4-29-2015

Formation Mechanism of Char and Coke in Biomass Catalytic Pyrolysis

Shoucheng Du
shoucheng.du@engr.uconn.edu

Formation Mechanism of Char and Coke in Biomass Catalytic Pyrolysis

Shoucheng Du, PhD

University of Connecticut, 2015

Thermochemical conversion of biomass via pyrolysis can play an important role in renewable fuel production. Introduction of catalyst in biomass pyrolysis is an effective way to upgrade the quality of bio-oil via de-oxygenation reactions. However, in catalytic pyrolysis, char and coke are formed via primary decomposition of biomass and secondary catalytic reactions of pyrolysis intermediates, respectively. The formation of coke and char is the main reaction competing with the production of favorable aromatic compounds and can significantly deteriorate catalyst activity. Control of coke and char formation during pyrolysis could be possible through innovative catalyst and process designs, in which fundamental understanding of the formation mechanisms of char and coke should be viewed as a prerequisite. This study utilizes various experimental and modeling techniques in order to measure and interpret the physicochemical characteristics of char and coke and gain mechanistic insights of their origins during biomass catalytic pyrolysis. This study includes design and testing of a conical spouted bed reactor for in-situ biomass catalytic pyrolysis, investigation of the effect of key operating parameters on pyrolysis product distribution, characterization of char and coke structures and a structured model compound exploration of coke formation mechanisms. It is shown that char and coke have different origins. They cannot be lumped as one, since they occupy different locations on the catalyst surface and, thus, contribute differently to catalyst deactivation. Char, a product from thermal reactions, forms as an external layer on the catalyst surface and in its macropores, whereas coke, a catalytic product, forms inside the zeolite micropores. By studying the coke formation using biomass model compounds, it is concluded that the chemical structure of coke depends on its chemical precursors. The formation of coke from

olefins, aromatic hydrocarbons and aromatic oxygenates are all directly related to the so-called “hydrocarbon pool” mechanism, following mainly hydrogen transfer and cyclization reactions.

Formation Mechanism of Char and Coke in Biomass Catalytic Pyrolysis

Shoucheng Du

B.S., Dalian University of Technology, 2010

A Dissertation

Submitted in Partial Fulfillment of the

Requirements for the Degree of

Doctor of Philosophy

at the

University of Connecticut

2015

APPROVAL PAGE

Doctor of Philosophy Dissertation

Formation Mechanism of Char and Coke in Biomass Catalytic Pyrolysis

Presented by
Shoucheng Du, B.S.

Major Advisor

_____

George M. Bollas

Associate Advisor

_____

Julia A. Valla

Associate Advisor

_____

Steven L. Suib

Associate Advisor

_____

Richard S. Parnas

Associate Advisor

_____

Luyi Sun

University of Connecticut
2015

Dedicated to my wife, Ting Jiang

ACKNOWLEDGMENTS

I would like to thank my parents for their support and guidance so that I could pursue a PhD degree in the USA. Moreover, I would like to thank my wife, Ting Jiang, who is always there when I need a listener, helps me with research discussions when I have questions, and trusts, encourages and stands behind me the many times things did not go right. Furthermore, I would like to show my great appreciation to my major advisor, Prof. George M. Bollas, for all his guidance and suggestions during my PhD studies. I am very glad to see the growth of myself towards a real researcher with all the experiences that he shared with me and the knowledge and skills that I learned from him. I would also like to thank Prof. Julia A. Valla, Prof. Steven L. Suib, Prof. Richard S. Parnas and Prof. Luyi Sun for not only serving on the defense committee, but also offering me help and suggestions in collaborated research projects. I am grateful to the members of the Bollas group, Dr. Monica Navarro, Zhiquan Zhou, Lu Han and Chunxiang Zhu for their help from many angles in both daily life and research. Thanks also go to my lab mate, David Gamliel from Prof. Julia A. Valla's group for being a very good friend and a great teammate in research during the past year and a half. Moreover, thanks to all the lab technicians at Center for Clean Energy Engineering (C2E2) and the analytical lab staff at Institute of Materials Science, UConn. Without their patient help and professional training, my research would not go as smooth as it did. Finally, thanks to all the undergraduate students that have been working with me and all the other friends at C2E2. With the help of everyone mentioned, I had a truly wonderful and formative experience.

This work was supported by the UCONN Faculty Large Grant and National Science Foundation under Grant No. 1236738.

TABLE OF CONTENTS

LIST OF TABLES

LIST OF FIGURES

CHAPTER 1 INTRODUCTION

1.1. Biomass and lignocellulosic biomass

Biomass has received considerable attention as a close to CO_2 neutral and sustainable feedstock that can replace fossil fuels for energy generation.[1–5] According to the literature,[6] the U.S, Europe, Africa, Latin America, and the rest of the world could produce 23.4, 8.9, 21.4, 19.9 and 76~376 EJ/year of biomass, respectively, with an energy equivalence of 3.8×10^9, 1.4×10^9, 3.5×10^9, 3.2×10^9 and 1.3×10^{10}~6.4×10^{10} barrels of oil energy equivalent. First generation biofuels technologies (bioethanol) rely on feedstocks not sufficiently available that compete with the food industry. A sustainable biofuels strategy should utilize widely available, low-cost, non-edible carbon sources lignocellulosic biomass for the production of sustainable liquid fuels.[4,6,7] Moreover, lignocellulosic biomass is also a promising feedstock for the production of chemicals.[8–10] However, lignocellulosic biomass is difficult to deconstruct into hydrocarbon-containing sub-fractions, because of its heterogeneous composition (Table 1-1).[7]

Table 1-1: Composition of typical biomass feedstocks and relevant model compounds (wt%)[11]

	C	H	O	S	N	Ash
Pine sawdust	53.10	5.21	39.31	0.02	0.17	1.33
Miscanthus	47.92	5.50	41.00	0.11	0.54	2.85
Wheat straw	46.02	5.50	44.50	0.10	1.65	5.04
Rice husk	44.22	5.06	41.81	0.51	0.50	10.91
Cellulose	44.40	6.20	49.40	-	-	-
Glucose	40.00	6.67	53.33	-	-	-

1.2. Biomass pyrolysis and catalytic pyrolysis

The thermochemical methods used for lignocellulose deconstruction can be broadly lumped into

combustion, gasification, liquefaction, and pyrolysis.[12,13] Among these, pyrolysis (thermal treatment at 400-600°C in inert gas atmosphere) is developing rapidly and can play a very important role in the future of renewable energy production.[14] Depending on the heating rate, biomass pyrolysis can be separated into two categories: slow pyrolysis (0.1 □ 1 K/s) and fast pyrolysis (10 □ 1000 K/s or higher, including flash pyrolysis).[15] Slow pyrolysis produces large amounts of carbonaceous residues, which can be used as a solid fuel or fertilizer, whereas fast pyrolysis produces high yields of bio-oil.[6] However, the bio-oil produced from the thermal pyrolysis cannot be directly used as fuel replacement due to its composition and heating value deficiency, as compared, for instance, with diesel (shown in Table 1-2). Thus, upgrading of the bio-oil is needed.

Table 1-2: Comparison of characteristics of bio-oil from thermal pyrolysis and diesel fuel (40 °C and 25% water)[16]

Physical property	Bio-oil from thermal pyrolysis	Diesel fuel
Moisture content (wt%)	20-30	0.1
PH	2.0-2.5	-
Density (kg/L)	1.2	0.94
Elemental analysis (wt%)		
C	55-58	85
H	5-7	11
O	35-40	1
N	0-0.2	0.3
Ash	0-0.2	0.1
HHV as produced (MJ/kg)	16-19	40

Catalytic fast pyrolysis (CFP) combines the pyrolysis with catalytic upgrading, and enhances selectivity to hydrocarbons, particularly aromatics.[17–20] An obvious benefit of using a catalyst such as a zeolite is that conversion of lignocellulose to gasoline takes place in a single step,

thereby simplifying the process of using two reactor setups (pyrolysis and upgrading).[16]

1.3. Spouted bed reactor vs micro-pyroprobe

Various reactor configurations have been used in Catalytic fast pyrolysis studies. Micro-pyroprobe reactors offer an attractive technique for studying the pyrolysis of biomass.[17,21] In a PyGC, reactions occur in a microreactor, and all products can be analyzed on-line. Excellent control of temperature and heating rate can be obtained in micro-pyroprobe reactors. Moreover, with PyGC, only small amounts of biomass and catalyst are required. The simplicity of operation makes it a widely applied flexible tool to simulate the CFP in bench-scale and industrial scale reactors.[17,21–25] However, PyGC experimentation entails intrinsic limitations such as inefficient biomass/catalyst mixing, small biomass loading (which results in insufficient quantity of coked samples for later analyses in this study) and requirement of small particle size for the biomass feed. Moreover, the PyGC cannot be economically scaled up to satisfy industrial needs.[20] On the contrary, fluidized bed reactors have been extensively utilized in chemical processes across the chemical industry due to their scalability, excellent mass and heat transfer properties, good mixing between the solids and the suspending fluid, uniform catalyst distribution, ability to operate continuously and so forth. One type of fluidized bed reactor is the spouted-bed reactor. Other work has shown that spouted bed reactors can handle large particle size distributions, larger particles, differences in particle densities, and provide excellent mixing.[2]

1.4. Char and coke

In biomass pyrolysis, slow or fast, catalytic or thermal, there is always some solid residue (typically, a mixture of coke and char, depending on the pyrolysis process) produced in parallel to non-condensable products and condensable bio-oil plus water.[13,26,27] In this regard, the formation of char and coke consumes the carbon content of the biomass, thus leading to relatively lower carbon content in the bio-oil. Moreover, the formation of char and coke may deactivate the

catalyst,[18,28] leading to a negative effect on the bio-oil quality. Although the study of formation of coke and char is important in the effort to improve the bio-oil quality, the definition of coke and char varies among different studies. Elordi et al.[29] studied the Catalytic fast pyrolysis of polyethylene in a spouted bed reactor at 500°C, using HZSM-5, HY, Hβ catalysts. They defined coke as the carbonaceous material deposited on the catalyst. They claimed that the combustion of coke in the meso- and macro-pores of the catalyst shows a temperature programmed oxidation (TPO) peak at lower temperatures, compared with the coke located inside the zeolite crystal channels due to differences in composition. They also observed coke outside the zeolite crystals with heterogeneous sizes between 10 and 50 nm, using transmission electron microscopy (TEM). In the review of biofuel production by Huber and Corma,[30] coke was defined as the organic fraction that could only be removed from the catalyst *via* calcination. Char was defined as the organic fraction deposited in the reactor as a result of thermal decomposition, but not on the catalyst. Triantafyllidis et al.[31] studied the Catalytic fast pyrolysis of beech wood in a fixed bed reactor at 500°C, using mesoporous aluminosilicate and conventional Al-MCM-41 catalysts. They considered coke as a lump of the solid carbonaceous residue produced thermally in the reactor as a separate phase to the catalyst, as well as the solid residue deposited on the catalyst surface due to thermal and catalytic cracking. Generally, coke is considered as the catalytic product, whereas char is the residue formed *via* thermal deconstruction. This definition is widely accepted, and many researchers describe the solid residue after thermal pyrolysis as char.[27,32,33] Based on this definition, primary decomposition and secondary polymerization contribute to char formation,[34,35] while coke formation is mainly attributed to catalytic polymerization of small biomass molecules inside the catalyst pores.[36] Generally, coke formation leads to catalyst deactivation and results in undesirable product selectivity in biomass pyrolysis,[6] whereas char may or may not deactivate the catalyst, depending on the location of its formation.

1.5. Challenges in studies on char and coke formation

Cheng and Huber[18] studied catalytic pyrolysis of furan over ZSM-5. They concluded that the soluble coke mostly consisted of aromatic rings and carbonyl groups. They identified the molecular weight distribution of soluble coke, using gel permeation chromatography (GPC), and concluded that the maximum molecular weight of soluble coke is beyond the limitation of a GPC column (MW >104). Extraction of the polyaromatic hydrocarbons (PAHs) from the biochar after pyrolysis was also performed by Fabbri et al.,[37] who found that the main PAHs in the biochar were naphthalene, phenanthrene, fluoranthene, and pyrene. Although it is seen in the literature that soluble coke has been well studied and characterized, the structure of insoluble coke, which represents about 95 C% in coke,[18] is still unknown.

Some effort has been put to study the structure of coke/char as a whole, without extracting only the soluble part. Brewer et al.[38] proposed a structure of char formed by slow and fast thermal pyrolysis of switch grass derived from ^{13}C-NMR analysis. They estimated that aromatic clusters of 7-8 rings terminated by carbonyl and hydroxyl groups are representative of the composition of thermal char (shown in Figure 1-1).

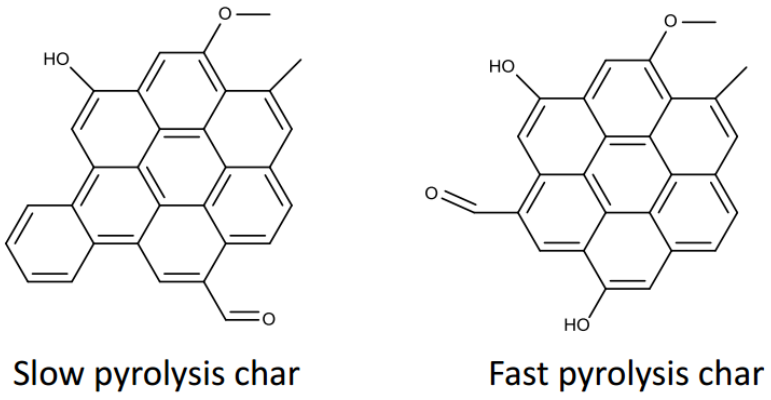

Figure 1-1: Proposed structure of char from slow and fast pyrolysis of switchgrass.[38]

Valle et al.[39] studied the catalytic upgrading of bio-oil with methanol over ZSM-5. They showed two origins of coke, thermal and catalytic, by performing temperature programmed oxidation (TPO). By deconvoluting the TPO peaks, they surmised that catalytic coke is deposited mainly inside the zeolite crystal channels; whereas thermal coke is mostly formed outside of the zeolite crystals. Guisnet and Magnoux[40] reviewed the organic chemistry of coke formation. With transmission electron microscopy (TEM) coupled to electron energy loss spectroscopy (EELS), they showed that with HZSM-5 the structure of coke was similar to that of coronene (pregraphitic), while with USHY it was similar to that of pentacene (linear polyaromatic). These studies have provided significant insights to the understanding of the structure of coke and char. However, the results from the current studies do not provide a deep enough insight to the coke/char chemistry and further revealing of the coke/char chemical structure is in demand. Thus, obtaining a clearer picture of the structure of coke/char during biomass (catalytic) pyrolysis is still challenging.

1.6. Chemistry of char and coke formation

As far as coke and char formation mechanisms are concerned (especially the coke formation mechanism), model compounds are widely used to study reaction chemistries.[18,41–44] Some pathways for the formation of coke have been identified previously. Model compounds for the study of coke formation can be lumped as aromatic hydrocarbons, aromatic oxygenates and small oxygenates. For instance, when toluene is chosen as the precursor, coke forms under self-alkylation reactions[45] and/or side alkylation with propylene[46] under carbenium ion mechanisms. The carbenium ion mechanism in coke formation is also proposed by Huang et al.,[47] who claimed that, at the temperature of 260-450 °C, the formation of coke during ethylbenzene disproportionation over ZSM-5 is initiated by the formation of alkylcarbenium ions, followed by repeated intermolecular hydride transfer reactions. Besides carbenium ion mechanisms, at the extreme pyrolysis conditions (high temperature, high vacuum), Zhang et al.,[48] Lannuzel et al.,[43]

Matsugi and Miyoshi,[49] and Colket and Seery[50] proposed radical reaction mechanisms for coke precursors.

In the study of coke formation from aromatic oxygenates, Cheng and Huber[18,51] performed catalytic pyrolysis of furan. They proposed the Diels-Alder reaction pathways from the "hydrocarbon pool", followed by oligomerization, cyclization, cracking, isomerization, and hydrogen transfer reactions for coke formation. In regards to the formation of coke from small oxygenates, Ramasamy et al.[52] studied biomass-derived small oxygenates under pyrolysis at 360 °C and 300 psig, including ethanol, acetaldehyde, acetic acid and ethyl acetate. Particularly in the cases of acetaldehyde, acetic acid and ethyl acetate, they proposed several aldol condensation reactions in the initial steps, leading to the formation of olefins and single-ring aromatic hydrocarbons, which are considered to be coke precursors. Moreover, coke formation from propanal was studied by Hoang et al.,[53] using ZSM-5 of different crystallite sizes. They found that the formation of coke proceeds under aldol condensation followed by cyclization. In addition, the larger crystallites of ZSM-5 with longer diffusion path length produce more coke than the smaller crystallites.

Although coke formation in catalytic pyrolysis of various model compounds has been investigated, the reaction pathways proposed are inconsistent and uncertain due to the unclear chemical structure of coke. It will be extremely helpful to reveal the coke structure and further understand the coke formation chemistry if the pyrolysis liquid and gas product analyses can be combined with the characterization of coke.

1.7. Objective of this study

This study focuses on understanding the mechanisms of coke and char formation during biomass catalytic pyrolysis in various reactor configurations. The objective of this study is to explore the char and coke structures and the coke formation mechanism during biomass catalytic pyrolysis.

The work presented herein focuses on the effect of operating conditions and feedstocks (biomass and model compounds) on the product distribution, especially coke and char yields, the characteristics of coke and char from various biomass and model compounds, and the coke formation mechanisms during catalytic pyrolysis. This study aims to combine coke and char characterization, product distribution, bio-oil selectivity and reaction mechanism identification using model compounds, in order to reveal the char and coke origins and their formation mechanisms. Questions that this study seeks to answer include:

- What is the structure of char and coke?
- What are the key operating and reactor parameters that affect char and coke formation?
- How does coke form?
- What is the role of oxygen in coke formation?
- What are the compounds that contribute the most to coke formation?
- What is the chemical structure of coke and how is it affected by its formation precursors?
- When using a supported catalyst, what is the impact of the support on coke formation?

CHAPTER 2 METHODS

2.1. Feedstock and catalysts

In the majority of the experimental results presented herein, miscanthus and pine were used as the biomass feedstock. Miscanthus×giganteus is a very promising energy crop, due to its fast growth and low mineral content. Pine sawdust was used as biomass feedstock for pyrolysis studies due to its wide availability.[17,54,55] Dried biomass was grinded and sieved to 80-175 μm particle size. Glucose, cellulose, toluene, tolualdehyde and furan were chosen as biomass model compounds.

In biomass catalytic pyrolysis, zeolite catalysts, including ZSM-5, Beta zeolite, Y zeolite, Mordenite and several mesoporous materials, have been widely studied.[28,31,56,57] In the majority of these studies, ZSM-5 has been proven to be very effective in catalytic (fast) pyrolysis due to its proper pore morphology.[56,58] In this study, a commercial ZSM-5 catalyst (synthesized by W.R. Grace & Co. in Al_2O_3/SiO_2 macroporous matrix of mean particle size of 70 μm) was used for the catalytic pyrolysis. In order to reveal the effect of catalyst support, Al_2O_3 from W.R. Grace & Co. was also used in the catalytic pyrolysis. In the study of coke formation mechanism, commercial ZSM-5 zeolite (CBV 8014) was purchased from Zeolyst International, Inc. and was used in the catalytic pyrolysis of biomass model compounds for the investigation of coke formation.

2.2. Conical spouted bed reactor

Figure 2-1 presents two pictures of the spouted bed reactor setup, which includes the conical spouted bed reactor housed inside an electrical furnace, biomass and catalyst feeders, liquid collection system and Fourier Transform Infrared Spectroscopy (FTIR) for on-line gas analysis. During the experiments, biomass was fed at a rate of 4 gr/min from the bottom for 1min, using a screw feeder and a vertical entrainment line with 5 SL/min N_2 flow. The catalyst of 4-20 gr was fed via entrainment from the catalyst feeder connected to the bottom of the reactor. During the reaction, volatile matters, including organic vapors and permanent gas, exit from the top of the

reactor and pass through a condensing system. The organic vapors were condensed in a six-impinger train in dry-ice bath. Methanol was used in the impingers as a solvent to trap the organic vapors. The intermediate line between the reactor outlet and the impinger train was maintained at 300 °C, to prevent condensation of organic vapors in the line. The FTIR was connected on-line right after the liquid collection system, for analysis of the gas composition. A cooling jacket was applied to keep the inlet of the reactor below 100 °C, thus eliminating blockage of the inlet, caused by low temperature thermal pyrolysis of biomass.

(a) (b)

Figure 2-1: Pictures of the conical spouted bed reactor. (a) whole reactor setup; (b) the hot reactor inside the furnace; (c) glass reactor of the same dimension for cold flow hydrodynamic study

2.3. Pyroprobe-GC-MS

A comparison of the spouted bed designed in this work with a Pyroprobe-GC-MS (PyGC) was performed. The PyGC used here was micro reactor (CDS Analytical Pyroprobe 5200HP) connected to a gas chromatograph-mass spectrometer (GC-MS), shown in Figure 2-2. In a typical PyGC experiment, a small amount of biomass (5-10 mg) or biomass and catalyst mixture is

loaded in the quartz microreactor and held in place by quartz wool. The microreactor is inserted into the probe, and then placed in the pyrolysis interface, maintained at 300 °C for the duration of the experiment to prevent condensation of pyrolysis vapors. The probe is then heated to the desired pyrolysis temperature and maintained isothermally for a probe time of 20 seconds (enough to volatilize all biomass in the microreactor[59]). The heating rate is 20 °C/ms.[60] The pyrolysis vapor products are carried by the Ar carrier gas from the microreactor to either a cold trap (*in situ*), or a secondary fixed bed reactor (*ex situ*) followed by the cold trap. Condensable liquids are adsorbed onto the trap and permanent gas is carried through to an online mass spectrometer (MS, Agilent 5975C). All experiments presented here were performed at probe and reactor temperatures of 600 °C. After pyrolysis, condensed vapors were desorbed from the trap and swept to a gas chromatograph equipped with a mass spectrometer (GC-MS, Agilent 6890 GC with 5973N MS). Constant He flow of 1 mL/min, an inlet temperature of 270 °C, and split ratio of 75:1 were used for GC-MS. The GC-MS was calibrated by injecting external standards through the PyGC system. Solid yield was determined by oxidizing the residue at 800 °C and quantifying the CO_2 and CO with MS.

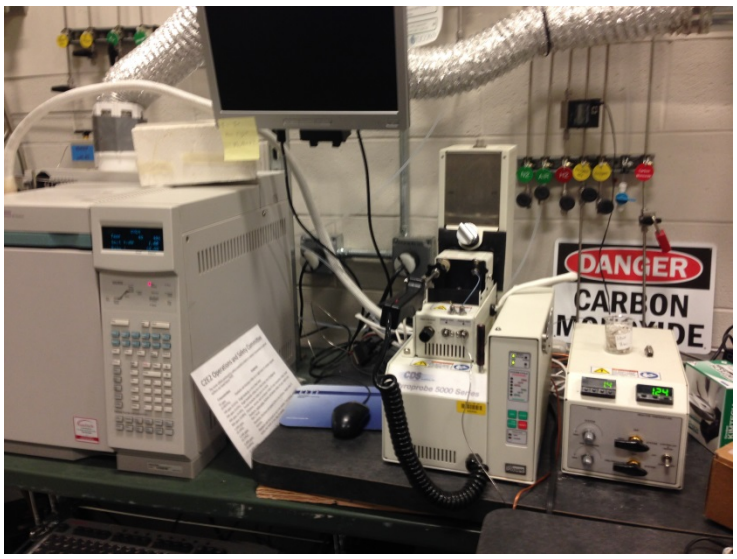

Figure 2-2: Picture of the PyGC setup

2.4. Horizontal fixed bed reactor

In the study of char and coke characteristics, slow thermal and slow catalytic pyrolysis were performed in a fixed bed quartz tube reactor (1 inch o.d. and 24 inch length), which was heated in a horizontal tube furnace. Nitrogen was used for purging gas during the pyrolysis with 20 sccm flow rate. During the pyrolysis, the reactor was heated from room temperature to 600 °C at the heating rate of 10 K/min and stayed isothermal for 15 min. Two pictures are shown in Figure 2-3 for the horizontal fixed bed reactor.

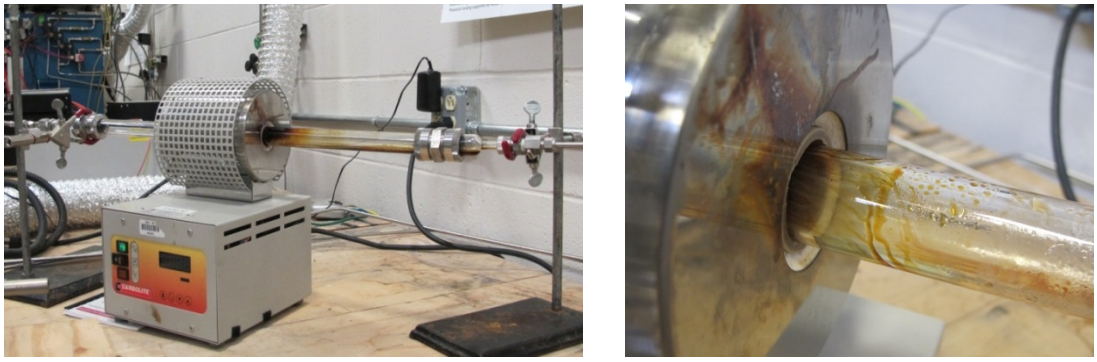

(a) (b)

Figure 2-3: Pictures of the fixed bed reactor. (a) whole reactor setup; (b) release of the organic vapors during the pyrolysis

2.5. Vertical fixed bed reactor

In the study of coke formation by pyrolysis of biomass model compounds, a vertical fixed bed reactor together with a saturator was used. A picture of the vertical fixed bed reactor setup is shown in Figure 2-4. The catalyst bed of ZSM-5 zeolite (1-3 gr) was held in place by two plugs of quartz wool in a quartz tube reactor (22 mm ID). The reactor was heated by a vertical tube furnace, and the bed temperature was confirmed by a K-type thermocouple placed in the middle of the reactor. The saturator temperature was maintained at 10 °C above the boiling point of each main reactant. All experiments were performed with Ar purge flow at 50 sccm. One gram of reactant was then injected using a syringe through a septum into the preheated saturator. The

condensable products were collected in an impinger with 20 mL methanol in dry ice. The product gas stream was fed to an online Mass Spectrometry (MS, Agilent 5975C).The experiment proceeded until only the argon carrier gas could be detected by the MS.

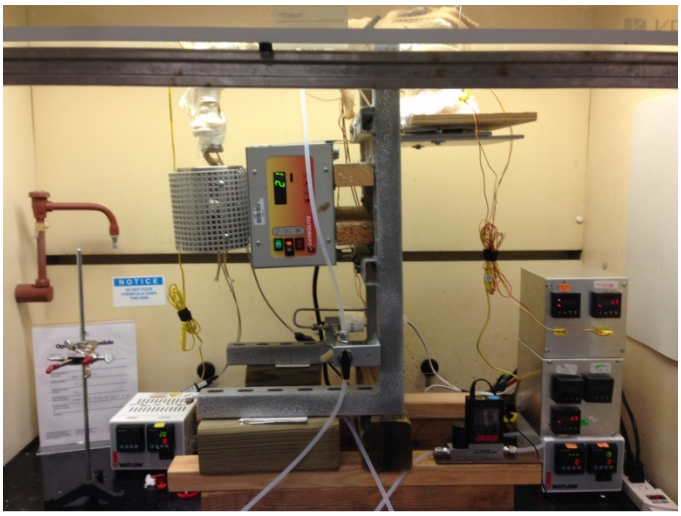

Figure 2-4: Pictures of the vertical fixed bed reactor setup.

2.6. Analytical techniques

2.6.1.Fourier Transform Infrared Spectroscopy (FTIR)

Gas composition analysis was performed using a Thermo Nicolet 6700 FTIR with a 2-meter gas cell. Number of scans of 16 was used with a resolution of 1 cm^{-1} and optical velocity of 6.3290 cm/sec. The collection of each data point took 11 sec, allowing for real-time gas analysis. The total mole fraction for each gas component was calculated by integrating its spectrum area over the time of experiment. FTIR measurements to characterize the functional groups of the char/coke were also performed in a Nicolet MAGNA-IR 560 spectrometer with a DTGS detector. The FTIR was operated at 4 cm^{-1} resolution and 132 scans.

2.6.2.Diffuse Reflectance Infrared Fourier Transform Spectroscopy (DRIFTS)

DRIFTS of the coked zeolites was performed in NICOLET 6700 Fourier Transform Infrared Spectroscopy (FTIR) from Thermo Scientific, equipped with an MCT detector and the Praying

Mantis DRIFTS cell from Harrick Scientific. Pure KBr was used as background. Samples were diluted in KBr (0.5 wt% concentration) for each analysis.

2.6.3.Mass Spectrometry (MS)

Gas products were analyzed online with mass spectrometry (MS, Agilent 5975C, inert with triple axis detector). H_2, CH_4, CO (C_2H_4), CO_2, C_3H_6, and Ar were calibrated using standard gases.

2.6.4.Gas Chromatograph-Mass Spectrometry (GC-MS)

Liquid products were analyzed using an Agilent 6890N Gas Chromatograph equipped with a 5973N mass selective detector (GC-MS). An Agilent DB-5 column was used. A split ratio of 50:1 and temperature program of isothermal at 40 °C for 2 min followed by a 10 °C/min ramp to 270 °C was applied for furan, benzene and toluene quantification. All other compounds were identified with a splitless injection and the temperature program of isothermal at 40 °C for 2 min followed by a 1 °C/min ramp to 87 °C and a 20 °C/min ramp to 270 °C was applied. Quantification standards consisting of furan, benzene, toluene, xylene, ethylbenzene, styrene, benzofuran, indane, naphthalene, naphthalene, 1-methyl naphthalene, biphenyl, diphenylmethane, acenaphthalene, fluorene, phenanthrene, anthracene and tolualdehyde were calibrated. All other compounds were analyzed using the semi-quantification method.

2.6.5.Scanning Electron Microscopy (SEM)

Char/coke samples were observed using a FEI Quanta FEG 250 SEM under high vacuum, to distinguish the differences in morphology of char samples produced in different experiments and visualize the coke/char deposition on the surface of catalyst pellets. Before each experiment, char samples were coated with gold to inhibit charging when the magnification is high.

2.6.6.Focused Ion Beam (FIB) and Scanning Transmission Electron Microscopy (STEM)

The FIB in-situ sample preparation and EDX element mapping was performed in a FEI Strata 400 STEM Dual Beam system, a fully digital Field Emission Scanning Electron Microscope (FE-

SEM) equipped with Focused Ion Beam (FIB) technology and Flip stage/STEM assembly. A catalyst particle was selected and milled on both sides, leaving a thin layer along the equatorial plane of the particle. The thin catalyst layer was lifted out with an Omniprobe micro-manipulator and imaged under scanning transmission electron microscopy (STEM).

2.6.7.Thermogravimetric Analysis (TGA)

Comparison of thermal properties of char samples was performed in a Q-500 thermogravimetric analyzer from TA Instruments. The samples were first dried at 120°C for 30 min and heated up to 900°C in air flow of 60 ml/min. In the study of char and coke characteristics, three different heating rates (5/10/15 K/min) were used in order to get accurate results for kinetics modelling. For the study of coke formation mechanism, the weight percent of coke on zeolite/catalyst was determined by weight loss during combustion at temperature up to 900 °C.

2.6.8.Nitrogen Adsorption and Desorption

The surface area and pore size distribution of char/coke were determined in a Micrometitics ASAP 2020 Accelerated Surface Area and Porosimetry System. The isotherms of N_2 at 77 K were obtained from physisorption. Before analysis, all the char samples were degassed at 250°C under vacuum for 12 hr to remove the surface contaminants. The pore size distribution of the char samples was determined from the N_2 adsorption isotherms at 77 K, using the Barrett-Joyner-Halenda (BJH) method.

2.6.9.Raman Spectroscopy

Raman spectra were obtained for coked zeolites in a Renishaw 2000 Ramanscope, operated with a 0.024 in focus length, 514.5 nm laser excitation source (2.41 eV), at 20% power and 32 exposure times, to avoid detector saturation. For each sample, laser focus was set to 40% to prevent local damage and 3 different positions were analyzed to verify the spectra.

2.6.10. Elemental Analysis

Elemental analysis of the coked zeolites was performed in Vario MICRO Elemental Analyzer from Elementar Americas Inc. Right before each analysis, samples were dried in an oven at 100 °C for 3 hr. Samples of 2-5 mg were measured using microbalance and loaded into the instrument. Sulfanilamide was used as the standard sample for the calibration.

2.6.11. Solid state 13C Nuclear Magnetic Resonance (NMR)

Solid-state magic angle spinning (MAS) Nuclear magnetic resonance (NMR) spectra were acquired with a Bruker Avance III 400 MHz spectrometer operating at field strength of 9.4 T, hence a frequency of 400 MHz for 1H and 100.6 MHz for ^{13}C by using a triple resonance 2.5 mm MAS probe. Samples were packed in a Zirconia rotor with Vespel caps and spun at 35 kHz at room temperature. Quantitative direct polarization ^{13}C MAS NMR spectra were acquired with 90° pulse width of 2.5 s, delay time of 120 s ($> 5T_1$) and 100 kHz of spectral width using spinal 64 high power proton decoupling. Chemical shifts were given with respect to tetramethylsilane (TMS) by using an external reference of glycine (carbonyl at 176.5 ppm) for ^{13}C as the secondary reference. The coked zeolites were characterized in NMR without HF and CH_2Cl_2 treatment, in order to see the total characteristics of both soluble and insoluble coke.[40]

CHAPTER 3 DESIGN AND TEST OF A SPOUTED BED REACTOR FOR CATALYTIC PYROLYSIS OF BIOMASS

The results of this Chapter have been published in Bioresource Technology, 2014.[61]

3.1. Introduction

Global energy unsustainability and environmental issues have generated interest in searching for alternative and renewable energy sources. Biomass has been a major source of energy for mankind dating back to ancient times. Today, it is the fourth largest source of energy in the world.[6] Lignocellulosic biomass is the most abundant form of biomass, typically composed of cellulose (38–50%), hemicellulose (23–32%) and lignin (15–25%). Renewable woody biomass can be transformed into liquid, gaseous and solid fuels or fuel precursors through pyrolysis, thereby decreasing our dependency on fossil fuels. However, thermal pyrolysis of lignocellulosic biomass produces a bio-oil of low quality, due to its high oxygen content, high acidity, and low calorific value. Catalytic pyrolysis has been shown to be an effective way to enhance deoxygenation reactions, thus improving the bio-oil quality. Furthermore, fast heating rates also improve the bio-oil quality.[6] Therefore, Catalytic fast pyrolysis (or catalytic fast pyrolysis) was studied and shown to be among the most effective processes for the conversion of lignocellulosic biomass to fuels and chemicals.

Various reactor configurations have been used in Catalytic fast pyrolysis studies. Micro-pyroprobe reactors have been widely used to study Catalytic fast pyrolysis of biomass due to their ease of operation,[17,21] but they entail intrinsic limitations such as inefficient biomass/catalyst mixing, small biomass loading and particle size. Moreover, they cannot be economically scaled up to satisfy industrial needs;[20] they are useful only for bench-scale studies. On the contrary, fluidized bed reactors have been extensively utilized in chemical processes across industry due to their scalability, excellent mass and heat transfer properties, good mixing between the solids and

the suspending fluid, uniform catalyst distribution, ability to operate continuously and so forth. Therefore, it is of industrial relevance to study biomass pyrolysis in fluidized bed reactors, focusing on more realistic bench-scale experimentation and simulation. One type of fluidized bed reactor is the spouted-bed design, which was shown to be ideal for application to biomass pyrolysis. It can handle large particle size distributions, larger particles, differences in particle densities, and provide excellent mixing.[2]

The effect of operating conditions, such as temperature and catalyst to biomass ratio, on biomass catalytic pyrolysis product distribution has been widely investigated in the literature. Zhang et al.[36] studied the effect of temperature and weight hourly space velocity (WHSV) on product selectivity in pyrolysis of pine wood with ZSM-5 in a fluidized bed reactor. They showed that the maximum aromatic yield (13.9%, mainly including benzene, toluene, xylene and naphthalene) is achieved at 600 °C and 0.35 hr^{-1} WHSV (catalyst to biomass ratio of ~6). Thangalazhy-Gopakumar et al.[62] performed catalytic pyrolysis of green algae in a pyroprobe and observed a 13.9% maximum aromatic yield at 650 °C and catalyst to biomass ratio of 9. Bilbao and co-workers studied the spouting characteristics and the advantages of spouted beds, with specific applications to biomass pyrolysis.[55] However, other than their extensive work, a comprehensive study of the effect of operating conditions (temperature and catalyst to biomass ratio) on the product distribution in biomass catalytic pyrolysis in spouted beds is missing.

In this work, a bench-scale conical spouted-bed reactor was designed, using published correlations for the stability of the spouting regime and considering different particle properties, geometric factors and important hydrodynamic parameters. The challenges and advantages of the developed experimental setup are discussed and illustrated. With the specially designed reactor, Catalytic fast pyrolysis of miscanthus giganteus was studied. The effects of temperature (400-600 °C) and catalyst to biomass ratio (1:1-5:1) on biomass catalytic pyrolysis product distribution and

selectivity were investigated. In addition, the contribution of ZSM-5 catalyst support on the product distribution and selectivity was explored.

3.2. Experimental section

3.2.1. Feedstock and catalyst

Various lignocellulosic biomass sources have been investigated for bio-oil production through Catalytic fast pyrolysis, including pine wood, rice straw and wheat straw. Among biomass feedstocks, miscanthus was a promising energy crop due to its simple cultivation, high calorific value and fast growth rate.[63] In this study, miscanthus was used as the biomass feedstock. The feed was grinded and dried in an oven at 120 °C overnight and then sieved to 80-175 μm particle size. Proximate analysis of the feedstock was performed in a Q-500 thermogravimetric analyzer from TA Instruments, following literature protocols.[64] Ultimate analysis of the feedstock was carried out in a Vario MicroCube elemental analyzer from Elementar. The results of proximate and ultimate analysis are shown in Table 3-1.

Table 3-1: Proximate and ultimate analysis of the miscanthus feedstock

Proximate analysis (wt%)		Ultimate analysis (wt%)	
Moisture	4.81	C	40.94
Volatile	83.89	H	5.23
Fixed carbon	6.47	N	0.18
Ash	4.83	S	0.32
		O[a]	53.33

[a]Oxygen is calculated by difference

Commercial ZSM-5 catalyst and Al_2O_3-SiO_2 matrix from W. R. Grace & Co were used as the catalysts in this study. Table 3-2 shows basic information of the ZSM-5 catalyst and the Al_2O_3-SiO_2 matrix, including porosity and acidity. Comprehensive characterization of the ZSM-5

catalyst in terms of morphology and pore size distribution, and the deactivation of the catalyst due to coke and char formation during biomass (catalytic) pyrolysis were presented previously.[65]

Table 3-2: Characterization of the supported ZSM-5 catalyst and Al_2O_3-SiO_2 matrix[a]

	Physical property		Porosity analysis[b]			Acidity analysis[c]		
	ρ_{bulk} (kg/m^3)	d_p (μm)	S_{total} (m^2/g)	S_{micro} (m^2/g)	V_{micro} (cm^3/g)	B.s. (μmol/g)	L.s. (μmol/g)	B.s./L.s
ZSM-5	800	75~175	124.30	98.98	4.61E-2	35.26	3.16	11.15
Matrix	860	70~230	157.79	4.29	2.11E-4	2.07	35.36	0.06

[a] In Table 2, ρ_{bulk} stands for bulk density; d_p, particle size; S_{total}, BET surface area; S_{micro}, t-plot micropore area; V_{micro}, t-plot micropore volume; B.s., Brønsted acid sites; L.s., Lewis acid sites. [b]Porosity analysis was performed in Micrometitics ASAP 2020 Accelerated Surface Area and Porosimetry System. Samples were degassed at 250 °C under vacuum for 12 h before analysis. [c]Acidity analysis was performed by Diffuse Reflectance Infrared Fourier Transform Spectroscopy (DRIFTS). ZSM-5 and matrix were calcined in air at 350 °C for 3 hours, and then diluted with KBr to 6 wt%. Enough pyridine (99 wt%) was added to the samples to achieve saturation. Physisorbed pyridine was removed by heating the samples to 150 °C under vacuum. Extinction coefficients of 1.67 cm/μmol and 2.22 cm/μmol are used for concentration calculation of Brønsted and Lewis acid sites, respectively.[66]

3.2.2.Experimental setup and procedure

Figure 3-1 illustrats the spouted bed reactor setup, which includes the conical spouted bed reactor housed inside an electrical furnace, biomass and catalyst feeders, liquid collection system and Fourier Transform Infrared Spectroscopy (FTIR) for on-line gas analysis. The dimensions of the spouted bed reactor are also shown in Figure 3-1. The biomass was fed by the biomass auger feeder from the bottom of the reactor. The catalyst was fed by entrainment from the catalyst feeder also from the bottom of the reactor. The liquid collection system contains six impingers which were put in dry-ice bath. The FTIR was connected on-line right after the liquid collection system, which can analyze the gas composition as a function of time.

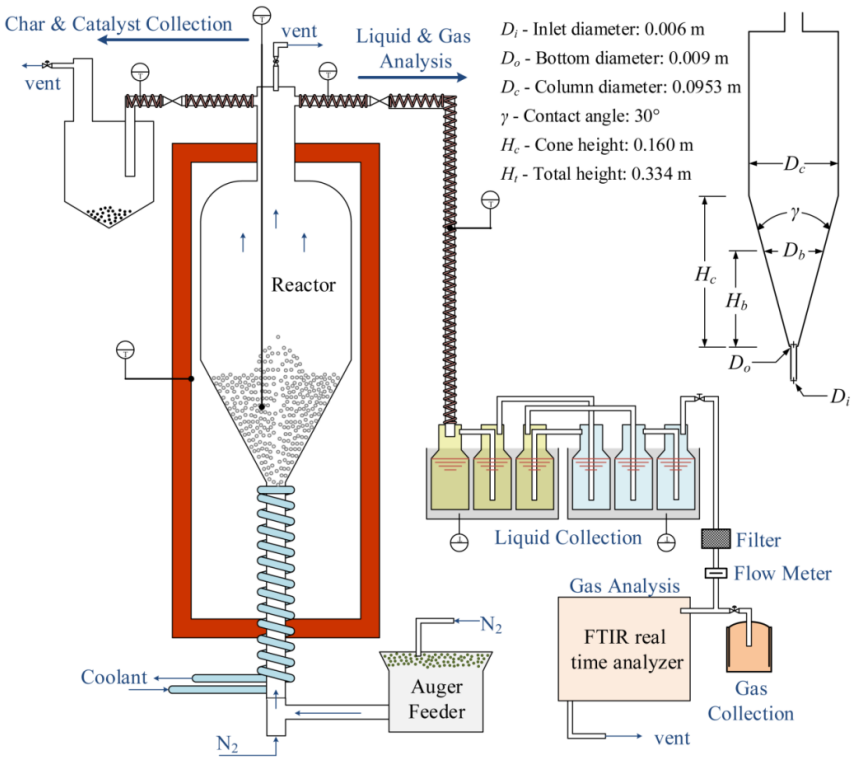

Figure 3-1: Conical spouted bed reactor setup for biomass catalytic pyrolysis.

Considerable effort was devoted on designing the biomass feeding system. Dai et al.[67] reviewed and discussed common biomass feeding problems, such as bridging and line blockages occurring in biomass thermochemical processes. The issues in biomass feeding were also studied by an international group of researchers.[32] For the extreme case of lignin pyrolysis, they showed that significant amounts of char are accumulated on the auger, unless special cooling designs were applied. This obviously affected the accuracy and consistency of bench-scale experiments and could potentially impact the operational stability and economics of the corresponding commercial equivalents. The spouted bed unit of the group of Bilbao and coworkers[55] has a hopper feeder system at the reactor top, which addressed the problems of auger feeding. However, depending on the setup and conditions, part of the biomass could be pyrolyzed in the top dilute zone and left the reactor, without being catalytically upgraded. Also, fine biomass particles might be entrained out

of the reactor before conversion to gas or bio-oil. In order to address these challenges, namely char formation on the feeder, blockage of the transfer line, inefficient contacting with catalyst, and fine particle entrainment, our reactor was designed to accept biomass from the bottom via entrainment (Figure 3-1). A cooling jacket was applied to keep the inlet of the reactor below 100 °C, thus eliminating blockage of the inlet, caused by low temperature thermal pyrolysis of biomass. Thus, with the current design, biomass did not react until it contacted the hot catalyst bed inside the reactor.

In all the experiments, the catalyst was loaded into the reactor via entrainment. When the desired pyrolysis temperature was achieved (measured with a thermocouple inside the catalyst bed), biomass was fed at a rate of 4 gr/min from the bottom for 1min, using a screw feeder and a vertical entrainment line with 5 SL/min N_2 flow. During the reaction, volatile matters, including organic vapors and permanent gas, exited from the top of the reactor and passed through a condensing system. The organic vapors were condensed in a six-impinger train in dry-ice bath. Methanol was used in the impingers as a solvent to trap the organic vapors. The intermediate line between the reactor outlet and the impinger train was maintained at 300 °C, to prevent condensation of organic vapors in the line. The total time for both reaction and purging was 10 min for all the experiments. After the experiment, the reactor was cooled down and washed with water. The water/char/catalyst mixture was dried overnight and then analyzed. Impingers were washed with methanol and the entrained solid particles were filtered out using a vacuum pump. The lumped char/coke yield was presented as the sum of the entrained solid particles and the solids obtained from the water/char/catalyst mixture subtracting the original catalyst load. All the experiments presented here were repeated at least three times and the mass balance for each was >90%.

3.2.3.Bio-oil and gas analysis

The bio-oil, condensed in the impinger train, was washed with methanol and collected. The total volume of the diluted bio-oil was then measured. The diluted bio-oil was analyzed in an Agilent 6890N Gas Chromatograph (GC) (Agilent DB-5 column) equipped with a 5973N mass selective detector (MS). The GC oven was held initially at 40 °C for 1 min and then ramped to 270 °C at 10 °C/min. Quantification was performed with benzene, toluene, xylene, ethylbenzene, styrene, benzofuran, indane, naphthalene, naphthalene, 1-methyl naphthalene, biphenyl, diphenylmethane, acenaphthalene, fluorene, phenanthrene and anthracene external standards, and the method of semi-quantification was applied for the remainder of the identified compounds. In this study, the liquid products were measured and reported in two ways, the lumped yield (including water) obtained by measuring the weight of impingers before and after pyrolysis (excluding the weight of entrained solids), and the bio-oil distribution measured by GC-MS.

Gas composition analysis was performed using a Thermo Nicolet 6700 FTIR with a 2-meter gas cell. Number of scans of 16 is used with a resolution of 1 cm^{-1} and optical velocity of 6.3290 cm/sec. The collection of each data point took 11 sec, allowing for real-time gas analysis. The total mole fraction for each gas component was calculated by integrating its spectrum area over the time of experiment. Due to the low content of sulfur in the miscanthus used (See Table 3-1) and the focuses of this study, the sulfur-content products were not analyzed and the reactions between zeolite and sulfur were not considered and reported.

3.3. Results and discussion

3.3.1.Design of the spouted bed reactor and hydrodynamic analysis

Table 3-3 shows the dimensions of the spouted bed reactor and the respective measurements of the pressure drop and minimum spouting flow rate. The reactor of this work was designed on the basis of the analysis by Bilbao and coworkers[68–70] for shallow conical spouted beds.

Table 3-3: Experimental conditions and hydrodynamic measurements[a]

Temperature (°C)	400/500/600	400/500/600	400/500/600
Catalyst/biomass ratio	1:1	2:1	5:1
Catalyst inventory, W_C (gr)	4	8	20
Stagnant bed height, H_b (m)	0.025	0.035	0.053
Stagnant bed top diameter, D_b (m)	0.022	0.028	0.037
Observed pressure drop ΔP_{exp} (atm)	0.002	0.004	0.007
Observed min. spouting at 25 °C	3.25	4.57	10.5

[a] All the experiments are batch, performed with N_2 flow of 5 SL/min for 10 min.

Table 3-4: Survey of correlations for minimum spouting velocity and pressure drop in shallow conical spouted beds

Correlations	Ref.	Geometry and Conditions
$(Re_i)_{ms} = 0.174 Ar^{0.5} \left(1 + 2\tan(\gamma/2) H_b / D_0\right)^{0.25} \tan(\gamma/2)^{-1.25}$	71	D_0=D_i, D_i=0.0103-0.0129m H_b=0.03-0.015m, γ=12-60°, d_p=0.5-2.5mm, ρ_s=0.98-2.36g/cm^3
$\frac{\Delta P_s}{H_b \rho_b g} = 7.68 \tan(\gamma/2)^{0.2} (Re_i)_{ms}^{-0.2} \left(\frac{H_0}{D_i}\right)^{-0.33}$	72	D_0=D_i, D_i=0.0103-0.0129m H_b=0.03-0.015m, γ=12-60°, d_p=0.5-2.5mm, ρ_s=0.98-2.36g/cm^3
$(Re_i)_{ms} = 0.126 Ar^{0.39} \left(\frac{D_b}{D_i}\right)^{1.68} \tan(\gamma/2)^{-0.57}$	70	D_i=0.06-0.01m, H_b=0.05-0.20m, γ=35-45°, d_p=0.08mm-0.5mm, ρ_s=0.91-1.39g/cm^3
$\frac{\Delta P_s}{H_b \rho_b g} = 1.2 \tan(\gamma/2)^{-0.11} (Re_i)_{ms}^{-0.06} \left(\frac{H_b}{D_i}\right)^{0.08}$	73	D_0=0.03-0.06m, H_b=0.36-0.61m, γ=28-45°, d_p=1mm-25mm, ρ_s=0.24-3.5g/cm^3
$(Re_i)_{ms} = \left[0.3 - \frac{0.27}{(D_b/D_i)^2}\right] \sqrt{\frac{Ar\left(\frac{D_b}{D_i}\right)\left[\left(\frac{D_b}{D_i}\right)^2 + \left(\frac{D_b}{D_i}\right) + 1\right]}{3}}$	74	D_0=D_i, D_i=0.015-0.03m, D_b/D_i>1.66, γ=24-60° d_p=0.88-6.17mm, ρ_s=0.85- 2.99g/cm^3
$\frac{\Delta P_s}{H_b \rho_b g} = 1.087 Ar^{-0.081}$	75	D_i=0.15m; γ=60º, H_b/D_c=0.42-0.67 ρ_s=3.88-7.6g/cm^3; d_p=0.5-2mm

These studies proposed correlations for minimum spouting velocity[68,69,76] and pressure drop under stable spouting for various reactor geometries, with various sizes, shapes and densities of particles.[73] Lima Rojas[75] presented a comprehensive review on the minimum spouting velocity and pressure drop in conical spouted beds. The majority of these correlations refer to deep beds, where the upper cylindrical part of the reactor is filled with catalyst particles. Epstein[77] recently commented on the misuse of the diameter of the cylindrical part D_c, when estimating minimum spouting velocity, u_{ms}, and pressure drop under stable spouting, ΔP_s, for shallow spouted beds. Reasonably, the top diameter of the reactor cone should not appear in correlations of the minimum spouting velocity and pressure drop for shallow spouted beds (such as the reactor of this work). Therefore, all the correlations suitable for the design of our reactor were filtered and only the correlations that refer to shallow beds (and do not contain the top cone diameter) are presented in Table 3-4. These correlations were used for the analysis of stable spouting fluidization regime for our reactor.

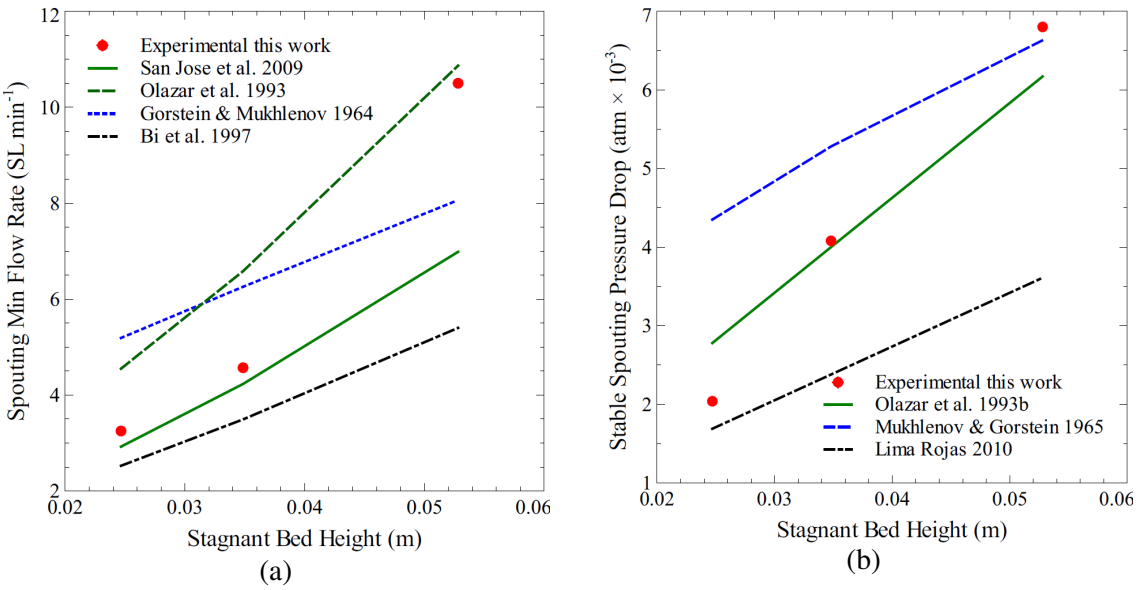

Figure 3-2: Calculated and measured minimum spouting flow rate (a) and solids pressure drop at stable spouting (b) for the biomass catalytic reactor of this work. Reactor geometry and stagnant bed heights are as shown in Table 3-3.

As shown in Figure 3-2, despite the geometric dissimilarities between published correlations and our reactor setup, good agreement is accomplished. The agreement between the correlations proposed by San José et al.[70] and Olazar et al.[73] (used to design our reactor) and the measurements of minimum spouting velocity and pressure drop validate the process followed for the design of the reactor. Evidently, at the highest catalyst loading (20gr) the hydrodynamic correlations deviate from experimental measurements, which is currently under investigation. According to this hydrodynamic analysis for all the experimental conditions, a 5 SL/min flow rate was found sufficient for stable spouting. This was validated with cold- and hot- flow experiments in a fused quartz reactor. As shown in the Figure 3-2, the measurements of minimum spouting velocity and pressure drop are in reasonable agreement with the literature correlations used for designing the reactor. Thereafter, a comprehensive analysis was performed to identify the stable hydrodynamic regimes, in which the designed reactor fell in.

Figure 3-3 shows a summary of various fluidization regimes by defining the dimensionless particle size, $d_p^* = Ar^{1/3}$ and the dimensionless velocity, $U^* = Re\ Ar^{1/3}$, where Ar is the Archimedes number and Re is the Reynolds number. The analysis is based on the work of Bi and Grace[78] and Grace[79], updated to account for the newer and more general correlation of Haider and Levenspiel[80] for the particle terminal velocity, U_t^*, and the recent correlation of Olazar et al.,[69] for the minimum spouting velocity, U_{ms}^*, in conical spouted beds at high temperatures. U_c^* and U_{se}^*, as reported by Bi and Grace,[78] depict the theoretical upper bound of stable fluidization and the critical velocity of entrainment, respectively. Figure 3-3 also illustrates the range of stable spouting operation explored in the current study. The corresponding operating regime is calculated, using the range of catalyst particle sizes (75-175 μm), different flow rates (3-5 SL/min), different catalyst loadings (4-20 gr) and different temperatures (400-600 °C) applied in this study. It shows the range of hydrodynamic conditions studied, not the entire operating

window of the spouted bed. According to Figure 3-3, the operating regimes studied are well within the acceptable ranges for stable fluidization in conical spouted beds.

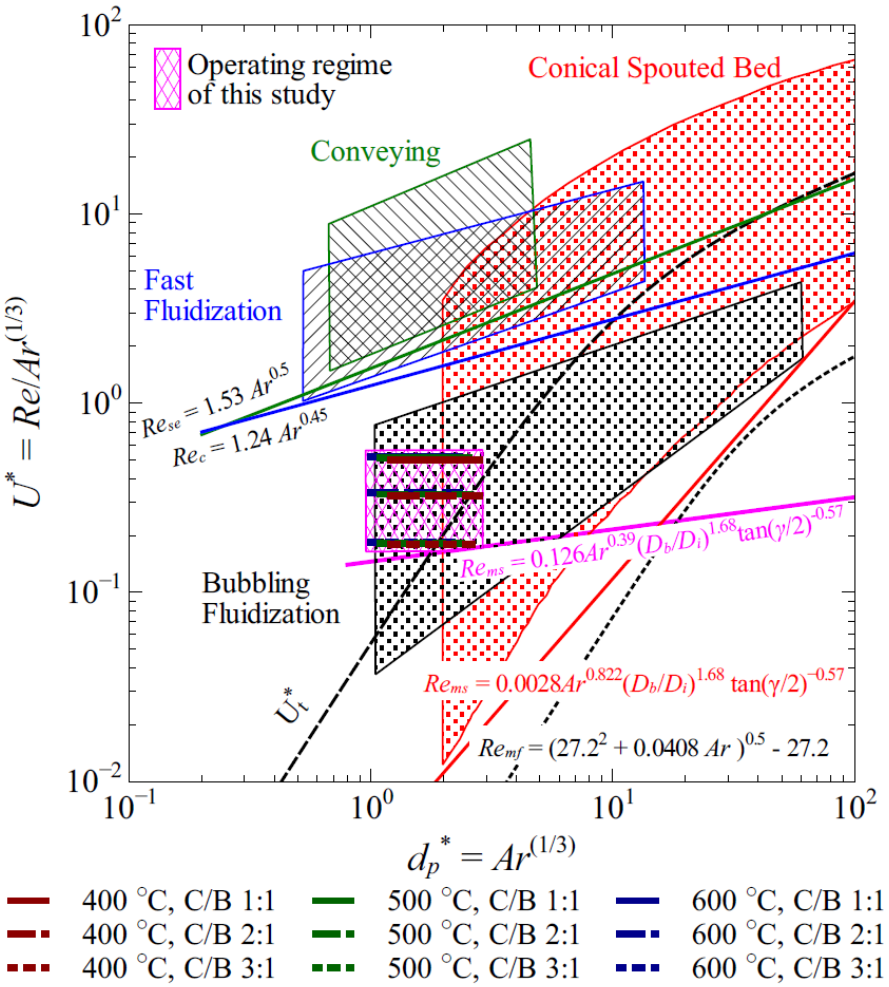

Figure 3-3: Hydrodynamic analysis of the conical spouted bed reactor.

Archimedes number: $Ar = g d_p^3 \frac{\rho_g(\rho_b - \rho_g)}{\mu_g^2}$; Reynolds number: $Re = \frac{u d_p \rho_g}{\mu_g}$, u is the velocity referring to D_b; Re_{ms}, the minimum spouting velocity [69,73]; Re_{mf}, the minimum fluidization velocity; Re_{se}, the critical point where the solids begin to be entrained significantly; Re_c, the critical point where the standard deviation of differential pressure fluctuations reaches a maximum.[78]

3.3.2.Overview of the effect of operating conditions on product distribution

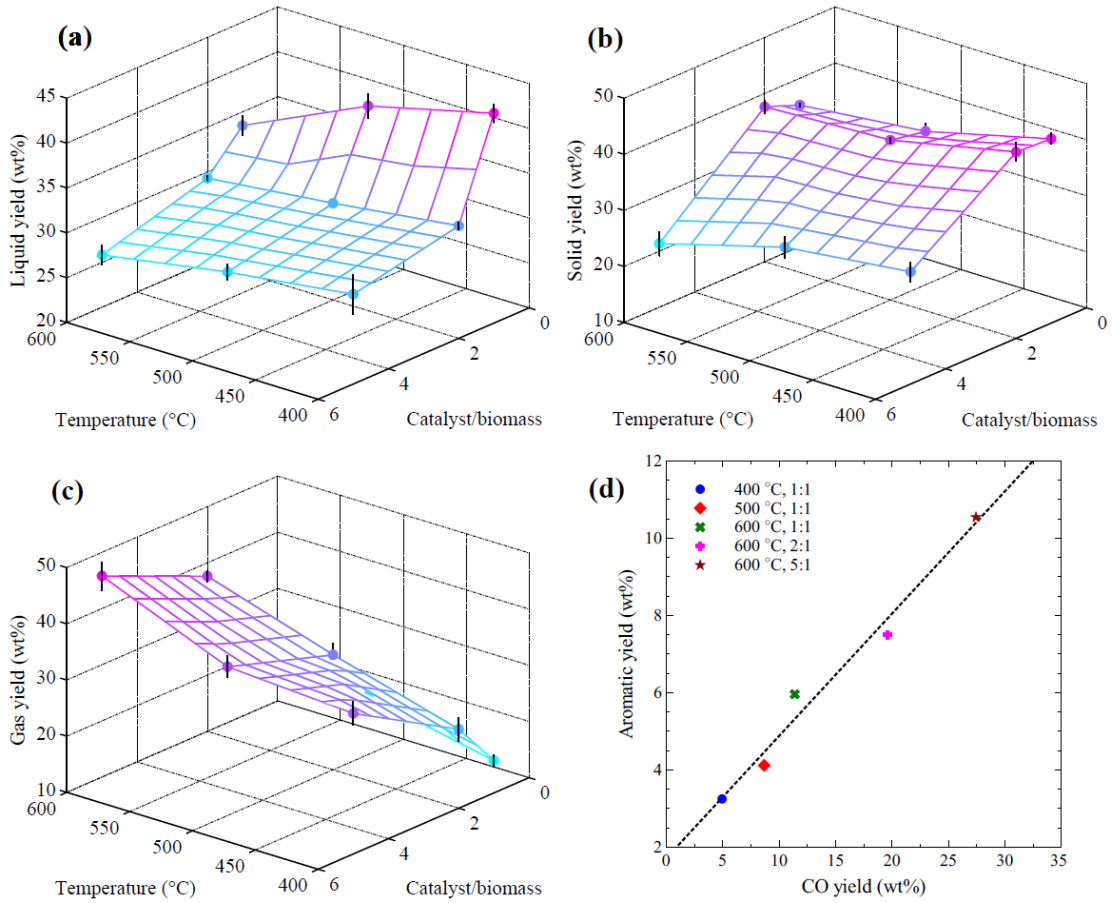

Figure 3-4: Effect of operating conditions on (a-c) the lumped product distribution; and (d) the relationship between aromatics and CO yields. Liquid product includes water and organic compounds. Solid product includes char and coke.

Figure 3-4(a-c) illustrates the overall effect of temperature (400-600 °C) and catalyst to biomass ratio (1-5) on the product distribution, lumped as total liquid, gas and solid. Generally, as the temperature is increased, more gas products and less liquid and solid products are obtained. The catalytic effect is enhanced at higher temperature, thus producing more CO and CO_2 through deoxygenation reactions. At higher catalyst to biomass ratio, higher gas yield and lower liquid and solid yields are observed, due to enhanced catalytic reactions. A detailed discussion on the effect of temperature and catalyst to biomass ratio on the lumped product distribution, bio-oil

selectivity and gas composition is presented in the following sections. Here we note that in all the experiments performed in this study, a clear linear relationship between aromatic yield and CO yield can be observed, shown in Figure 3-4(d). This serves as a validation of the consistency of the effectiveness of the catalytic effect in the spouted bed reactor within the temperature range studied, showing that catalytic deoxygenation results in better aromatic selectivity.

As mentioned in the experimental section, all the experiments were repeated three times and the ones which had the mass balance <90% were discarded. In Figure 3-4(a-c), standard deviations are shown for each experiment in order to show the accuracy and consistency of the experiment. To be specific, at 400 °C, the maximum standard deviation is 2.21% for the liquid product, 2.12% for the solid product and 2.13% for the gas product. The respective values at 500 °C are 2.19% for the liquid product, 1.97% for the solid product; 2.11% for the gas product. At 600 °C, the values are 1.09% for the liquid product, 2.21% for the solid product, and 2.55% for the gas product. The overall mass balance for all the experiments are higher than 90%, within the range of 92.23-104.51%.

3.3.3.Effect of temperature on the lumped product distribution

Figure 3-5(a) shows the effect of temperature on the lumped product distribution. As the temperature increases from 400 °C to 600 °C, the gas yield increases significantly from ~16 wt% to ~25 wt%, whereas the solid and liquid yields decrease from ~43 wt% to ~35 wt% and from ~43 wt% to ~33 wt%, respectively. A similar effect of temperature on the product distribution was observed by Williams and Nugranad,[81] who studied catalytic pyrolysis of rice husks with ZSM-5 catalyst in a fluidized bed reactor. They found that as temperature increases, the liquid and solid yields decrease in parallel to higher gas production. The increase of the gas yield at higher temperature is mostly because of the production of carbon monoxide (see Section 3.3.5), which is caused by the decomposition of the solid fraction and secondary reactions of the liquid fraction to volatile compounds in the reactor at higher temperature.[82] The overall mass balance for

each experiment is also shown in Figure 3-5(a) with the error bars. The errors shown in Figure 3-5(a) represents the real number variation of the total yield measured. The total yields measured (mass balance) are 102.02%, 97.69% and 93.38% for temperatures of 400°C, 500°C, and 600°C, respectively. The standard deviations for the total yields are within the range of 0.415-3.76 for all the experiments studied by changing the temperature.

3.3.4.Effect of temperature on bio-oil distribution

Figure 3-5(c) illustrats the effect of temperature on the bio-oil distribution at a catalyst to biomass ratio of 1. The total aromatic yield increases with temperature (400-600 °C), from 3.25 wt% to 5.96 wt%. In particular, at 400 °C, no monocyclic aromatic hydrocarbons (benzene, toluene, xylene, styrene, and alkylbenzenes) are observed in the bio-oil. As temperature is increased, the yield to monocyclic hydrocarbons increases. The reason for the increase in monocyclic hydrocarbons with temperature can be explained by the promotion of decomposition reactions at higher temperature, producing smaller compounds, which have easier access to the ZSM-5 zeolite pores.[83] The yield to indenes, naphthalenes and heavier polycyclic aromatic hydrocarbons (PAHs) also increase with temperature. The formation of poly-aromatic compounds was attributed by Aho et al.[84] to the Brønsted acidity of the zeolite in the catalyst, which promoted acid catalyzed reactions, such as cracking, dimerization, cyclization and dehydrocyclization. The yield to phenols, benzofurans, and other oxygenates (mainly acetic acid) decrease as the temperature increase. This reflects that higher temperatures enhance deoxygenation reactions, which is also evidenced by the higher yields to CO and CO_2.

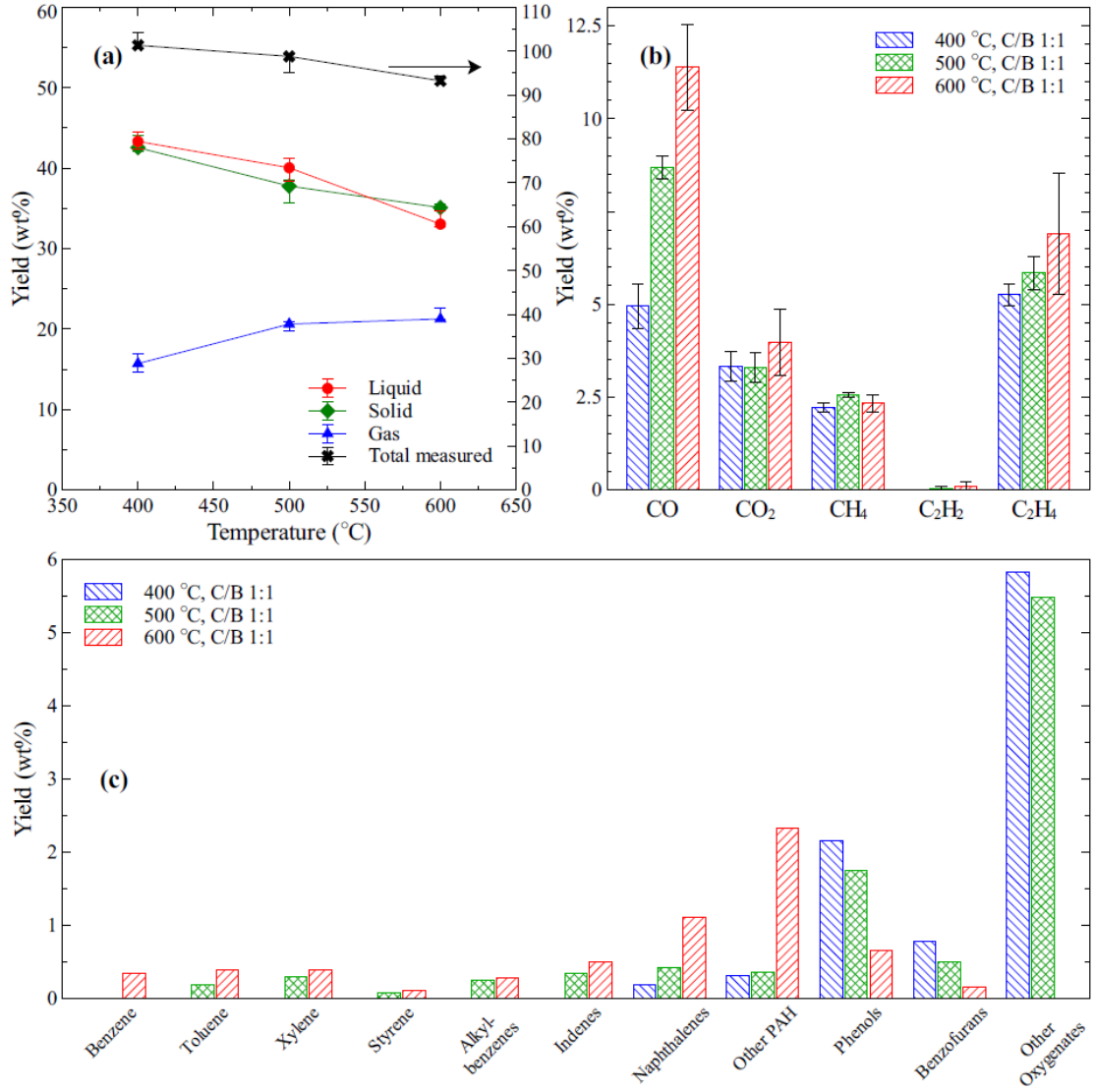

Figure 3-5: Effect of temperature on (a) the lumped product distribution; (b) the gas product distribution and (c) the bio-oil distribution.

Liquid product includes water and organic compounds. Solid product includes char and coke. Alkylbenzenes mainly include benzene, 1-ethyl-2-methyl-, benzene, 1-butynyl-, benzene, 1,2,3,5-tetramethyl-, benzene, ethenylmethyl-, benzene, cyclopropyl-. Indenes mainly include indene, indane, 2-methylindene, 1H-indene, 1,3-dimethyl-. Naphthalenes mainly include naphthalene, naphthalene, 1,2-dihydro-, naphthalene, 2-methyl-, naphthalene, 1-methyl-, naphthalene, 2-ethenyl, naphthalene, 2-ethyl-, naphthalene, 2,7-dimethyl-. Other PAH mainly include phenanthrene, anthracene, fluoranthene, pyrene, and their derivatives. Phenols mainly include phenol, phenol, 3-methyl-, phenol, 2-methoxy-, phenol, 2-methoxy-4-methyl-, phenol, 2,6-dimethoxy-4-(2-propenyl)-, phenol, 2,3-dimethyl-, phenol, 4-ethyl-, vanillin, eugenol. Benzofurans mainly include benzofuran, furfural, benzofuran, 2-methyl-, benzofuran, 2,3-dihydro-, benzofuran, 7-methyl-. Other oxygenates mainly include acetic acid, 1,2-cyclopentanedione, 2-cyclopenten-1-one, 2-hydroxy-3-methyl-, 2-cyclopenten-1-one, 2-methyl-.

3.3.5.Effect of temperature on gas yield

Five major gaseous compounds, CO, CO_2, CH_4, C_2H_2, and C_2H_4 were quantified on-line with FTIR. As shown in Figure 3-5(b), when the temperature increases, the yields of all the gas products increase. CO is the most abundant component in the vapor products and increases significantly from 4.95 wt% to 11.39 wt%, with a temperature increase from 400 °C to 600 °C. The yield to CO_2 and CH_4 does not change much with temperature. The yield to olefins increases from 5.26 wt% at 400 °C to 7 wt% at 600 °C. The CO/CO_2 weight ratio changes from 1.49 to 2.86 when the temperature increases from 400 °C to 600 °C. This is comparable with Zhang et al.,[36] who measured 1.45-2.42 CO/CO_2 weight ratios at temperatures between 400-650 °C. Similar results were also obtained by Wang et al.,[83] who studied catalytic pyrolysis of individual components of lignocellulosic biomass (cellulose, hemicellulose and lignin) at 600 °C. They reported 2.19, 1.56 and 2.07 CO/CO_2 ratios for the catalytic pyrolysis of cellulose, hemicellulose and lignin, respectively. However, not all the relevant analyses of CO/CO_2 ratio are consistent. Olazar et al.[55] reported a CO/CO_2 ratio of 0.08-0.22 for the catalytic pyrolysis of pine sawdust with ZSM-5 catalyst over a temperature range of 400-500 °C. Williams and Nugranad[81] observed CO/CO_2 ratios close to unity after pyrolysis of rice husks with ZSM-5 catalyst at temperatures between 400-600 °C. On the contrary, Wang et al.[83] claimed that the strong acid sites of their H-ZSM-5 catalyst are more active for decarbonylation to produce CO than decarboxylation to CO_2. Evidently, differences in the acidity of the various ZSM-5 catalysts used in each experimental work and differences in feedstock composition make the comparison of gas selectivity difficult.

3.3.6.Effect of catalyst to biomass ratio (C/B) and weight hourly space velocity (WHSV) on the lumped product distribution

In this study, catalyst to biomass ratio was varied by changing the catalyst loading and maintaining the biomass feeding rate and total amount fed. Thus, C/B ratio and WHSV were not controlled independently. Therefore, the effect of catalyst to biomass ratio on product

distribution, shown in Figure 3-6(a), is actually the combined effect of C/B ratio and WHSV. As shown in Figure 3-6(a), the gas yield increases with increasing catalyst to biomass ratio, whereas the solid and liquid yields decrease. Overall mass balance for each experiment is also shown in Figure 3-6(a) with the error bars. The errors shown here also represent the real number variation of the total yield measured. The total yields measured (mass balance) are 93.38%, 104.51% and 93.00% for temperatures of 400°C, 500°C, and 600°C, respectively. The standard deviations for the total yields are within the range of 0.635-7.24 for all the experiments studied by changing the C/B ratio.

Figure 3-7 shows a review of the effect of catalyst to biomass ratio and WHSV on the lumped product distribution. Atutxa et al.[85] studied the catalytic pyrolysis of pine sawdust with ZSM-5 catalyst in a spouted bed reactor at 400 °C. They changed the catalyst to biomass ratio at constant bed height but different catalyst loadings (supplementing the difference with silica sand). They found that as the catalyst to biomass ratio increased the gas yield increased, whereas the solid yield and the liquid yields decreased. Naqvi et al.[86] studied catalytic pyrolysis of paddy husk in a fixed bed reactor with ZSM-5 catalyst. In their setup, C/B ratio and WHSV were not controlled independently. They found that liquid and solid yields decreased with increasing catalyst to biomass ratio (0.5-2), whereas the gas yield increased with the addition of catalyst due to catalyst promoted decarbonylation and decarboxylation reactions.

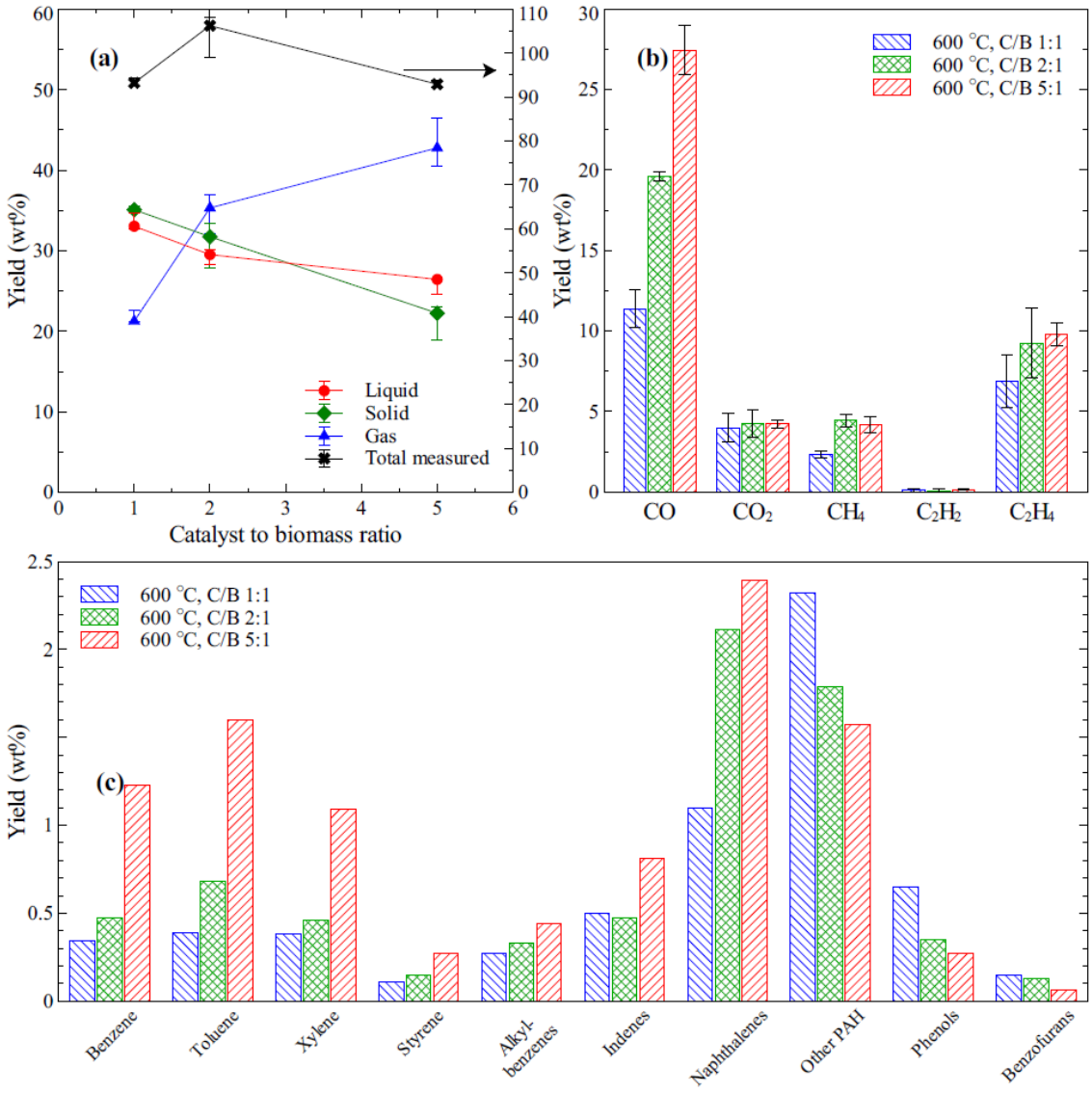

Figure 3-6: Effect of catalyst to biomass ratio on (a) the lumped product distribution; (b) the gas product distribution and (c) the bio-oil distribution. Compound notation is as shown in Figure 3-5.

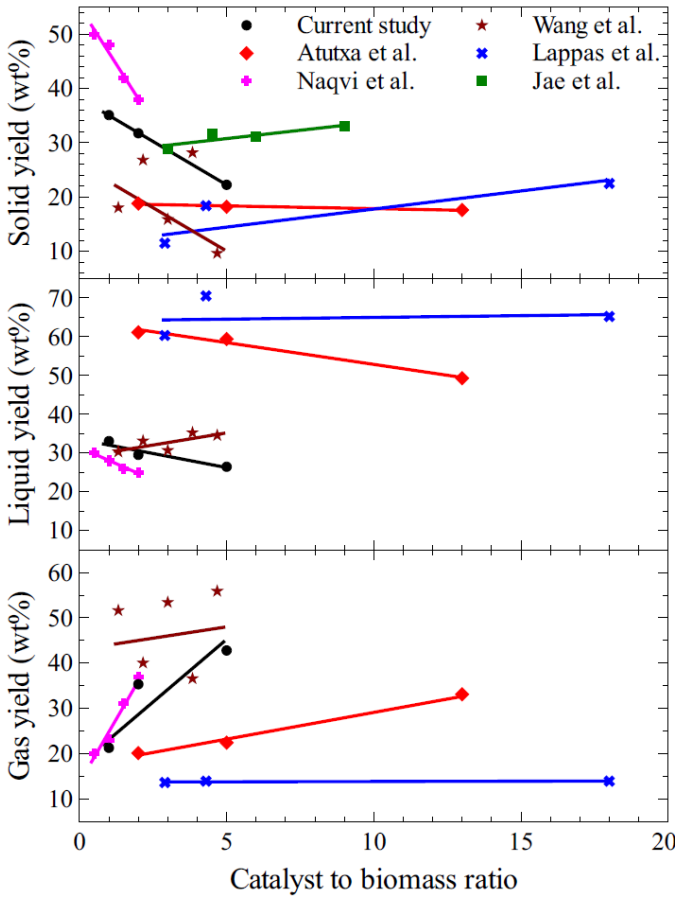

Figure 3-7: Summary of the effect of catalyst to biomass ratio on the lumped product distribution from the current study and the literature. All the reported yields here are in wt%. Solid yields in C% from Jae et al. (Jae et al., 2014) were assumed to equal the solid yields in wt%. feed basis.

Similar trends were also obtained by Wang et al.,[87] who studied catalytic pyrolysis of Douglas fir pellets in microwave with ZSM-5 catalyst, changing C/B ratio and WHSV simultaneously. Lappas et al.,[88] in catalytic pyrolysis experiments of Lignocellulose in a circulating fluidized bed reactor with ZSM-5 catalyst, studied the effect of C/B ratio at constant WHSV. Although they observed similar trends for the yield to liquid and gas with the change in C/B ratio, the yield to solid was reported to be increasing with the catalyst to biomass ratio. An increase in the coke yield with catalyst loading was also observed by Jae et al.,[89] who studied the effect of C/B ratio at constant WHSV in catalytic pyrolysis of wood over ZSM-5 catalyst in a bubbling fluidized bed

reactor. In summary, the effect of catalyst to biomass ratio on liquid and gas distributions is generally consistent between the current study and the literature. The increase of catalyst to biomass ratio results typically in a decrease of the liquid yield, which is converted to gas products. This indicates the effect of the catalyst in promoting deoxygenation reactions, since oxygen removal from the bio-oil proceeds mostly via production of carbon oxides at relatively high temperature (>450 °C).[90] The inconsistency in the literature in the coke selectivity as a function of the catalyst to biomass ratio might be attributed to a combined effect of catalyst to biomass ratio and WHSV. Specifically, by changing catalyst to biomass ratio only, as was done by Lappas et al.[88] and Jae et al.,[89] higher C/B ratios leads to higher coke yields. However, when the catalyst to biomass ratio and WHSV are changed at the same time, such as in this study, Naqvi et al.[86] and Wang et al.,[87] the coke yield decreases with higher catalyst to biomass ratio, due to the correspondingly decreasing WHSVs, higher residence times and bed heights.[21] As discussed previously,[65] the solid pyrolysis product is a mixture of coke and char. Coke as a catalytic product should depended on the catalyst to biomass ratio; whereas, char as a thermal product depends on residence time and bed height. Since char and coke have different origins in the cellulose, hemicellulose and lignin components of biomass,[65] it is fairly difficult to obtain consistency in the observations between researchers using different reactor setups, feedstocks and catalysts.

3.3.7.Effect of catalyst to biomass ratio on bio-oil distribution

Figure 3-6(c) shows the effect of catalyst to biomass ratio on bio-oil composition. The total aromatics yield increases from 5.96 wt% at a ratio of 1:1 to 10.54 wt% at a ratio 5:1. The observed increase in aromatics in the liquid is in good agreement with the literature. A brief summary of the aromatics selectivity in biomass catalytic pyrolysis in the literature is shown in Table 3-5. Despite the differences between the setups, feedstock, and operating conditions, the total aromatics yield (wt%) obtained from catalytic pyrolysis with ZSM-5 lies in the range 0.58-

12.9 wt%. In the current study, the selectivity of monocyclic aromatic hydrocarbons (benzene, toluene, xylene, styrene, alkylbenzenes) is significantly promoted as the catalyst to biomass ratio increased. The total yield to PAHs also increases at higher catalyst to biomass ratios. Formation of PAHs has been shown to be enhanced by catalytic reactions during pyrolysis.[81] In particular, indenes and naphthalenes yields increase with catalyst to biomass ratio, whereas heavier PAHs, such as anthracenes, phenanthrenes and pyrenes, decrease with catalyst to biomass ratio. The yield to phenolic compounds decrease at higher catalyst loadings, illustrating the enhancement of deoxygenation reactions.

As discussed in section 3.3.4 (shown in Figure 3-5(c)), the yield of MAH reaches the maximum 5.96 wt% at 600 °C, showing that the optimum pyrolysis temperature is 600 °C, focusing on the MAH's selectivity, whereas the best pyrolysis catalyst to biomass ratios is 5:1 where the yield of MAH is 10.54 wt% as shown in Figure 3-6(c).

Table 3-5: Selectivity to aromatics and organic liquid in biomass catalytic pyrolysis over ZSM-5 from literature

Ref.	Reactor	Biomass	C/B ratio	Temp. (°C)	Aromatic yield (C%)	Aromatic yield (wt%)	Organic yield (wt%)[b]	Water yield (wt%)
[17]	Pyroprobe	Maple	19	600	~26	~13[a]	~13	-
[22]	Pyroprobe	Microalgae	20	700	22.95	11.48[a]	11.48	-
[62]	Pyroprobe	Algae	1-9	650	2.6-25.8	1.3-12.9[a]	1.3-12.9	-
[24]	Pyroprobe	Microalgae	1-5	550	-	6-17	6-17	-
[91]	Pyroprobe	Pine	9	450	14.88	7.44[a]	7.44	-
[92]	Pyroprobe	Pine	6	600	11.5	5.75[a]	5.75	-
[93]	Pyroprobe	Pine	9	600	18.9-23.4	9.45-11.7[a]	9.45-11.7	-
[63]	Fixed bed	Miscanthus	0.1	450	-	3.15	21.5	26.3
[20]	Fluidized bed	Pine	1.2-20	600	9.5-14	4.75-7[a]	4.75-7	-
[36]	Fluidized bed	Pine	1-5-18	600	4.4-13.9-6.7	2.2-6.95-3.35[a]	2.2-6.95-3.35	-
[88]	Fluidized bed	Lignocell HBS	2.9-18	400	-	0.58-0.64	36.4-30.7	23.9-34.5
[94]	Fluidized bed	Corncob	5	550	-	10.17	13.7	25.6
[28]	Fluidized bed	Pine	0.4	450	-	8.5	20.7	13.0
[95]	Fluidized bed	Hybrid poplar	0.5	500	~10.8	~5.4[a]	~27	~25
[89]	Fluidized bed	Pine	3-9	600	11.9-13.9	5.95-6.95[a]	5.95-6.95	-
[29]	Spouted bed	polyethylene	0.03	500	-	10	25	-
This work	Spouted bed	Miscanthus	1-5	600	-	5.96-10.54	5.96-10.54	-

[a]Aromatics yield (wt%) is the standard yield out of biomass feedstock. Calculation has been performed to approximately convert carbon yield to standard yield by standard yield=1/2 carbon yield.

[b]Organic yield includes the aromatics and other organic compounds, such as ketones, alcohols, aldehydes, acids.

3.3.8.Effect of catalyst to biomass ratio on gas composition

Figure 3-6(b) shows the effect of catalyst to biomass ratio on the gas distribution. As the catalyst to biomass ratio increases (1:1-5:1), the total gas yield increases from 24.70 wt% to 45.79 wt%. The selectivity of CO increases from ~46 wt% to ~60 wt% and the CO/CO_2 weight ratio increases from 2.86 to 6.47 with the increase of catalyst to biomass ratio. Olefin yields also increase with catalyst to biomass ratio, from 7.0 wt% to 9.93 wt%. Combining the experiments of varying catalyst to biomass ratios with those of varying temperature, a clear linear relationship between aromatic yield and CO yield can be observed, shown in Figure 3-4(d). Foster et al.[17] studied catalytic pyrolysis of glucose over ZSM-5 catalysts with varying SiO_2/Al_2O_3 composition. They suggested a possible correlation between CO production via decarbonylation and the formation of aromatics. Also, Wang et al.[83] studied catalytic pyrolysis of cellulose, hemicellulose, and lignin at 600 °C with a catalyst to biomass ratio of 20. They showed a linear correlation between the aromatic yield and catalytic CO yield, from experiments with the three individual biomass components. This shows that the formation of aromatics is from the catalytic reactions of volatile intermediates, which are produced mainly through decarbonylation pathways.

3.3.9.Effect of presence of ZSM-5 on product distribution and bio-oil selectivity

To further understand the effect of ZSM-5 catalyst, experiments with pure catalyst support were performed. Figure 3-8(a) shows the product distribution from catalytic pyrolysis experiments with ZSM-5 catalyst and experiments with its matrix at different temperatures. It is clear that at each temperature, experiments with the matrix produce more char/coke than those with the ZSM-5 catalyst. The results are consistent with Stefanidis et al.,[96] who performed a catalyst screening study for upgrading of biomass pyrolysis vapors. They compared alumina (surface area 160 m^2/g) with the supported ZSM-5 catalyst (surface area 138 m^2/g) and showed that alumina produces more solids than ZSM-5 catalyst during the upgrading process. This means that the matrix alone

has activity due to the presence of alumina sites, which can enhance non-selective pyrolysis reactions, forming coke/char. Because coke and char form on the support, in addition to the supported catalyst, their location, when supported ZSM-5 is used, is not clear in the literature. This study indicates that coke/char formation is highly promoted by the matrix, rather than the ZSM-5 catalyst. Figure 3-8(c) shows the temperature programmed oxidation (TPO) in thermogravimetric analysis (TGA) of the coked ZSM-5 catalyst and the matrix (samples collected by washing the reactor and drying) from experiments at 600 °C and C/B ratio of 1. From the first derivative of the weight loss (DTG), ZSM-5 coke/char TPO shows a low temperature peak and a high temperature peak, which represent char (higher oxygen content in the form of carbonyl groups formed on the matrix)[65] and coke (polyaromatic hydrocarbons mainly deposited in the micropores or cavities of ZSM-5), respectively. In comparison, TPO of the coked/charred matrix shows one peak at the same low temperature, identified as char for the ZSM-5 catalyst, indicating the absence of catalytic reactions inside the catalyst pores and cavities, which lead to coke of polyaromatic nature[65] in the ZSM-5 catalyst.

In terms of bio-oil selectivity, although the Al_2O_3-based matrix has activity, it does not improve the quality of the bio-oil. As shown in Figure 3-8(b), at low temperatures (400 °C and 500 °C), the matrix does not produce any monocyclic aromatic hydrocarbons (MAHs). At 600 °C, small production of MAHs is observed with the matrix, but is significantly lower than that with the ZSM-5 catalyst. Also, the production of MAHs starts at lower temperature (500 °C) with the ZSM-5 catalyst. In the temperature range studied, ZSM-5 produces more aromatics (including MAHs, PAHs, and Phenolics) than its matrix alone, due to the appropriate pore size and acidity of the ZSM-5.[97] The results verify that production of aromatics is favorable in the presence of ZSM-5 catalyst.

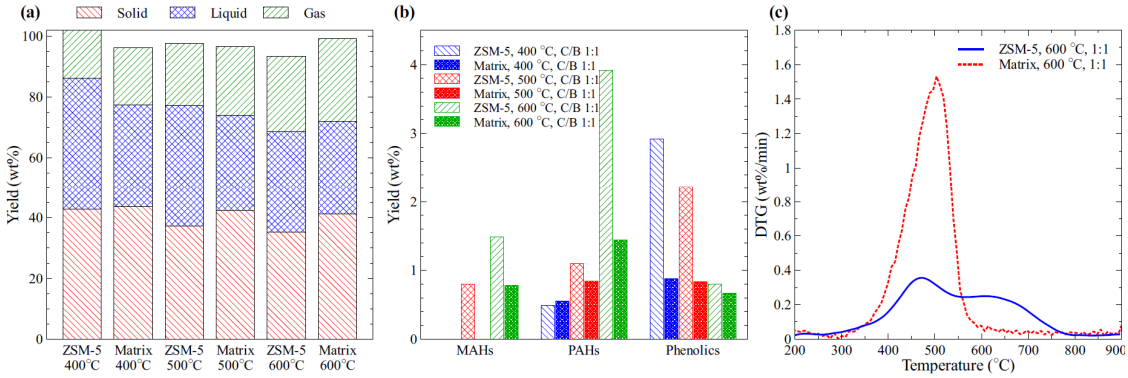

Figure 3-8: Effect of ZSM-5 on (a) the lumped product distribution; (b) the bio-oil distribution; and (c) the solid product TPO.

All six experiments are performed with catalyst to biomass ratio 1:1. TPO shown is of the coked ZSM-5 catalyst and catalyst matrix after catalytic pyrolysis at 600 °C and catalyst to biomass 1:1. MAHs mainly include benzene, toluene, xylene, styrene and alkylbenzenes. PAHs mainly include indenes, naphthalenes, and other PAHs such as phenanthrene, anthracene, fluoranthene, pyrene, and their derivatives. Phenolics mainly include phenols and benzofurans.

3.4. Conclusions

The proposed spouted bed design was shown to be a promising reaction system for biomass catalytic pyrolysis, providing excellent mixing, superior biomass feeding and selectivity towards deoxygenated products. In agreement with relevant literature reports, high temperatures and catalyst loadings favored aromatics production, via deoxygenation reactions that formed carbon oxides. The catalyst support produced more coke and less monocyclic aromatic hydrocarbons than the ZSM-5 catalyst, due to its uncontrolled catalytic activity and lack of shape selectivity. The reactor operating conditions were mapped to product selectivity showing high selectivity to aromatics at 600 °C and high catalyst to biomass ratios.

CHAPTER 4 BIOMASS CATALYTIC PYROLYSIS IN MULTIPLE REACTOR CONFIGURATIONS: A COMPARISON OF SPOUTED BED REACTOR AND PYROPROBE-GC-MS

The results of this Chapter have been submitted for publication to Bioresource Technology, 2015.

4.1. Introduction

Multiple reactor configurations have been designed to maximize the yield to bio-oil, the most desirable pyrolysis product. Generally, according to the sequence of biomass pyrolysis and biooil upgrading, two methods exist: *in situ* CFP, and *ex situ* catalytic upgrading. For *in situ* CFP, pyrolysis and upgrading occur in a one-step catalytic process, whereas *ex situ* upgrading requires transporting the pyrolysis vapors to a secondary reactor. Several recent studies have been performed, focusing on the comparison of the two methods. Wan et al.[98] constructed an *ex situ* reaction system for a micropyrolyzer. They studied *in situ* and *ex situ* catalytic pyrolysis of oak and levoglucosan, and much higher aromatic yields were observed for the *in situ* case. They argued that residence times in the *in situ* microreactor were very high (greater than 10 s), which leads to high conversions to secondary products (aromatics and coke). Nguyen et al.[99] studied *in situ* and *ex situ* pyrolysis of woodchips at constant catalyst to biomass ratio. They found a higher degree of oxygen removal with the *ex situ* configuration. They concluded that this could be attributed to the temperature gradient created by heating the catalyst and biomass at the same time with the *in situ* method, as opposed to the *ex situ* upgrading method where the catalyst is pre-heated in a downstream unit. Wang et al.[100] studied *in situ* and *ex situ* catalytic pyrolysis of poplar at 20:1 catalyst to biomass ratio and 700 °C in a microreactor system. They found significantly higher yields to permanent gas and lower yields to aromatics during the *ex situ* method. They also observed significantly more carbonaceous residue when performing *in situ* CFP. The differences between *in situ* CFP and *ex situ* CFP are mostly in the residence time and the corresponding impact caused by promoting char formation.

Different reactor scales are used in biomass catalytic pyrolysis. Fluidized bed reactors are widely applied due to their scalability, excellent mixing and heat transfer characteristics, continuous operation, and uniform catalyst distribution.[28,65,95] Studies regarding catalytic fast pyrolysis (CFP) in fluidized bed reactors are widely available in the literature.[20,28,89,95,101,102] Spouted bed reactors are one type of fluidized bed reactors, which is adept at handling large particles and particle size distributions, providing excellent mixing and handling differences in feedstock and particle densities.[2] Bilbao and coworkers[55] studied CFP of sawdust over ZSM-5 catalyst in a spouted bed reactor and discussed the benefits of the spouted bed configuration with respect to biomass pyrolysis. The design and hydrodynamic analysis of a spouted bed reactor together with an integrated study of the effect of operating conditions on biomass catalytic pyrolysis product distribution was shown in Chapter 3.

Besides the industrial-scale and bench-scale reactors, a micro-scale reactor setup, pyrolysis gas chromatography (PyGC), offers an attractive technique for studying the pyrolysis of biomass. In a PyGC, reactions occur in a microreactor, and all products can be analyzed in a closed automated system. Although PyGC has several drawbacks including inefficient mixing of catalyst and biomass, experimental error created by irregularities in biomass feedstocks, and inability to be scaled up to a continuous industrial process,[20] it does offer excellent control of temperature and heating rate. Moreover, micropyrolyzers are often far more simple than bench scale setups, and have a pre-built in liquid collection system.[98] In the PyGC, only small amounts of biomass and catalyst are required. The ease of operation makes it a widely applied flexible tool to simulate the CFP equivalent of bench-scale and industrial scale reactors.[17,21–25]

Comparing these reactor configurations; namely the PyGC with *in situ* and *ex stiu* catalytic upgrading, and the spouted bed allows for understanding the real specialty of the spouted bed compared to other reactor setups, and also creates a better understanding of why and how the spouted bed benefits the production of aromatics in the bio-oil. (See Table 3-5)

The objective of this study is to further explore the effect of operating conditions, such as heating rate and residence time on the product distribution, by comparing different reactor configurations. The effect of char formation on the catalyst activity during pyrolysis and the impact of reactor configuration on liquid selectivity are also discussed by comparing *in situ* and *ex situ* catalytic upgrading in PyGC. This study also reflects the effectiveness of using the microscale PyGC to predict the performance of large scale reactors. Results from different reactor configurations, including PyGC with *in situ* CFP, PyGC with *ex situ* catalytic upgrading and spouted bed reactor CFP, are presented. The differences in WHSV, heating rate, catalyst bed height and preheating of the catalyst bed among different reactor configurations are compared and discussed.

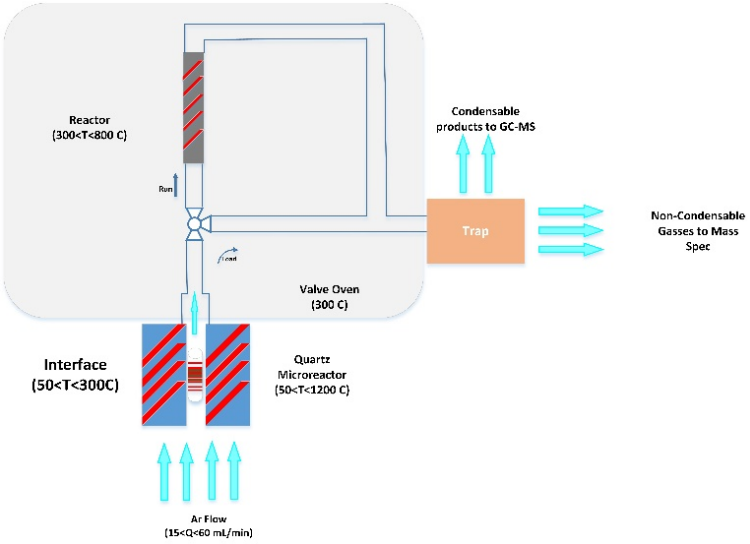

Figure 4-1: Simplified flow path for PyGC system.

4.2. Methods

4.2.1.Feedstock and Catalyst

Miscanthus × giganteus is used as biomass feedstock in this study. The preparation of miscanthus (milling and drying) and its proximate and ultimate analysis were discussed in Section 3.2 and Du et al.[103] Commercial spray-dried ZSM-5 catalyst from W.R. Grace & Co is used as the catalyst in

this study. Characterization of this catalyst including the morphology and pore size distribution has been shown in Table 3-2.

4.2.2.Experimental Setup and Procedure

Pyrolysis experiments were performed using a CDS Analytical Pyroprobe 5200HP (CDS Analytical Inc.). Figure 4-1 shows a simplified schematic of the reaction system. During the experiment, biomass was placed in the quartz microreactor and held in place by quartz wool. A constant loading of 5 mg (biomass and catalyst mixture) for *in situ* CFP and 2 mg (biomass) for *ex situ* upgrading was maintained. In the *in situ* study, catalyst and biomass were well mixed. The microreactor was inserted into the probe, and then placed in the pyrolysis interface, maintained at 300 °C downstream for the duration of the experiment to prevent condensation of pyrolysis vapors. The probe was then heated to the desired pyrolysis temperature and maintained isothermally for a probe time of 20 seconds, which was proven to be sufficient to volatilize all the biomass in the microreactor.[59] The heating rate was 20 °C/ms.[60] The pyrolysis vapor products were carried by the Ar carrier gas from the microreactor to either the cold trap (*in situ*), or a secondary fixed bed reactor (*ex situ*) followed by the cold trap. Condensable liquids were adsorbed onto the trap and permanent gas was carried through to an online mass spectrometer (MS, Agilent 5975C), externally calibrated for H_2, CO, CO_2, CH_4, C_3H_6 and Ar. All experiments were performed at probe and reactor temperatures of 600 °C. After pyrolysis, condensed vapors were desorbed from the trap and transferred to a gas chromatograph equipped with a mass spectrometer (GC-MS, Agilent 6890 GC with 5973N MS). The GC column was an Agilent DB-5 (0.32 μm ID, 30 m length), with a constant He flow of 1 mL/min, an inlet temperature of 270 °C, and split ratio of 75:1. The GC-MS was calibrated by injecting external standards through the PyGC system. Due to the wide range of compounds detected from the PyGC (over 350 total individual compounds detected), only those with a qualifier greater than 75 were quantified, using the semi-quantification method was applied. Solid yields were determined by oxidizing the

remaining organic residue at 800 °C while monitoring the CO_2 and CO signals on the MS. Char and coke in solids produced from each configuration were also measured by a Q-500 thermogravimetric analyzer (TGA) from TA instruments using temperature programmed oxidation (TPO).

The experimental conditions and operating procedure of the spouted bed reactor have been described in Chapter 3. In order to compare the results between PyGC and spouted bed, the feedstock, temperature and catalyst to biomass ratio were kept identical. A summary of the experimental conditions for pyrolysis in the PyGC and the spouted bed reactor is shown in Table 4-1.

Table 4-1: Experimental conditions for pyrolysis and catalytic upgrading in PyGC and spouted bed reactor

Configuration	*In situ*	*Ex situ*		Spouted bed
	(Pyrolysis+Upgrading)	Pyrolysis	Upgrading	(Pyrolysis+Upgrading)
Temperature [°C]	600	600	600	600
Catalyst/biomass	1-10	-	1-10	1-5
Flow rate [mL/min]	50	50	50	5000
Heating rate [C/sec]	2e4	2e4	1e5[a]	1e5[a]
Catalyst preheat	No	-	Yes	Yes
Catalyst bed length/height [cm]	0.5	-	0.026-0.26	2.5-5.3
WHSV[b] [hr^{-1}]	18-180	-	10.8-108	12-60

[a]Estimated based on reactor dimensions and operating condition. For example, in spouted bed, the parameters for the calculation are the inlet diameter (0.635 cm), flow rate (5 L/min), temperature difference between inlet and catalyst particle (500 °C) and distance between inlet and catalyst particle (1 cm). It is not considering the time for heat transfer between biomass particle and catalyst particle.
[b]WHSV is defined as the mass flow rate of feed divided by the mass of catalyst in the reactor. Calculation of *ex situ* upgrading WHSV uses the effective catalyst to feed (volatile products from thermal pyrolysis) ratio by assuming 60 wt% volatile products after thermal pyrolysis

4.3. Results and Discussion

In this study, the effect of different catalyst to biomass ratios on the product distribution was studied using the three previously described reactor configurations: a) *in situ* CFP in PyGC, b) fast pyrolysis with *ex situ* catalytic upgrading in PyGC and c) *in situ* CFP in the spouted bed reactor. Only PyGC experiments with a carbon balance of 100% +/- 15% were accepted. All experiments were performed in triplicate. All the experiments in the spouted bed reactor were also repeated three times and the ones with mass balance ≥90% were kept and shown. The results obtained by using the PyGC were compared with the corresponding results obtained with the bench scale spouted bed reactor.

4.3.1. Lumped product distribution

Figure 4-2(a) shows the yield to solids, liquids, and permanent gas from *in situ* CFP. The overall mass balance is only around 60 wt% due to the presence of water, which cannot be measured. Generally, the gas yield increases with catalyst to biomass ratio, whereas liquid and solid yields do not change much as a function of catalyst to biomass ratio. As shown in Figure 4-2(b), similar trend in lumped product distribution is observed in *ex situ* upgrading. Comparing the *in situ* CFP with *ex situ* upgrading experiments, the solid yield remains essentially the same. *In situ* CFP produces much higher liquid yields and lower overall gas yields than *ex situ* upgrading. The results regarding liquid and gas yields are in good agreement with Wang et al.,[100] who performed CFP at 20 C/B and 700 °C in a microreactor. The conclusion that an *in situ* CFP reaction system results in the highest yield to liquids is also consistent with Compton et al.,[104] who found slightly higher liquid yields for oak pyrolysis using a similar microreactor method in comparison to an external packed bed reactor.

Compared with the experiments performed in PyGC, catalytic pyrolysis in spouted bed shows a clearer catalytic effect. As shown in Figure 4-2(c), the clear trend for decrease of liquid and

increase of gas yields as catalyst to biomass ratio increases is consistent with the literature.[85,89,90] The explanation for the decrease of solid (coke and char) yield is attributed to the simultaneous change of both catalyst to feed ratio and WHSV during the experiment.[61] Comparing the *in situ* CFP in PyGC with the CFP in the spouted bed, a higher gas yield and lower liquid yield (assuming the unmeasured water yield being solely responsible for the mass balance gap) in the spouted bed implies that the more enhanced catalytic reactions in spouted bed are possibly due to the preheating of the catalyst bed (Table 4-1).

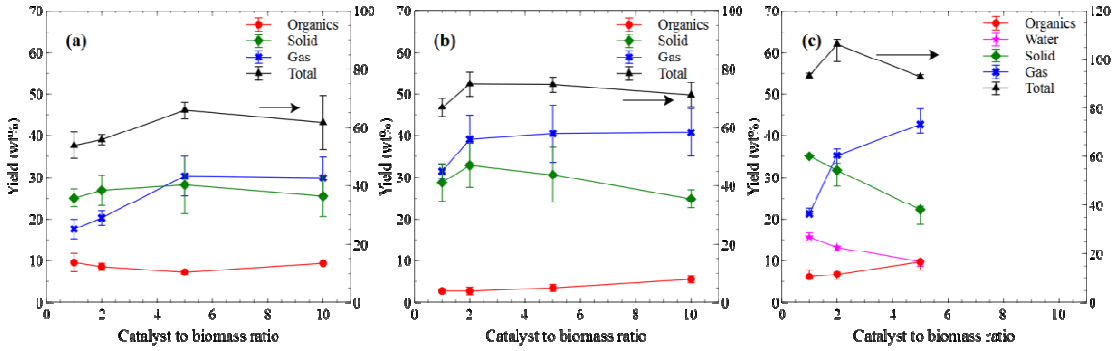

Figure 4-2: Comparison of the overall yields to bio-oil components, solids, and permanent gas for a) *in situ* catalytic fast pyrolysis, b) *ex situ* vapor upgrading, and c) spouted bed reactor under 600 °C and 1:1-10:1 catalyst to biomass ratios.

4.3.2.Liquid product distribution

In Figure 4-3(a), at low catalyst to biomass ratios, oxygenated species such as phenols, hexadecanoic and octadecanoic acids, ketones, esters, and furans dominate in the liquid products from *in situ* CFP. As catalyst to biomass ratio increases, aromatic compounds including benzene, toluene, xylene, styrene and alkyl benzenes (e.g. ethyl benzene), naphthalenes and indenes all increase. At high catalyst to biomass ratios, the products are mostly aromatic hydrocarbons, with oxygenated species only making up a small portion of the liquid products. Similar trends in the liquid product distribution as a function of catalyst to biomass ratio are also observed in *ex situ* PyGC and spouted bed reactor.

The *ex situ* catalytic upgrading results in a better selectivity to aromatic hydrocarbons at all catalyst to biomass ratios compared with *in situ* CFP. These results are consistent with Nguyen et al. who found more deoxygenated products with *ex situ* upgrading.[99] The higher selectivity to aromatic hydrocarbons in *ex situ* upgrading is most likely due to the relief of catalyst deactivation caused by char formation. This is also verified by the observation that the difference between *ex situ* upgrading and *in situ* CFP diminishes as catalyst to biomass ratio increases.

Comparing the spouted bed reactor with PyGC, the yield of aromatics is 6.0-10.5 wt% in the spouted bed, whereas the yield of aromatics recorded in the PyGC is 7.1-8.9 wt%. The similar aromatics yields between the two reactor configurations can be attributed to the similar residence time. The effect of residence time on aromatics production has been studied by Carlson et al.,[20] who compared CFP of wood in a fluidized bed reactor to that in the PyGC. They found that the PyGC maximized yield to aromatic compounds and coke compared with their fluidized bed reactor, due to the high residence time in the PyGC. It should be noted that the study of the effect of residence time on the aromatics production should be based on the prerequisite that catalyst is not completely or mostly deactivated by the formation of char during the *in situ* CFP. From the comparison of *in situ* and *ex situ* in PyGC, it is very clear that catalyst deactivation caused by char formation is very significant in *in situ* CFP in PyGC.

Overall from the comparison of the liquid aromatic hydrocarbon yields between *in situ* and *ex situ*, it is not unreasonable to claim that the enhanced catalytic effect, producing mostly deoxygenated compounds, in *ex situ* experiments is attributed to the prevention of char formation compared with the *in situ* configuration. Moreover, similar aromatics yields between the CFP in the PyGC and that in the spouted bed are mainly attributed to the similar residence time.

In this study, it has been shown that vapor residence time plays a very important role in aromatics production in the spouted bed reactor and the PyGC. In essence, this translates into the extent and

dominance of primary and secondary pyrolysis reactions. Mettler et al.,[105] in their critique of the top 10 fundamental challenges facing biomass pyrolysis, claimed that primary reactions occurred very rapidly to form furans and levoglucosan, which can either evaporate or break down to form secondary products, such as pyrans and light oxygenates. Patwardhan et al.[21] studied the primary and secondary pyrolysis of cellulose using a microreactor and a fluidized bed reactor. They found that most of the primary products were very reactive at pyrolysis temperatures and can undergo secondary reactions. The extent of these reactions depends on their residence time inside the pyrolysis reactor. Accordingly, in CFP, primary pyrolysis produces reaction intermediates of mostly oxygenated compounds, whereas the secondary pyrolysis in CFP refers to catalytic reactions of small organic compounds in catalytic pore systems.[59] In this study, shown in Figure 4-3, all the liquid products including aromatic hydrocarbons and oxygenates are considered as secondary pyrolysis products. The formation of these compounds is highly dependent on the catalytic performance, which are mostly affected by catalyst activity (whether deactivated by char/coke formation) and vapor residence time (contact with catalyst).

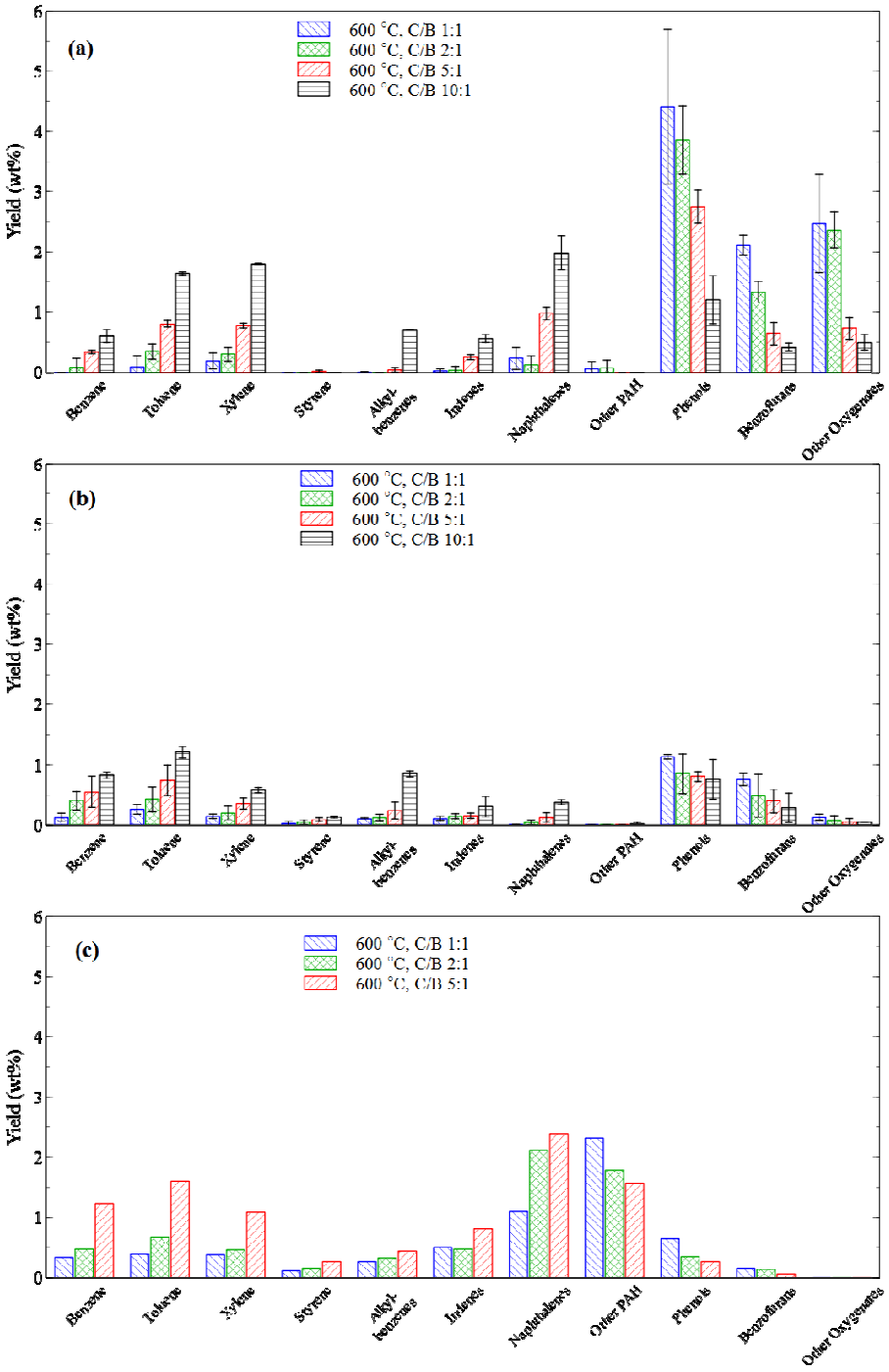

Figure 4-3: Comparison of the bio-oil distribution for a) *in situ* catalytic fast pyrolysis, b) *ex situ* vapor upgrading, and c) spouted bed reactor under 600 °C and 1:1-10:1 catalyst to biomass ratios.

4.3.3.Gas product distribution

A detailed gas analysis is presented in Figure 4-4. The overall gas yield increases as a function of catalyst to biomass ratio for all the reactor configurations. In the PyGC, CO_2 is the most dominant gas component, whereas in the spouted bed, CO dominates in the gas products. The difference in the CO and CO_2 production between the PyGC and the spouted bed might be attributed to the promoted conversion of furanic compounds into CO in the spouted bed. This is, to some extent, verified by the significant decrease in the yields of benzofuran and other oxygenates shown in Figure 4-3. Small amounts of olefins are detected in experiments in the PyGC but were not quantified in this study. In contrast, significant amounts of ethylene are observed during biomass catalytic pyrolysis in the spouted bed reactor. The observation that the fluidized bed configuration produces CO as the dominant gas component, whereas the micro reactor produces mainly CO_2 and minor amounts of CH_4 and olefins, is consistent with Patwardhan et al.,[21] who studied cellulose pyrolysis in both microreactor and fluidized bed.

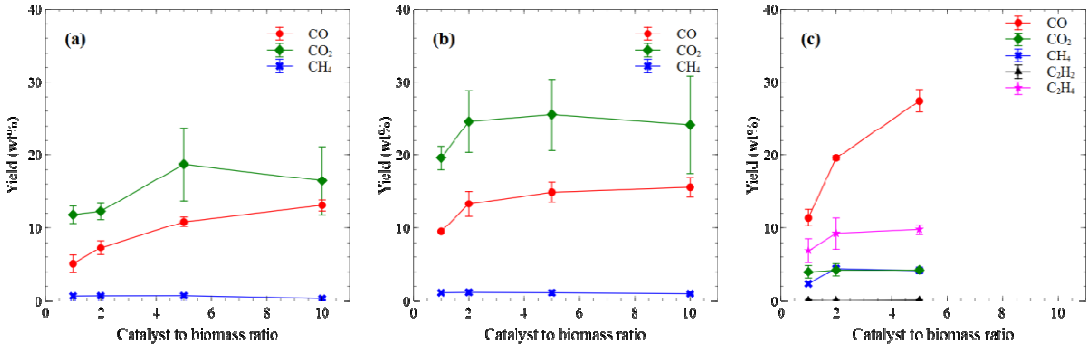

Figure 4-4: Comparison of the gas distribution for a) *in situ* catalytic fast pyrolysis, b) *ex situ* vapor upgrading, and c) spouted bed reactor under 600 °C and 1:1-10:1 catalyst to biomass ratios.

Figure 4-5 is a plot of CO yield vs. aromatics yield in the catalytic pyrolysis of miscanthus using (a) *in situ* pyroprobe, (b) *ex situ* pyroprobe, (c) spouted bed reactor. There is a clear positive trend between the yield to CO and that to aromatics. The trend in the spouted bed appears to be linear,

whereas the PyGC results indicate this trend may be exponential. No trend is apparent between CO_2 yield and lumped aromatics and coke yield, which is in good agreement with our previous work.[103,106] These trends are most likely a result of the greater proclivity of strong acid sites in the H-ZSM-5 catalyst to decarbonylation (resulting in CO) rather than decarboxylation (resulting in CO_2).

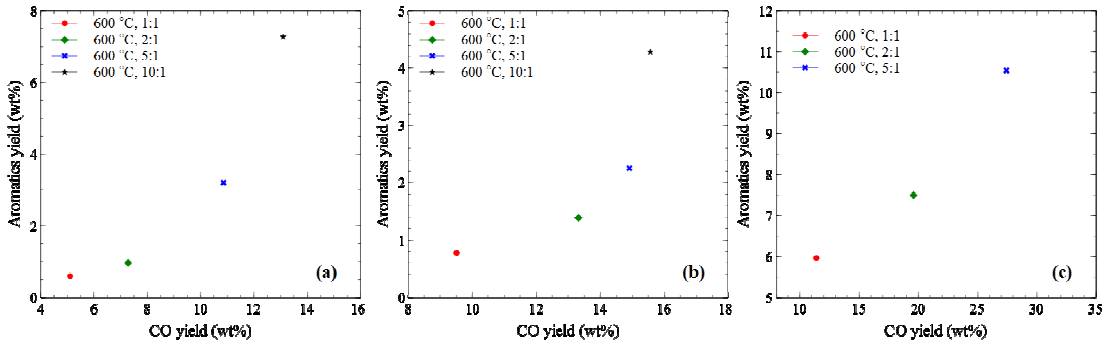

Figure 4-5: CO yield vs aromatics yield in catalytic pyrolysis of miscanthus using (a) *in situ* pyroprobe, (b) *ex situ* pyroprobe, (c) spouted bed reactor

4.3.4.Formation of Coke and Char

Char is defined as the organic solids remaining after thermal pyrolysis. Coke is defined as carbonaceous deposits attributed to catalytic reactions. For the *ex situ* case, char yield represents what remains in the reactor after thermal pyrolysis, and the coke yield represents the coke deposited in the downstream upgrading reactor. The formation of coke can cause a loss of catalytic activity during the *in situ* CFP and *ex situ* upgrading via micropore blockage.[18,107] The formation of char, in CFP, can also cause the catalyst deactivation by catalyst outer surface coverage.[29] Thus the separation of thermal treatment and catalytic treatment (*ex situ*) is advantageous, in the sense that the catalyst will not undergo a loss of activity from char formation.[107]

In this study, the characteristics of char and coke from different reactor configurations is investigated by performing Temperature programmed oxidation (TPO) of char and coke in a thermogravimetric analyzer (TGA). The TPO peak areas are not comparable between the PyGC and the spouted bed reactor, due to the varying catalyst to feed ratios used in each configuration. The first derivative thermogram (DTG) of the *in situ* CFP experiment has one large peak at 485 °C, and a smaller higher temperature peak at 610 °C. The DTG of the char from the *ex situ* CFP in the PyGC exhibits a single peak at 425 °C, with a shoulder at 325 °C. The coke deposited in the catalyst from the *ex situ* CFP in PyGC shows a single broad peak with peak temperature at 670 °C. A lower temperature DTG peak indicates less condensed carbonaceous compounds, or the presence of oxygen in the coke/char.[29] These results indicate that the structure of char from the CFP method is different from that of thermal pyrolysis, resulting in the notion that the catalyst has an effect on the structure of thermal char. Mettler et al.[108] showed a reaction scheme for cellulose thermal pyrolysis, where different sources of char named primary char and secondary char are proposed. In their scheme, the secondary char was formed from the secondary pyrolysis of furanic compounds. Thus in the presence of catalyst, it is reasonable to assume that the difference in char structures between the *in situ* and *ex situ* upgrading is because of catalyst interaction during the formation of secondary char in *in situ* CFP. Moreover, it is observed that the coke fraction on catalyst is significantly reduced in *ex situ* upgrading compared with in situ CFP, due to the higher effective catalyst to feed ratio (biooil from thermal pyrolysis is the feed for *ex situ* upgrading whereas biomass is the feed for *in situ* CFP). Interestingly, the DTG of chars from *in situ* CFP and that from spouted bed have exactly the same peak temperatures. This means that although differences exist between the two configurations, they do not affect the char/coke structure. This further means that char/coke are quite stable during CFP. Once formed, they do not react with other compounds in the subsequent secondary pyrolysis.

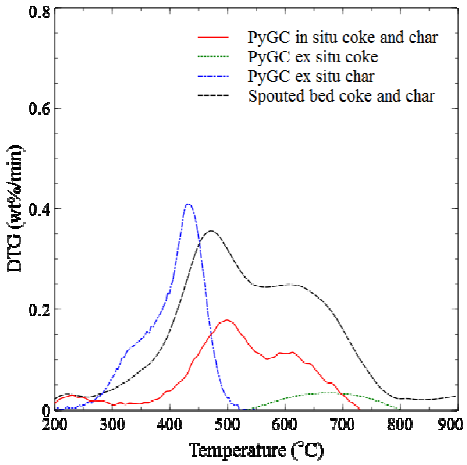

Figure 4-6: DTG of carbonaceous deposits collected from the pyroprobe reactor (*in situ* and *ex situ*) and the spouted bed reactor at 600 °C and catalyst to biomass ratio of 5:1 for PyGC and 1:1 for spouted bed.

4.4. Conclusions

A PyGC was tested for the pyrolysis of biomass in two different configurations, *in situ* CFP in a single microreactor, and *ex situ* vapor upgrading in a downstream fixed bed reactor. These configurations were also compared to a laboratory scale spouted bed reactor. The PyGC showed some ability to predict trends in the bio-oil, permanent gas and solid product yields of the bench scale spouted bed, but the quantitative product distribution is not the same due to different operating conditions (mainly heating rates and residence times). The most significant findings in this study are summarized as follows:

- *In situ* CFP produces higher liquid yields and lower overall gas yields than *ex situ* upgrading. The higher gas yields and lower liquid yields measured in the spouted bed compared with the *in situ* CFP in PyGC implies an enhancement of the catalytic reactions in the spouted bed, due to its better heat transfer characteristics. Overall, the heating rate or preheating of the catalyst bed is the most dominant factor that affects the lumped product distribution.

- The enhanced catalytic effect in *ex situ* experiments, resulting in mostly deoxygenated compounds, is attributed to the prevention of char formation compared with *in situ* CFP.
- In the PyGC, CO_2 is the most dominant gas component, whereas in the spouted bed, CO dominates the gas products. Significant amounts of olefins are detected in experiments using the spouted bed, but are not significant in the PyGC. A clear trend of the yield to CO increasing with the yield to aromatics is observed in all the three reactor configurations.
- The structure of char from the *in situ* CFP method is different from that of thermal pyrolysis, resulting in the notion that the catalyst has an effect on the structure of thermal char. The DTG of chars from *in situ* CFP and that from spouted bed have the exact same peak temperatures, reflecting the similarity in char/coke structure.

CHAPTER 5 CHARACTERISTICS AND ORIGINS OF CHAR AND COKE FROM FAST AND SLOW, CATALYTIC AND THERMAL PYROLYSIS OF BIOMASS AND RELEVENT MODEL COMPOUNDS

The results of this Chapter have been published in Green Chemistry, 2013.[65]

5.1. Introduction

In biomass pyrolysis, slow or fast, catalytic or thermal, there is always some solid residue (typically, a mixture of coke and char, depending on the pyrolysis process) produced in parallel to non-condensable products and condensable bio-oil plus water.[13,26,27] However, the definition of coke and char varies among different studies. Elordi et al.[29] studied the Catalytic fast pyrolysis of polyethylene in a spouted bed reactor at 500°C, using HZSM-5, HY, Hβ catalysts. They defined coke as the carbonaceous material deposited on the catalyst. They claimed that the combustion of coke in the meso- and macro-pores of the catalyst shows a temperature programmed oxidation (TPO) peak at lower temperatures, compared with the coke located inside the zeolite crystal channels due to differences in composition. They also observed coke outside the zeolite crystals with heterogeneous sizes between 10 and 50 nm, using transmission electron microscopy (TEM). In the review of biofuel production by Huber and Corma,[30] coke was defined as the organic fraction that could only be removed from the catalyst *via* calcination. Char was defined as the organics deposited in the reactor as a result of thermal decomposition, but not on the catalyst. Triantafyllidis et al.[31] studied the Catalytic fast pyrolysis of beech wood in a fixed bed reactor at 500 °C, using mesoporous aluminosilicate and conventional Al-MCM-41 catalysts. They considered coke as a lump of the solid carbonaceous residues catalytically produced in the reactor as a separate phase to the catalyst, as well as the solid residues deposited on the catalyst surface due to thermal and catalytic cracking. Generally, coke is considered as the catalytic product, whereas char is the residue formed *via* thermal deconstruction. This definition is widely accepted, and many researchers describe the solid residue after thermal pyrolysis as char.[27,32,33] Based on

this definition, primary decomposition and secondary polymerization contribute to char formation,[34,35] while coke formation is mainly attributed to catalytic polymerization of small biomass molecules inside catalyst pores.[36]

Generally, coke formation leads to catalyst deactivation and results in undesirable product selectivity in biomass pyrolysis,[6] whereas char may or may not deactivate the catalyst, depending on the location of its formation. However, the real reason for catalyst deactivation due to coke and char is not well understood. Carlson et al.[59] studied the effect of ZSM-5 deactivation (due to coking) on the selectivity of glucose Catalytic fast pyrolysis in a pyroprobe reactor. Coke yields of the order of 33 – 45 mol% (moles of carbon in coke per total moles of carbon) were measured, which translates to about 15 wt% coke yield on glucose mass basis. In experiments with zeolite to glucose ratios of 19 (thus, coke on catalyst of about 0.79 wt%), they observed positive effects of coke formation on biomass pyrolysis selectivity. On the contrary, Aho et al.[28] performed Catalytic fast pyrolysis experiments with pine and ZSM-5 in a fluidized bed reactor at 450 °C, but with low zeolite to biomass ratio (0.4), showing that coking of the zeolite leads to a significant decrease in catalytic activity. Also, Cheng and Huber[18] investigated the conversion of furan over HZSM-5 in a fixed-bed reactor at 600 °C. A continuous loss of catalytic activity was observed as the amount of coke increased on the catalyst surface. In most studies, carbon and char are lumped as “coke”, but according to Aho et al.[28] the char to coke ratio after pyrolysis of pine sawdust with ZSM-5 is about 2:1.

As indicated above, significant effort has been devoted on the characterization of biomass char and coke. However, most of the published work focuses on thermal chars,[109–111] leading to a lack of understanding of the mechanisms and effects of char and coke formation when catalyst is introduced in the pyrolysis. This work focuses on studying catalyst deactivation and the effectiveness of model compounds, in particular glucose and cellulose, as compared to pine from the perspective of comparing their pyrolysis char and coke characteristics. The objective of this

study is to explore the difference between coke and char residues and explore the origin of their formation and their contribution to catalyst deactivation during biomass catalytic pyrolysis.

5.2. Experimental section

5.2.1. Experimental setup

Two experimental setups are used in the pyrolysis experiments. Slow pyrolysis is performed in a fixed bed quartz reactor (1 inch o.d. and 24 inch length), which is heated in a horizontal tube furnace. Fast pyrolysis is studied in a specially designed spouted bed reactor. In the spouted bed reactor, biomass is fed with an auger feeder at the bottom and enters the reactor *via* entrainment with 4-10 L/min N_2 flow. The reactor operates at temperatures up to 1000 °C, 600 °C in the experiments discussed here. The products pass through six impingers, with three of them filled with 5 ml methanol each, to collect the liquid products. A cooling jacket is used at the bottom of the inlet tubing of the reactor, to prevent thermal pyrolysis at lower temperatures (or temperature gradients) before entering the spouting zone. As shown by Ferdous et al.,[112] Nowakowski et al.,[32] and Sharma et al.,[113] lignin can melt at lower temperatures before entering the hot reactor zone, which makes it very difficult to study the effect of lignin on the pyrolysis of lignocellulosic biomass, as most of the lignin is never fed to the reactor. This is addressed in the current setup with the aforementioned cooling jacket, keeping the feeding pipe under 100 °C, and the high gas velocities in the feeding pipe, which prohibit early decomposition of biomass components.

5.2.2. Feedstock and catalyst

In order to study the mechanism of biomass pyrolysis, various biomass feedstocks and model compounds are being used. Among them, pine sawdust is widely used in bio-fuel production studies.[17,54,55] Cellulose and glucose are popular biomass model compounds. Cellulose is the major component in cellulosic biomass (typically, 23–32% in lignocellulose); therefore, the study of cellulose pyrolysis has been considered to be critical for the study of biomass pyrolysis mechanisms.[27,114,115] Glucose, the monomer of cellulose, is often used as a model compound for

cellulose to simplify simulations.[35] Recently, Mettler et al.[116] studied the fast thermal pyrolysis of glucose, cellodextrins and cellulose in a thin-film pyrolysis reactor at 500°C. They reported very different product distributions between glucose (with –OH groups instead of glycosidic linkages) and cellulose pyrolysis, showing the inappropriateness of using glucose as a model compound for cellulose. According to the above discussion, pine, cellulose and glucose were chosen as the feedstocks in this study. The grinded biomass and model compound powders were sieved to <350 μm in particle size.

In biomass catalytic pyrolysis, zeolite catalysts, including ZSM-5, Beta zeolite, Y zeolite, Mordenite and several mesoporous materials, have been widely studied.[28,31,56,57] In the majority of these studies, ZSM-5 has been proven to be very effective in catalytic (fast) pyrolysis due to its proper pore morphology. Jae et al.[56] investigated the shape selectivity of zeolite catalysts for glucose conversion in Catalytic fast pyrolysis in a pyroprobe reactor at 600 °C, using different zeolite catalysts. They showed that medium pore zeolites, such as ZSM-5 had the highest aromatic yield and minimum coke formation. Similarly, Carlson et al.[58] tested different zeolite catalysts for the conversion of glucose, xylitol, cellobiose and cellulose to aromatics using a pyroprobe reactor at 600 °C. They found that ZSM-5 had the highest aromatic yields and the lowest coke selectivity. Thus, in this study, a commercial ZSM-5 catalyst (synthesized by W.R. Grace & Co. in Al_2O_3/SiO_2 macroporous matrix of mean particle size of 70 μm) was used for the catalytic studies.

5.2.3.Experimental procedure

All experiments presented in this work thus far were performed with a biomass to catalyst weight ratio of 1. The relatively low ratio was chosen to maximize char/coke to catalyst ratios, and thus, exemplify the results. In the slow catalytic pyrolysis experiments, biomass and catalyst were well mixed before the experiment. Then, the mixture was pyrolyzed in a N_2 environment. Before starting the experiment, N_2 flow (20 ml/min) was kept for 1 hr to purge the air inside the reactor.

The feedstock was first dried at 120 °C for 30 min and then the temperature was ramped to 600 °C at a rate of 10 K/min. In fast pyrolysis, 1-2 gr of biomass was dried at 120°C overnight in a separate furnace. The desired reactor temperature (600°C) was reached before feeding the catalyst and biomass. Catalyst was fed via entrainment from the bottom of the reactor with 4 L/min N_2 flow. When the catalyst bed temperature reached 600°C, biomass was fed from the bottom as well. With the high N_2 flow rate, biomass reaches the spouting zone within very short times (~0.1 ms) and contacts with the hot catalyst particles. After the reaction, char/coke samples were collected via entrainment with 19 L/min N_2 flow. Quartz beads (sieved <180 μm) were used for the fast thermal pyrolysis experiments, assuming zero catalytic activity.

5.2.4.Char/coke characterization

Char/coke samples were observed using a FEI Quanta FEG 250 scanning electron microscopy (SEM) under high vacuum, to distinguish the differences in morphology of char samples produced in different experiments and visualize the coke/char deposition on the surface of catalyst pellets. Before each experiment, char samples were coated with gold to inhibit charging when the magnification is high. The FIB in-situ sample preparation and EDX element mapping was performed in a FEI Strata 400 STEM Dual Beam system, a fully digital Field Emission Scanning Electron Microscope (FE-SEM) equipped with Focused Ion Beam (FIB) technology and Flip stage/STEM assembly. A brief description of the sample preparation is illustrated in Figure 5-1. A catalyst particle was selected and milled on both sides, leaving a thin layer along the equatorial plane of the particle. The thin catalyst layer was lifted out with an Omniprobe micro-manipulator and imaged under scanning transmission electron microscopy (STEM).

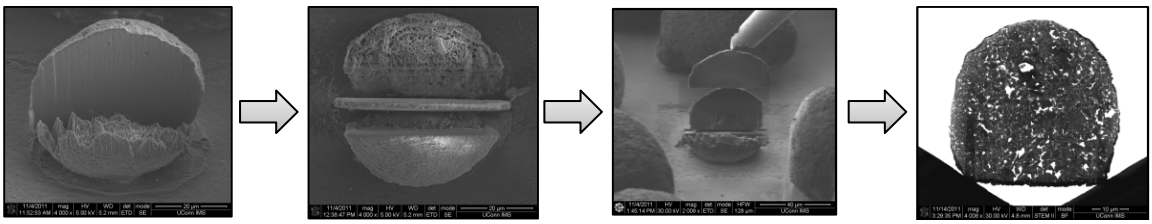

Particle milled on "first side." Cross sectioned on equator

Particle milled on "second side." (View from above)

Coupon "lifted out" using Omniprobe micro manipulator

Coupon imaged in STEM

Figure 5-1: Process of sample preparation in Focused ion beam (FIB)/Energy Dispersive X-Ray Spectroscopy (EDX) analysis.

Comparison of thermal properties of char samples was performed in a Q-500 thermogravimetric analyzer from TA Instruments. Platinum crucibles instead of alumina crucibles were used for the oxidation of chars, to prevent catalyst sintering with the crucibles. The samples were first dried at 120°C for 30 min and heated up to 900°C in air flow of 60 ml/min. Miura and Silveston[117] studied non-catalytic gas-solid reactions using the temperature-programmed reaction (TPR) technique. They showed a relative unreliability of rate parameters obtained based on TPR at only one heating rate. Therefore, in this study three different heating rates (5/10/15 K/min) were used in order to get accurate results in TPR data processing. All the TGA results presented in this paper were normalized to char weight loss (catalyst weight excluded) to compare thermal with catalytic residues. The surface area and pore size distribution of char/coke were determined in a Micrometitics ASAP 2020 Accelerated Surface Area and Porosimetry System. The isotherms of N_2 at 77 K were obtained from physisorption. Before analysis, all the char samples were degassed at 250°C under vacuum for 12 hr to remove the surface contaminants. The pore size distribution of the char samples was determined from the N_2 adsorption isotherms at 77 K, using the Barrett-Joyner-Halenda (BJH) method. FTIR measurements to characterize the functional groups of the char/coke were performed in a Nicolet MAGNA-IR 560 spectrometer with a DTGS detector. The FTIR was operated at 4 cm^{-1} resolution and 132 scans. Raman spectra were obtained in a

Renishaw 2000 Spectrometer Ramanscope, using a 514 nm laser as excitation source. 1-25% power and 16-32 exposure times were played around in order to avoid the detector saturation. 40% laser focus was used in order to prevent the local damage of the samples. Three different positions were analysed for each sample to verify the spectra.

5.3. Results and discussion

5.3.1. Char and coke yields

Figure 5-2 presents the experimental results for the yields of char/coke from pyrolysis of glucose, cellulose and pine. The effect of heating rates and catalyst are investigated in this study, although other factors, such as temperature, also play an important role.[26,110,111]

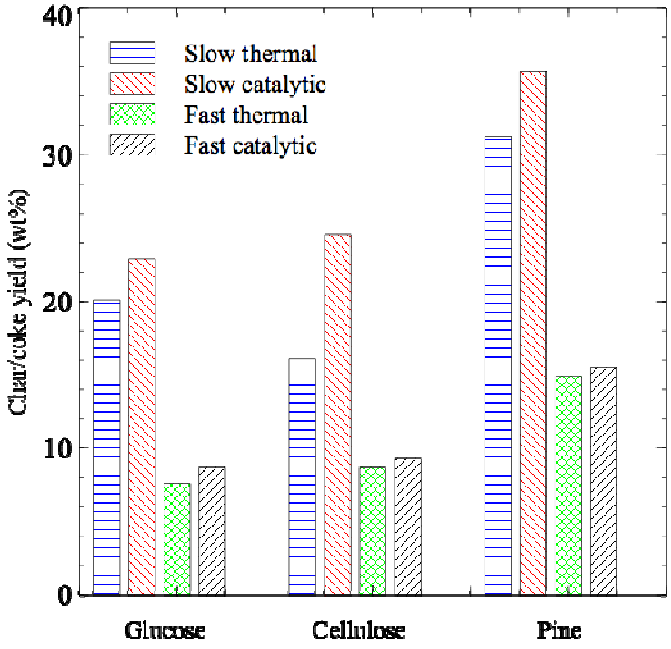

Figure 5-2: Comparison of char/coke yields between slow and fast, thermal and catalytic pyrolysis

The char/coke yields are significantly decreasing when fast heating rates are applied to the pyrolysis compared with slow heating rates. The lower char/coke yields from fast heating rates can be explained by the enhancement of the bond-scission reactions of the biomass to form tar

fragments, which, to some extent, limits the secondary pyrolysis (polymerization) of the volatiles.[118] Moreover, char/coke yields vary significantly between different feedstocks. To be specific, in slow thermal pyrolysis, pine produces the highest yield of char/coke; whereas cellulose produces less char/coke than glucose. Similar results were also obtained by other researchers.[119,120] In slow catalytic pyrolysis, fast thermal pyrolysis and Catalytic fast pyrolysis, char/coke yield from pyrolysis of pine outweighs that from cellulose, while glucose produces the lowest yield of char/coke. Furthermore, in order to study the catalyst effect, char/coke yields between thermal pyrolysis and catalytic pyrolysis are compared. For all the pyrolysis conditions performed in this study, catalytic pyrolysis produces more carbonaceous residues than the corresponding thermal pyrolysis due to the presence of catalyst. However, the reason for the increase of carbonaceous solid residues is not certain at this point. In other words, the solid residues can be char (a non-catalytic product), catalytic coke, or both. In the following, experimental results are analyzed, focusing on the formation of char and coke.

5.3.2.Char/coke morphologies

In Figure 5-3 the surface morphological characteristics of pure biomass feedstocks (a-c) and corresponding chars with or without catalyst, collected after slow thermal, (d-f), slow catalytic, (g-i), fast thermal, (j-l), and fast catalytic, (m-o), pyrolysis of the three types of biomass are investigated using SEM. The morphology of char derived from the slow thermal pyrolysis of glucose, (d), cellulose, (e), and pine, (f), retains a similarity to the original structure of the feedstock (a-c). In the case of slow catalytic pyrolysis, the glucose char, (g), is surrounding the catalyst particles forming catalyst agglomerates due to low temperature primary pyrolysis and melting. The slow catalytic cellulose char, (h), has a spiral type structure similar to the respective char produced from slow thermal pyrolysis, and appears to be formed as a separate phase to the catalyst particles. Pine slow catalytic char, (i), consist of irregular, large particles with slit-shaped surfaces surrounding the catalyst particles. In fast thermal pyrolysis, the morphologies of chars

from glucose, (j), cellulose, (k), and pine, (l), retain the original structure to some extent, but in a different way to the slow thermal pyrolysis, due to the different heating rates. A significant difference in morphology can be seen in pine fast thermal char, (l), compared with the slow thermal pyrolysis.

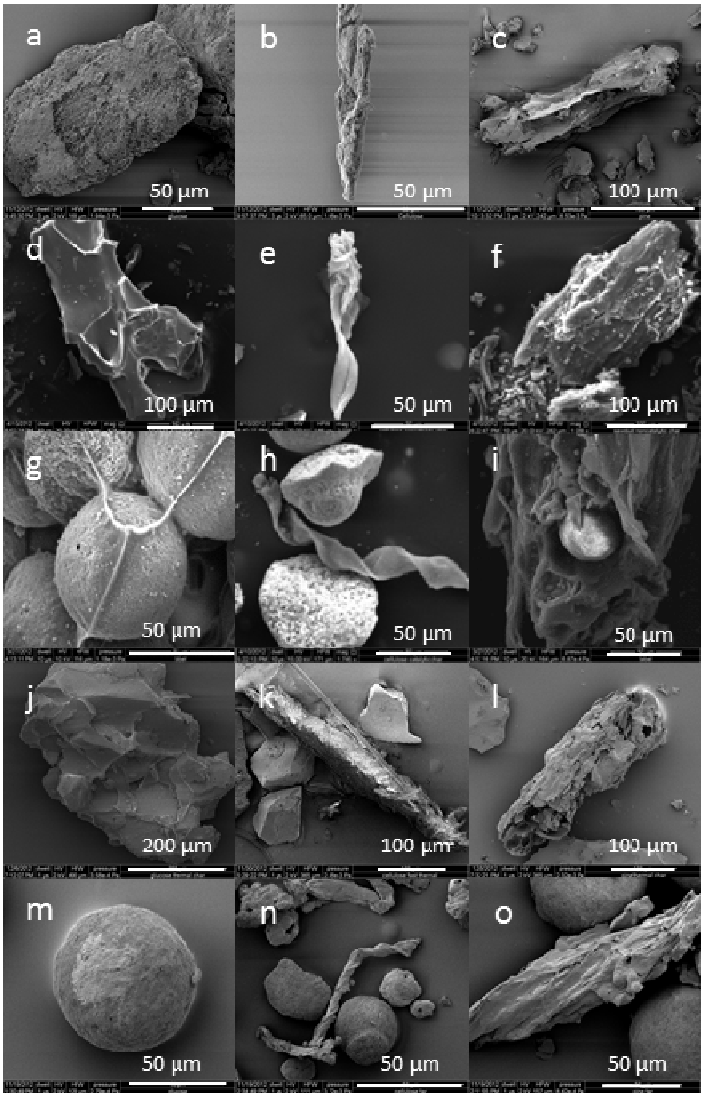

Figure 5-3: SEM morphology of biomass feedstocks: (a) glucose, (b) cellulose, (c) pine; and chars obtained by: (d) glucose slow thermal, (e) cellulose slow thermal, (f) pine slow thermal, (g) glucose slow catalytic, (h) cellulose slow catalytic, (i) pine slow catalytic, (j) glucose fast thermal, (k) cellulose fast thermal, (l) pine fast thermal, (m) glucose fast catalytic, (n) cellulose fast catalytic, (o) pine Catalytic fast pyrolysis.

The fast volatile release during fast pyrolysis enlarges the internal cavities, resulting in a more open structure. Therefore, the macroporosity of chars increases with increasing heating rate.[26] In Catalytic fast pyrolysis, there is no catalyst agglomeration occurring in the glucose case, (m), reflecting the benefit of fast heating rates to prevent excessive char formation. In the case of Catalytic fast pyrolysis of cellulose, (n), and pine, (o), char generally does not retain the structure of the original feedstock indicating that repolymerization may be the dominant mechanism for its formation.[105] However, it should be noted that in all the pyrolysis experiments, the formation of coke is considered to occur inside the catalyst pores due to catalytically enhanced reactions of small molecule products and intermediates in the secondary pyrolysis of volatile matters.[105] Thus, the formation of coke cannot be visualized with SEM.

5.3.3. Char/coke deposition on the outer surface and the equatorial plane of the catalyst

Figure 5-4 is the EDX elemental mapping of coked catalysts from pyrolysis of different biomass feedstocks. Clear char "footprints" can be seen in the slow catalytic pyrolysis of glucose and sawdust. The catalyst coupon from slow catalytic pyrolysis of glucose has a clear char edge, which is consistent with SEM pictures. It also has a large amount of char inside the pellet, which must be the result of melting inside catalyst macropores at intermediate temperatures. The coupon from slow catalytic pyrolysis of pine also has a char edge, but it is much thinner than that of glucose. Inside the catalyst pellet, less carbon is observed. The catalyst after slow catalytic pyrolysis of cellulose has almost no edges and only some small red spots can be seen, which indicates the formation of carbon inside the zeolite. In all the Catalytic fast pyrolysis cases, the catalyst has char deposition both on the outer surface of the catalyst and inside the catalyst. Specifically, in Catalytic fast pyrolysis of glucose, there exists a thinner and more homogeneous carbon layer on the surface of the catalyst pellet compared with slow catalytic pyrolysis of glucose, which verifies the improvement in catalyst accessibility, concluded in the SEM analysis. Overall, the carbon mapping of the coked catalyst shows a significant difference of carbon

deposition between slow catalytic pyrolysis of glucose/sawdust and cellulose. The deposition of char on the outer surface of the catalyst might affect the accessibility of the catalyst at the beginning of the pyrolysis. Thus, it can prevent volatile matters from accessing the zeolite and prohibit secondary pyrolysis, where coke is produced.

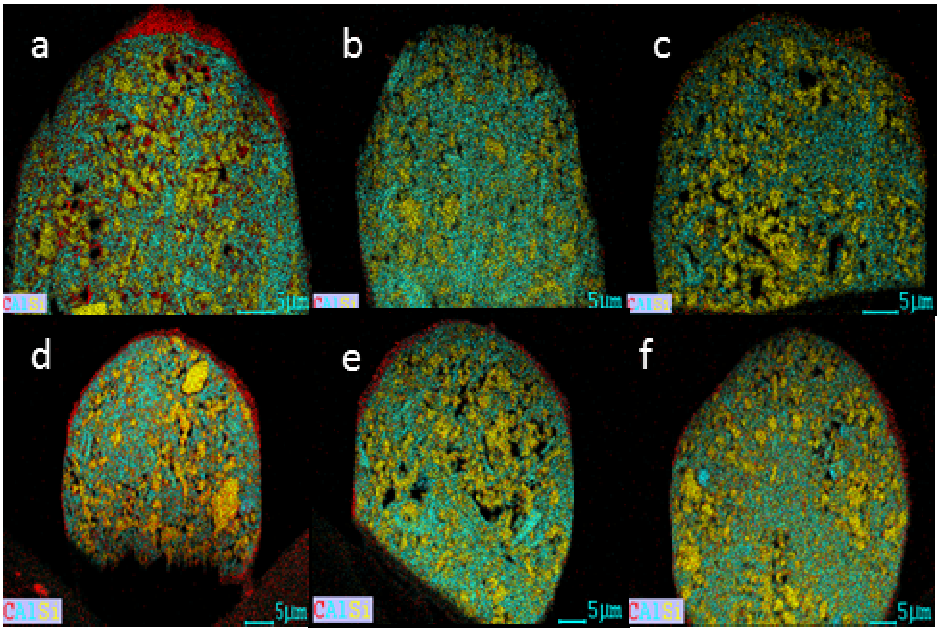

Figure 5-4: FIB images of the equatorial plane of the catalyst particle after slow and Catalytic fast pyrolysis. (a) glucose slow catalytic, (b) cellulose slow catalytic, (c) pine slow catalytic, (d) glucose fast catalytic, (e) cellulose fast catalytic, (f) pine fast catalytic. (Green=Al, Yellow=Si, Red=Carbon)

5.3.4. Comparison of surface areas and pore size distributions

Figure 5-5 shows the isotherms of N_2 adsorption and corresponding pore size distribution plots for pure ZSM-5 catalyst and the solid residuals obtained after slow and Catalytic fast pyrolysis. The isotherm profile of the catalyst after glucose slow catalytic pyrolysis exhibits very characteristic profiles. Microporosity (<2 nm) increases, which can be attributed to the porosity of char formed, also evident in the desorption profiles that indicate ink bottle shaped pores. Moreover, the catalyst macropores are significantly diminished, while the hysteresis loop during N_2 desorption reflects the creation of a mesoporous network in the form of ink bottle type pores

(H2 in IUPAC classification), as shown in the isotherm and pore size distribution plots. In the isotherm of the solid residue after cellulose slow catalytic pyrolysis, the decrease of the micropore volume reflects the enhanced coke formation and micropore blocking due to coking. In the isotherm of the solid residue after pine slow catalytic pyrolysis, the micropore volume increases slightly, but the macropore volume does not have a significant change (shown also in the pore size distribution plot). In Catalytic fast pyrolysis, however, a clear loss of microporosity is observed in the isotherms for all the cases, which can be attributed to the formation of coke inside the zeolite micropores.

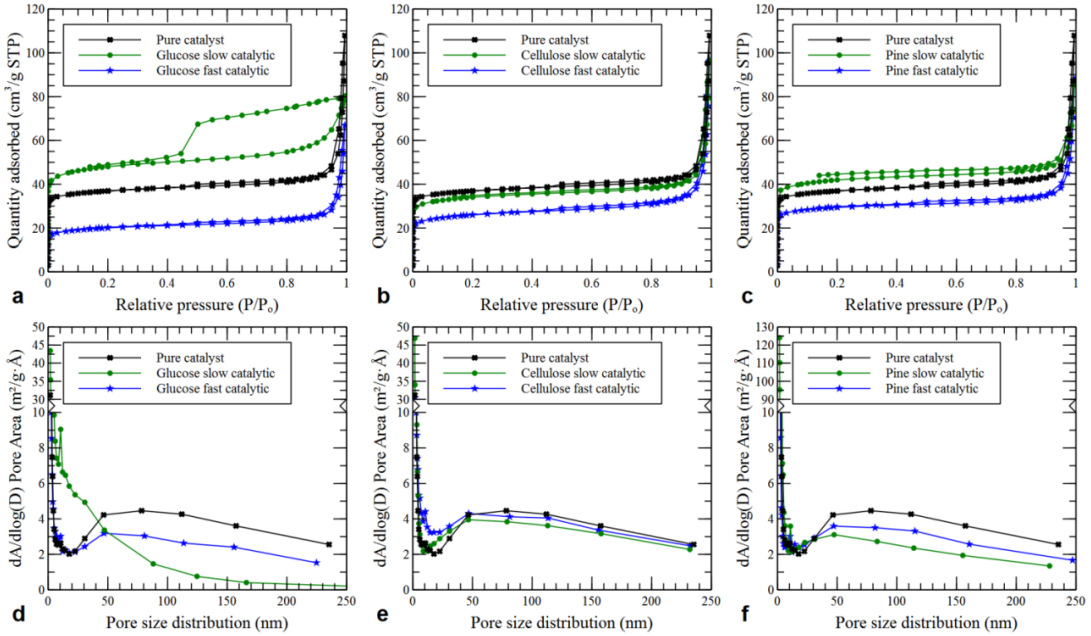

Figure 5-5: N_2 adsorption/desorption isotherms measured at −196°C and the pore size distributions of pure catalyst and deactivated catalyst produced from (a,d) glucose, (b,e) cellulose, (c,f) pine, calculated from adsorption isotherms by using the BJH method.

Table 5-1 shows a summary of the micropore area and total surface area of the catalyst and the catalytic chars (catalyst included). The micropore area of glucose and pine slow catalytic chars increased by 24% and 11% respectively, compared to pure catalyst. The microporosity of cellulose slow catalytic chars decreased by 13%, a smaller amount compared with the

microporosity of all the fast catalytic chars, which decreased by 52% (glucose), 38% (cellulose), and 22% (pine). The glucose slow catalytic char has the highest total surface area due to the highest microporosity, whereas the glucose fast catalytic char has the lowest total surface area due to the lowest microporosity.

Table 5-1: Micropore and total surface area of the fresh ZSM-5 catalyst and coked catalyst/char mixtures after catalytic pyrolysis (m^2/g)

	Micropore area (<2nm)	Total surface area
Pure catalyst	98.98	124.3
Glucose slow catalytic	122.4	162.1
Glucose fast catalytic	47.55	68.33
Cellulose slow catalytic	86.30	115.0
Cellulose fast catalytic	60.93	90.05
Pine slow catalytic	109.7	141.5
Pine fast catalytic	76.94	99.50

This result reveals that the catalyst porosity change is most significant in the pyrolysis of glucose when high heating rate is introduced in the experiment. Combining the results from SEM, FIB-STEM, BET and TPO (discussed in the next section), the significant reduction of macropores in the case of glucose and pine slow catalytic char might be attributed to macropore blocking by char formation on the catalyst outer surface. Macropore blockage is the reason for the minor catalyst effect on the properties of char and coke (e.g. oxygen content) in slow catalytic pyrolysis. Furthermore, the decrease of the number of micropores after cellulose slow catalytic pyrolysis is attributed to coking, showing catalytic activity, even at slow heating rates. The smaller quantity of char produced in this case is because of the catalytic enhancement of depolymerization of biomass to liquid and gas products.

5.3.5. Thermal gravimetric analysis of char/coke

In order to explore the effect of char/coke formation on the catalyst performance, temperature programmed oxidation (TPO) of the char/coke samples are performed in air using 3 different heating rates.[121] Before analyzing the char/coke samples, the catalyst effect on the oxidation itself was studied. TPOs of pure graphitic carbon and carbon/catalyst mixtures showed that there is no significant effect of the catalyst on the char/coke oxidation. Figure 5-6 presents differential weight loss profiles in TPO of the solid residues of thermal and catalytic (slow and fast) pyrolysis. TPO profiles are normalized to exclude the catalyst weight and the first derivative of weight loss (DTG) versus temperature is shown. In the comparison of slow thermal and slow catalytic char/coke from the three feedstocks, the char formed from pine thermal pyrolysis exhibits a DTG maximum identical to that of cellulose, whereas it also gives two additional DTG peaks. The three DTG peaks of pine thermal pyrolysis char reflect char structures of different origins, corresponding to its hemicellulose, cellulose and lignin compounds.[122] Interestingly, the addition of catalyst in slow pyrolysis conditions has only minor effect on the oxidation profiles of the solid residues from glucose and pine. In the case of glucose, the DTG peak is shifted slightly to the left, indicating a slight catalytic activity affecting the polymerization reactions, responsible for glucose char/coke formation. Cellulose pyrolysis exhibits a rather different behavior. The DTG peak moves to the right, indicating a more significant catalytic activity towards solid residues of lower oxygen content. This indicates a formation of an oxygen poorer phase that can be attributed to coke formation. Moreover, the oxidation peak of the glucose (catalytic and thermal) char/coke sample is more symmetrical than that of cellulose. In the latter case the high temperature side of the DTG profile displays a faster decrease in reaction rate, which can be attributed to a lower reaction order for the cellulose char/coke oxidation.[123]

TPOs of Catalytic fast pyrolysis samples show a broad DTG peak for glucose and multiple DTG peaks for the cellulose and pine solid residues. The broad DTG peak in the case of glucose can be

deconvoluted into multiple peaks that represent different oxidation steps, consistent with cellulose and pine. Generally, the first char/coke oxidation peak at 400-450 °C corresponds to char formation due to thermal reactions. The second DTG peak at 550-600 °C corresponds to catalytic coke formation. The wider shape of the DTG curves in the case of Catalytic fast pyrolysis char/coke indicates a lower char/coke apparent oxidation reaction rate or a multiplicity of compounds, being oxidized at different rates. Compared with Catalytic fast pyrolysis, fast thermal pyrolysis produces higher oxygen content char, leading to a lower temperature peak in the case of glucose and pine. Moreover, there is no secondary DTG peak at higher temperature in the fast thermal pyrolysis, reflecting the infeasibility of coke formation due to non-catalytic reactions. It is clearly evident that the catalytic effect is much stronger in fast pyrolysis experiments for each biomass feedstock compared with that in slow pyrolysis experiments.

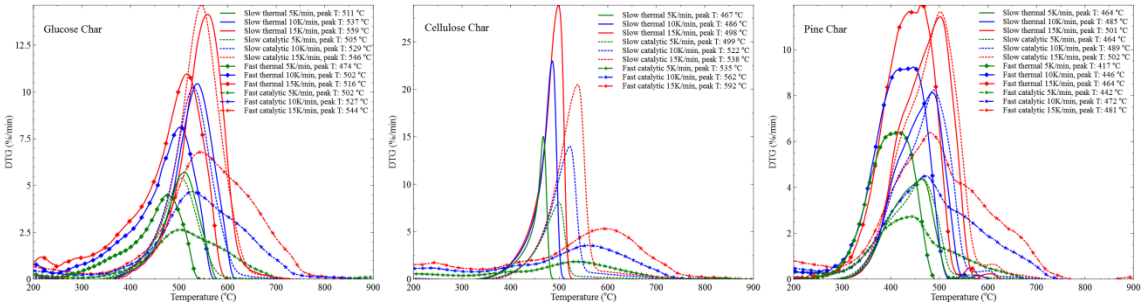

Figure 5-6: Oxidation of slow thermal (solid line) slow catalytic (dotted line), fast thermal (solid disc) and fast catalytic (dotted disc) pyrolysis char/coke from (a) glucose, (b) cellulose and (c) pine in TGA in three heating rates (5K/min (green), 10K/min (blue), 15K/min (red)).

In summary, many hypotheses derived from SEM, STEM and BET were verified with TPO results. Cellulose exhibits an entirely different behaviour, showing smaller catalyst surface coverage at slow pyrolysis conditions. TPO confirms this observation, showing a clear contribution of the catalyst to the oxidation temperature of cellulose slow catalytic char. The catalyst/char samples after Catalytic fast pyrolysis of all the feedstocks show smaller amounts of char and intermediate surface coverage of the catalyst, indicating a catalytic mechanism for coke

formation on the catalyst surface.

5.3.6.FTIR and Raman analysis of char and coke

The char/coke chemical composition with respect to their bonding groups was studied in FTIR. Figure 5-7 shows the spectrum 1500-1800 cm^{-1} of the glucose char/coke, produced at different heating rates with and without catalyst. The C=C stretch (1620-1680 cm^{-1}) appears in the char/coke produced from all the pyrolysis experiments. Interestingly, the char/coke after Catalytic fast pyrolysis contains minor amounts of carbonyl (C=O) groups, which reflects the efficiency of oxygen removal in Catalytic fast pyrolysis and the dominance of a different mechanism producing the catalytic coke. Consistent with the TPO results, the fast heating rates of the spouted bed reactor enhance the catalytic effect in pyrolysis, thus favouring catalytic coke formation. The diminished C=O in Catalytic fast pyrolysis compared to that in slow catalytic pyrolysis reveals that C=O is contained mostly in char instead of coke. The spectrum at 2500-3600 cm^{-1} (not shown here), exhibits a similar broad peak for all the chars studied, showing that O-H bonds (free hydroxyl bonded, hydrogen bonded and in carboxyl group) exist consistently. The FTIR analysis shows that coke and char are not graphitic carbon, and should not be treated as such in the modelling of pyrolysis mechanisms.[124,125] Further verification of this observation was performed in TPO experiments with mixtures of graphitic carbon and coked catalysts (not shown here), in which the TPO shows one clear DTG peak for the carbon (at ~800°C), well-separated from those of char and coke.

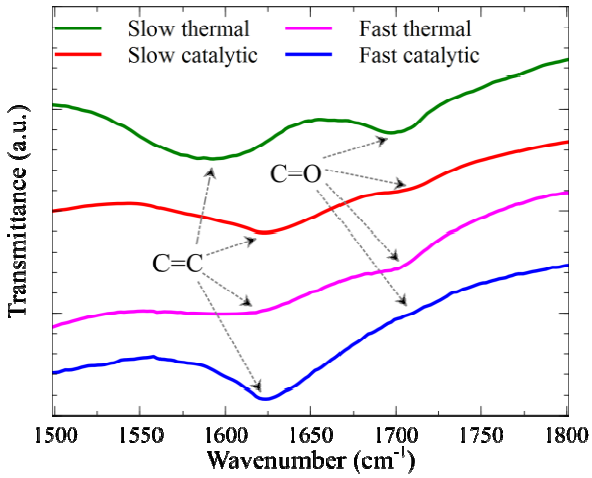

Figure 5-7: FTIR spectra of glucose chars from slow thermal pyrolysis, slow catalytic pyrolysis, fast thermal pyrolysis and Catalytic fast pyrolysis

In-depth study of the char/coke composition was also performed in Raman. Figure 5-8 shows the Raman spectra of the char/coke from glucose pyrolysis. The deconvolution of the spectra is based on observation of the main peaks, shoulders, valleys, and tails. Thus for the slow pyrolysis, the spectra has been deconvoluted into 6 Gaussian peaks: #1, *ca.* 1700 cm^{-1} (D_2 band, corresponding to carbonyl groups); #2, *ca.* 1600 cm^{-1} (G band, corresponding to well-structured aromatic rings); #3, 1550-1570 cm^{-1} (G□ band, corresponding to coexistence of a well-structured and a not well-structured carbons); #4, *ca.* 1450 cm^{-1} (D_3 band, corresponding to structural defects of aromatic clusters); #5, 1360-1370 cm^{-1} (D band, corresponding to not well-structured aromatics); and #6, *ca.* 1270 cm^{-1} (corresponding to C-H vibrations). For the fast pyrolysis, 5 peaks were sufficient for fitting the spectra: #1 (D_2 band); #2 (G band); #3 (G□ band); #4 (D band); and #5 (C-H vibrations). Detailed description of the interpretation of each band identified by Raman can be found elsewhere.[39,126,127] Comparison of the Raman spectra of the slow and fast pyrolysis shows that the second broad peaks (D_3+D+C-H in slow pyrolysis; D+C-H in fast pyrolysis) decrease significantly when fast heating rates are applied in pyrolysis. The Catalytic fast pyrolysis char/coke has the lowest second peak (0.21 in area fraction) among the four. It appears that the

formation of defect aromatics (mainly D band and D_3 band) is not favoured by the fast heating rates. Combining the results from TPO and Raman implies that the second peak is characteristic of the char formed. This is in agreement with Sheng,[127] who claimed that as the defect bands increase, the ordering of the char decreases and the char becomes more reactive. Moreover, the sum of areas of the G and G□ bands increases for the fast pyrolysis chars and is highest for the Catalytic fast pyrolysis char/coke. The fraction of the areas of the G and G□ bands exhibit similar trends to those observed from TPO, indicating an increase in catalytic coke. Furthermore, the total peak area of the defect band changes only slightly between slow thermal and slow catalytic pyrolysis, compared with that between fast thermal and Catalytic fast pyrolysis, which is very consistent to the TPO results (lack of significant catalytic activity at slow pyrolysis conditions). It is not reasonable to define coke as the well-structured aromatics and char as defect aromatics, since G and D bands coexist in all the Raman spectra, but the changes of their area fractions are indicative of the same observations in TPO, STEM/FIB and FTIR.

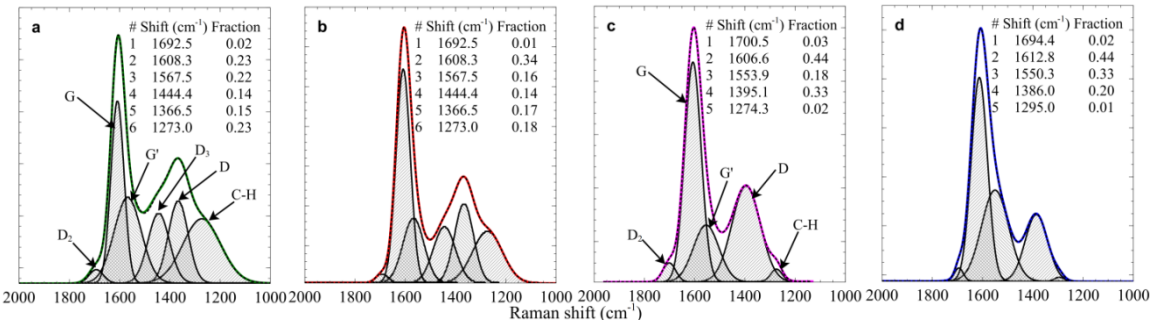

Figure 5-8: Raman spectra of glucose char from (a) slow thermal, (b) slow catalytic, (c) fast thermal and (d) Catalytic fast pyrolysis. The calculated area fractions of deconvoluted peaks (#1-6 for slow pyrolysis, #1-5 for fast pyrolysis) in each case are shown.

5.3.7. Char and coke fraction in the solid residue

The TPO results of Figure 5-6 were further analyzed using model-based and statistical deconvolution methods. For this illustration the TPO experiments of the glucose char/coke. In principle, glucose is an ideal candidate for a model-based analysis of its coke TPO, since there

exists mainly one mechanism (i.e., polymerization) for its formation.[105] The random pore model (RPM) by Bhatia and Perlmutter[128] was utilized for this analysis. This model considers the overlapping of pore surfaces and the competing effects of pore growth during gasification, and the destruction of the pores due to the coalescence of neighboring pores by oxidation. The RPM models solid conversion, X, according to:

$$\frac{dX}{dt} = k_{RPM}(1-X)\sqrt{(1-\psi \ln(1-X)}, \qquad (1)$$

where k_{RPM} is the reaction rate constant and ψ a pore structure factor of the unreacted sample:

$$k_{RPM} = k_0 e^{-\frac{E}{RT}}, \qquad (2)$$

$$\psi = \frac{4\pi L_0(1-\varepsilon_0)}{S_0^2}, \qquad (3)$$

with S_0, L_0 and ε_0 the pore surface area, pore length, and solid porosity, respectively.

As shown in Figure 5-9, the RPM is capable of representing the TPO of chars from glucose slow pyrolysis. In agreement with the previous discussion about the lack of catalytic contribution in glucose slow pyrolysis, the RPM is capable of modelling the DTG profile of the glucose slow catalytic char with the parameters of the thermal pyrolysis fit, by only adjusting the RPM shape factor (Fig.5-9(c)). This clearly indicates that the only contribution of the catalyst at slow pyrolysis conditions is on the shape, surface area and pore length of the char formed, but not on its chemical composition.

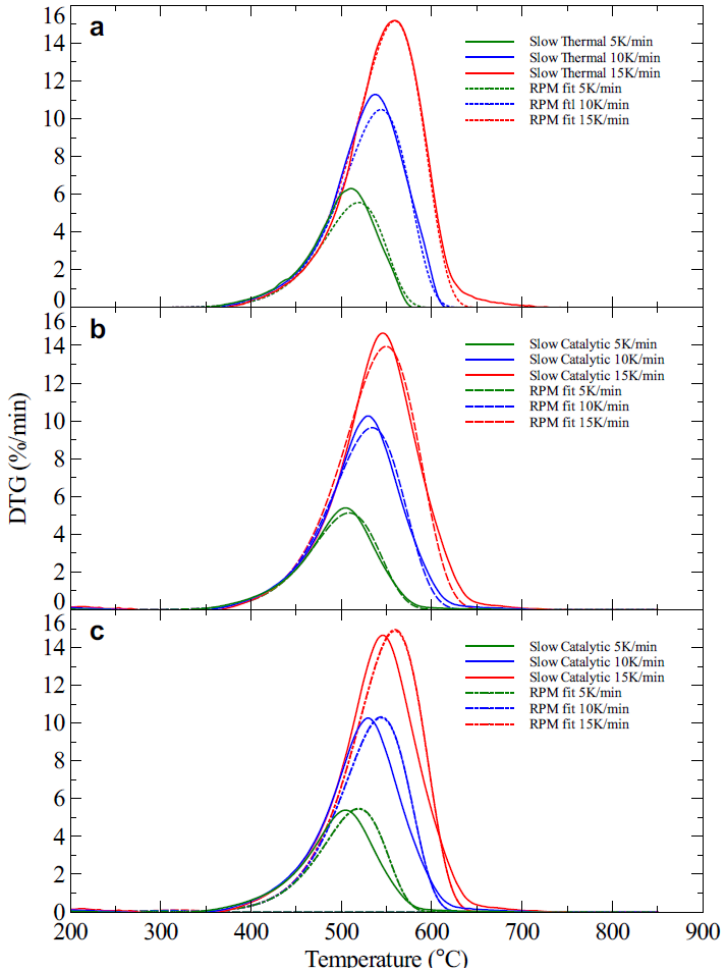

Figure 5-9: Application of the RPM on the TPO of chars from: (a) glucose slow thermal pyrolysis; (b) glucose slow catalytic pyrolysis; and (c) glucose slow catalytic pyrolysis using the RPM parameters of (a).

Figure 5-10 presents the RPM fit of the glucose chars from fast pyrolysis. The quality of fit is again very good for the thermal pyrolysis char, whereas the catalytic pyrolysis char exhibits two convoluted DTG peaks that cannot be represented by the RPM (Figure 5-10(b)). Figure 5-10(c) presents the result of the RPM when including the contribution of the fast thermal char, adjusting only the RPM shape factor, to account for the effect of the catalyst on shape and surface area differences. The inclusion of the RPM of the fast thermal char of glucose is capable of deconvoluting the fast catalytic DTG, identifying two solid residues of different origins. Therefore, it is reasonable to assume that, in parallel to the thermal polymerization reactions

(char), there is a significant contribution from catalytically enhanced reactions yielding solid residues of different composition (coke). This is an interesting finding, because it indicates that we can deconvolute experimentally the extent to which the catalyst contributes to catalytic pyrolysis reactions. The RPM predicts that 30wt% of the solid residue after Catalytic fast pyrolysis of glucose is fast thermal char.

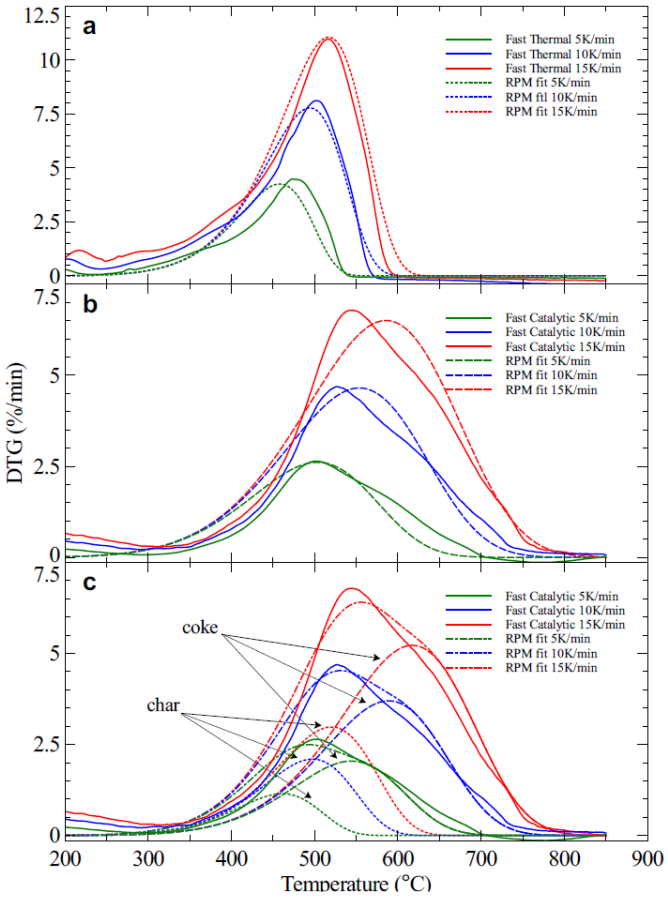

Figure 5-10: Application of the RPM on the TPO of chars from: (a) glucose fast thermal pyrolysis; (b) glucose Catalytic fast pyrolysis; and (c) glucose Catalytic fast pyrolysis using the combined RPM models of (a) and (b).

Table 5-2 summarizes the parameters of the best fit of the RPM for the char/coke obtained from glucose pyrolysis. The small ψ factors estimated should be attributed to the high surface area of glucose chars and the presumably small pore length (indicated by the EDX elemental mapping of Figure 5-4).

Table 5-2: Kinetic parameters of the RPM for the glucose char samples during TPO at three heating rates (5, 10 and 15 K min^{-1})

	k_0 (s^{-1})	E (J mol^{-1})	ψ	R^2
Glucose slow thermal	1.870E+6	1.361E+5	0.268	9.918E-1
Glucose slow catalytic ***char fraction=0***[a]	8.302E+5	1.292E+5	0	9.935E-1
Glucose slow catalytic ***char fraction=1***[b]	1.870E+6	1.361E+5	0.193	9.621E-1
Glucose fast thermal	3.665E+2	0.768E+5	0.898	9.956E-1
Glucose fast catalytic ***char fraction=0***[c]	8.066	5.932E+5	0	9.500E-1
Glucose fast catalytic ***char fraction=0.3***[d]	6.525E+1	0.755E+5	0	9.968E-1

[a]Assumes a dominant contribution of catalytic reactions; [b]Assumes a negligible contribution of catalytic reactions; [c]Assumes only one DTG peak; [d]Includes the DTG contribution of the thermal char.

5.3.8. Char fractions from different origins in the biomass

It should be noted that application of the RPM is superior to statistical deconvolution methods, as kinetic constants are extracted and the deconvolution is performed with the same constants for different TPO heating rates. This is valid for as long as the fits are of statistical significance, which is the case when fitting a small number of DTG peaks (small number of solid components being oxidized). However, chars from thermal pyrolysis of pine show four inflection points in their DTG curves, with additional peaks measurable after catalytic pyrolysis, due to the formation of catalytic coke. Therefore, a more conventional statistical deconvolution approach was employed; using iterative least-square fits of Exponentially Modified Gaussian (EMG) distribution function to the pine DTG signals.

Application of EMG is very common in deconvolution of chromatographic peaks[129] and was selected for this analysis due to its ability to represent fronted (or tailed) distributions. Fronted

distributions are evident in all the TPOs of Figure 5-4, particularly in the TPO of cellulose. Figure 5-11 shows the results of the deconvolution for the slow and fast pyrolysis chars from pine. For each case, the four deconvoluted peaks represent different chars from the three main components in pine (hemicellulose, cellulose and lignin), which means that these precursors participate in different reactions (or same type of reactions, but with different precursors). The last small peak at T>500 °C is attributed to the oxidation of extractives and other heterogeneous components of pine and should be considered part of the lignin char. These high temperature peaks were evident in TPO of the original pine (not shown here); therefore, they are not a pyrolysis product. By comparing the deconvolution results with those from TPO of pine and cellulose, it is reasonable to assume that peaks #1, #2, #3 represent chars from hemicellulose, lignin and cellulose, respectively; which is consistent with the location of peaks of the three components in the deconvolution of pyrolysis of pine.[130] In slow pyrolysis of pine, the ratio of hemicellulose (peak #1) and cellulose (peak #3) chars is ~2, which does not agree well with the initial pine composition (hemicellulose: 23-32%; cellulose: 38-50%; lignin: 15-25%). Moreover, in fast pyrolysis of pine, the fraction of char from hemicellulose increased significantly, whereas the fraction of char from cellulose decreased, which reflects that fast heating rates favour the formation of hemicellulose char. The ratio of cellulose to lignin char is about 6/10 in all cases, which is in good agreement with their initial fractions (~40wt% and ~20wt%, respectively) times their char yield (~15wt% and ~50wt%,[131] respectively). Figure 5-11 shows that in the research of catalytic options for the minimization of char formation in biomass pyrolysis, we need to focus on the reaction pathways of cellulose, since it appears to be the least affected by the fast heating rates. The char fractions of lignin and hemicellulose (peaks #2 and #3, respectively) are decreasing with increasing pyrolysis heating rates.

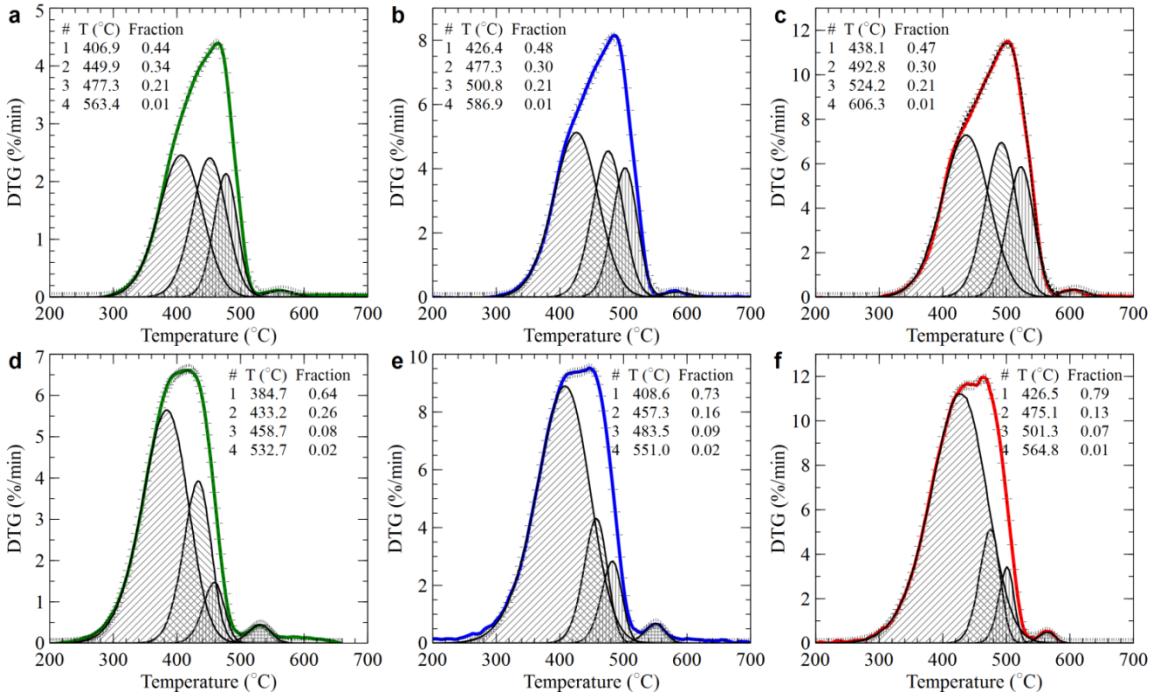

Figure 5-11: Exponentially Modified Gaussian peak deconvolution of chars obtained from: (a-c) pine slow thermal pyrolysis, 5/10/15 K min^{-1}; and (d-f) pine fast thermal pyrolysis, 5/10/15 K min^{-1}.

5.3.9. Reaction pathways for coke and char formation

Brewer et al.[38] performed ^{13}C-NMR analysis on the chars obtained from fast and slow thermal pyrolysis of switchgrass, showing that aromatic clusters of 7-8 rings terminated by carbonyl and hydroxyl groups are the representative composition of thermal char (a structure similar to the one shown in Figure 5-12).

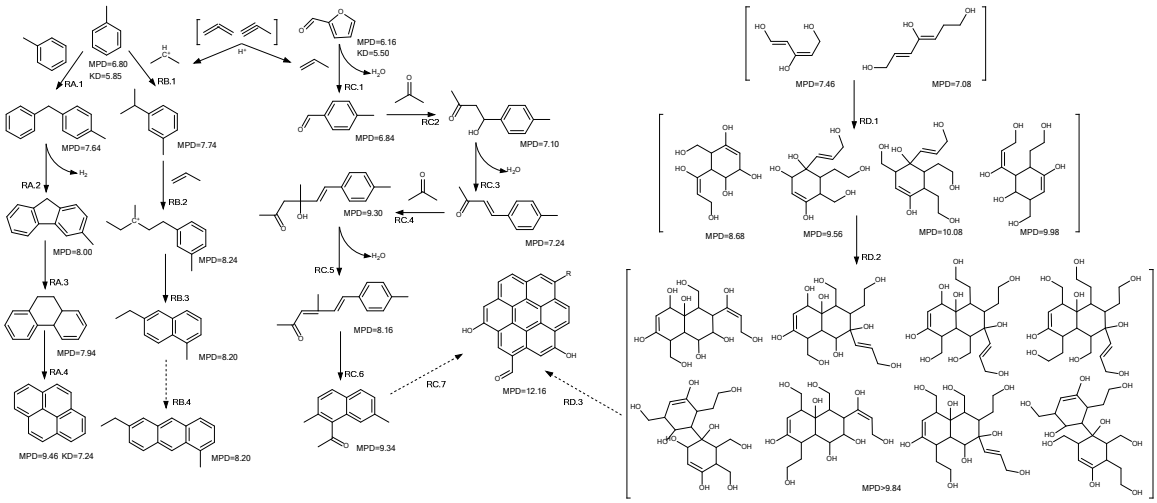

Figure 5-12: Possible reaction pathways for coke and char formation.

(a) RA[45] – toluene self-alkylation *via* RA.1 (alkylation), RA.2 (dehydrogenative coupling), RA.3 (isomerization), and RA.4 (hydrogen transfer and repetition of RA.1-RA.5); (b) RB[46] – coke formation *via* RB.1 (alkylation on the nucleus with carbenium ions), RB.2 (side alkylation and isomerization), RB.3 (cyclization), and RB.4 (repetition of RB.2, RB.3); (c) RC – char formation from furfural *via* RC.1 (Diels-Alder with propylene), and aldol condensations (RC.2-RC.7); RD – Diels Alder cycloadditions of C-5 and C-6 anhydrosugars *via* RD.1 (Diels Alder self- or hetero- cycloaddition), RD.2 (Diels Alder cycloaddition) of the products of RD.1 with the original anhydrosugars, and RD.3 (repetition of RD.2, followed by enol-keto tautomerization to produce carbonyl ending groups and condensation to fused polyaromatic rings terminated by carbonyl and hydroxyl groups). MPD is the minimum projection diameter of each molecule; KD is the kinetic diameter reported by Jae et al.[56]

Formation of char is typically observed in concert with CO and CO_2, which can be explained by the decarbonylation of furanics postulated by Huber and co-workers.[18,51] Another interesting observation was reported by Mettler et al.,[105] who compared the char yield from pyrolysis of glucose-based carbohydrates and the fraction of carbonyl groups present in the volatile products and observed a very strong relation. They postulated that aldol condensation chemistry is significant in thermal pyrolysis char formation. In parallel to the aforementioned studies, there is a wealth of information and published work on the nature and possible mechanisms of coke formation in the catalytic cracking of gasoil and other hydrocarbons.[40,45,46,132] Hydrogen transfer and carbenium ion chemistry is shown to be dominant in the mechanisms of catalytic coke formation, having small olefins and single ring aromatics as its origin. The production of

aromatics is established in catalytic pyrolysis of biomass, while small olefins are mostly postulated as responsible for their formation *via* the hydrocarbon pool mechanism proposed by Huber and coworkers.[59] Therefore, it is reasonable to assume that the mechanisms accepted in catalytic pyrolysis of hydrocarbons may well be relevant to the catalytic pyrolysis of biomass. In that view, there should be a competition between the reactions forming aromatics and the reactions responsible for catalytic coke, given the hydrogen-poor environment in the hydrocarbon pool and the small evidence of larger olefins observed in biomass catalytic pyrolysis experiments. On the other hand, char formation reactions can be surmised to proceed *via* reactions of oxygenates (aldol and Diels-Alder), but given the FTIR and Raman evidence they must lead to large polyaromatic rings terminated with carbonyl and hydroxyl groups. One other aspect to consider is the steric constraints of the ZSM-5 catalyst, which impose a requirement for the catalytic coke to be smaller (in its number of aromatic rings) than the char formed. The largest polyaromatic that can be accommodated and trapped inside the channel intersections of MFI zeolites is methylpyrene (shown with molecular modelling by Guisnet et al.[133]). The formation of polyaromatic rings is accepted to proceed *via* a series of alkylation and hydrogen transfer steps.[133] Marin and co-workers[46] show that coke formation proceeds *via* hydrogen transfer, alkylation and ring closing, with toluene and propylene as possible coke precursors. Cheng and Huber,[51] accept a mechanism that produces allene and/or methylacetylene (formed by decarbonylation of furanics), which undergo oligomerization to form a series of olefins and single ring aromatics. Accepting the thermodynamic stability of polyaromatics, it is straight-forward to envision that hydrogen transfer chemistry is relevant to coke formation in biomass catalytic pyrolysis.

On the basis of the aforementioned possible reaction pathways for the formation of coke and char in the catalytic pyrolysis of biomass, we suggest representative reaction schemes that are relevant to the pyrolysis of glucose and cellulose. Four reaction pathways (noted as RA, RB, RC, and RD) for coke and char formation are illustrated in Figure 5-12, together with the minimum projection

diameter (MPD) for each component calculated in ChemAxon Marvin.[134] Toluene and furfural are chosen as the starting molecules for showing the mechanisms, since their presence as biomass (glucose) pyrolysis products is confirmed in our liquid product analysis and the study by Carlson et al.[59] (1E,3E)-penta-1,3-diene-1,3,5-triol and (2E,4Z)-hepta-2,4-diene-1,4,7-triol are used as char precursors, as they are (according to the glucose/cellulose pyrolysis mechanism proposed by Vinu and Broadbelt[125]) among the postulated anhydrosugars responsible for carbon formation (char is tracked as carbon in that model). The reactions of Figure 5-12 are in no way exhaustive and can be considered only as representative of the mechanisms involved in coke and char formation. Moreover, there are alternative pathways that can co-exist (for instance, dehydration and tautomerization of the alcohols product in pathways RC and RD), which are omitted. The focus of this analysis is to explore the likely mechanisms that can produce fused or linear polyaromatic rings with or without oxygen containing ending groups.

Mechanisms RA and RB are similar to those proposed in Cerqueira et al.[45] and Quintana-Solórzano et al.,[46] respectively, and represent common coke formation reactions (with hydrocarbon precursors). According to Guisnet and Magnoux,[40] the composition of high temperature (400-600°C) coke is practically independent of the reactant and is considered to comprise polyaromatics, formed not only by condensation and rearrangement steps but also via various hydrogen transfer steps on acid catalysts. Methylpyrene is a major coke component with a molecular size intermediate between that of the MFI supercages and of its pore apertures. Therefore, the intermediate size aromatic rings derived via pathways RA and RB are sterically blocked inside the supercages of the ZSM-5, while they are thermodynamically resistant to cracking. Further alkylation and aromatization of the representative final polyaromatic of the RA mechanism is not feasible, as it is sterically constrained by the size of the ZSM-5 cavities. Floudas and co-workers[135] report a pore cavity size of 7.5Å for calcined ZSM-5,[136] which can tightly accommodate the pyrene molecule (~9Å diameter), given that the ZSM-5 cage and pyrene

are not spheres. Methyl- or ethyl- anthracene (the final product of pathway RB, ~8Å diameter) cannot escape the ZSM-5 pore (with pore limiting diameter of 4.5Å and maximum crystallographic diameter of ~6Å). Therefore, polyaromatics once formed inside the zeolite cage are bound to stay in it and undergo further aromatization leading to ring structures with a maximum of *ca.* 4 rings. Given their relatively larger residence time inside the zeolite (and the reactor) these polyaromatics might partially condense to heavier forms, leading to insoluble coke that is difficult to analyse. In summary, we postulate that the dominant coke formation mechanisms of catalytic cracking of hydrocarbons are relevant in biomass (glucose in this case) pyrolysis as well. The largest coke form possible should be defined by the ZSM-5 steric constraints, through a more in-depth analysis is required, such as the work by First at al.,[135] describing the interactions between the guest and host atoms that capture the particular shape of the molecule subject to its possible rotations. Molecular projection (MPD) and kinetic diameters (KD) are of little use in this regard.

Nonetheless, the coke from glucose pyrolysis is quantitatively much larger than what one would anticipate from hydrocarbons. Hence, there must be a significant contribution from oxygenates in the formation of coke (besides, their obvious contribution to char, discussed later). According to the results obtained in the char/coke analysis of this study and the postulated mechanisms for coke formation discussed previously, the most important mechanisms for coke formation with origins in oxygenated compounds are Diels-Alder and aldol reactions. A scheme involving these reactions is depicted in pathway RC of Figure 5-12. Furfural acting as a diene can react with a small olefin (from the hydrocarbon pool) yielding tolualdehydes, which can undergo aldol condensation reactions (inside or outside the ZSM-5 pore) to form polyaromatics of the form proposed by Brewer et al.[38] The aldol is indeed an interesting pathway, because it can lead to polyaromatics with carbonyl and hydroxyl end groups, which are clearly evident in the FTIR and Raman analyses. It can proceed inside the catalyst pore forming oxo-aromatics (Valle et al.[39]) or

continue outside of the zeolite, blocking both the micropores and the macropores of the catalyst (as observed in the BET analyses, Table 5-1).

Finally, in regards to char formation (besides the aforementioned aldol route), we look at the molecular structure of (1E,3E)-penta-1,3-diene-1,3,5-triol and (2E,4Z)-hepta-2,4-diene-1,4,7-triol, proposed by Vinu and Broatbelt[125] as major char precursors. These compounds (and other similar obtained by enol-keto tautomerizations) can act as dienes and dienophiles, which points strongly towards a Diels-Alder route for char formation. In Figure 5-12 we enumerate all the possible products of their Diels-Alder reactions, omitting the possible tautomerization and condensation steps (which would not significantly affect the aromatic structure of these intermediates). The first products of reaction RD.1 are all significantly larger (>10Å MPD) than the ZSM-5 pores or cavities. Hence, their formation can only occur in the catalyst macropores and on the catalyst surface. In the absence of catalyst they can lead to structures similar to those proposed by Brewer et al.[38] and it is likely that they are promoted at lower temperatures and slow heating rates, as indicated by the larger transmittance intensity of the FTIR carbonyl group in the glucose char from slow thermal pyrolysis. If we take into account the relatively narrow TPO DTG curves from slow thermal and slow catalytic pyrolysis of glucose and cellulose and the wide defect bands observed in the Raman spectra of the chars from slow thermal and slow catalytic pyrolysis of glucose, it is reasonable to assume that char is composed of a few oxygen-containing polyaromatics, that are preferably formed at lower temperatures (or their kinetics are slower).

5.4. Conclusions

In summary, the properties and the characteristics of the char and coke derived from thermal and catalytic pyrolysis are different. The formation of char and coke strongly depends on the biomass source and also on the pyrolysis conditions (e.g., heating rates). This study reveals that when glucose and pine are used as biomass feed in slow catalytic pyrolysis, catalyst deactivation due to formation of char and the corresponding loss of accessibility (surface coverage and macropore

blocking) becomes dominant. On the other hand, in the cellulose slow catalytic pyrolysis and all the Catalytic fast pyrolysis experiments, the formation of coke is attributed to catalyst micropore blocking. In Catalytic fast pyrolysis of glucose and pine, formation of catalytic coke proceeds in parallel to the formation of thermal char. We identified the char to coke ratio to be 3/7 (mass basis) for the case of glucose and it is theoretically feasible to do so for other biomass model compounds. The following conclusions were drawn in this work:

• In slow thermal pyrolysis, TPO results show that, for glucose and pine, similar oxidation reactivities of the char/coke products are obtained, compared to the corresponding slow catalytic char/coke. For cellulose, the oxygen content of the char in slow thermal pyrolysis is higher than that in slow catalytic pyrolysis. Glucose char is likely produced *via* thermal Diels-Alder and aldol reactions, while the origin of cellulose char also includes pyrolytic decomposition. Analysis of the TPO DTG peak shapes shows that cellulose char oxidation has a lower reaction order than pine and glucose; indicating the formation of a very narrow distribution of hydrocarbons and/or oxygenates.

• In slow catalytic pyrolysis, SEM, STEM and BET results confirm that macropore blocking occurs for glucose and pine, leading to minor accessibility of the volatiles to the catalyst, while micropore blocking occurs in the case of cellulose due to coking. Similar reaction orders for the char/coke oxidation are observed in TPO, compared to slow thermal pyrolysis. Application of the random pore model shows that, at slow catalytic pyrolysis of glucose, catalyst contributes only on the shape, surface area and pore length of the char formed, but not on its chemical composition.

• In fast thermal pyrolysis, with TPO DTG peaks shifting to lower temperatures, glucose and pine char/coke have higher oxygen content than the corresponding fast catalytic ones. Comparison of the TPO results of fast thermal pyrolysis char to those from Catalytic fast pyrolysis shows that there is no coke formation in fast thermal pyrolysis. Hemicellulose is

proposed to be the most significant char formation precursor in fast thermal pyrolysis of pine, on the basis of TPO deconvolution results.

• In Catalytic fast pyrolysis, as shown by BET, micropore blocking occurs for all the feedstocks, reflecting good accessibility to the zeolite, and thus a stronger overall catalyst effect than that of slow catalytic pyrolysis. The wide shapes of the TPO curves indicate that catalytic coke corresponds to a range of hydrocarbons or oxygenates, formed *via* different mechanisms. Common catalytic coke formation mechanisms are proposed for the glucose coke formation (on the basis of FTIR and Raman observations of diminishing carbonyl groups and decreasing defect bands, respectively), which are assumed to proceed in parallel to aldol and Diels-Alder reactions of oxygen containing biomass intermediates. The catalytic coke reactions are of the same type and antagonistic in nature to the reactions leading to aromatics, resulting in consumption of single-ring aromatics for the production of coke inside the zeolite cage.

CHAPTER 6 TOWARDS UNDERSTANDING THE COKE FORMATION IN CATALYTIC PYROLYSIS OF BIOMASS OVER ZSM-5 ZEOLITE AND SUPPORTED CATALYST: A STUDY USING MODEL COMPOUNDS

The results of this Chapter have been submitted for publication to Green Chemistry, 2015.

6.1. Introduction

Biomass pyrolysis is a themochemical process, typically operated in the temperature range of 400-600 °C in the absence of oxygen, to convert biomass into bio-oils, gases and solid chars.[6,137] Catalytic fast pyrolysis of lignocellulosic biomass, in the presence of zeolite catalysts, such as ZSM-5, has been proven to provide enhanced bio-oil selectivity to aromatic hydrocarbons.[28,56,96] However, not all carbon content in biomass is converted to bio-oil during the catalytic pyrolysis, due to the production of carbon oxides (CO and CO_2), light hydrocarbons (mostly methane, ethylene and propylene) and solid residue (char and coke). The production of solid carbonaceous residue not only results in lower carbon selectivity to bio-oil, but also causes catalyst deactivation, which largely impacts product selectivity. Control of coke and char formation during pyrolysis could be possible through innovative catalyst and process designs, in which fundamental understanding of the formation mechanisms of char and coke should be viewed as a prerequisite. The latter requires insight into coke and char structural characteristics and formation chemistry.

The characteristics of coke and char have been studied widely in the literature. Brewer et al.[38] proposed a structure of char formed by slow and fast thermal pyrolysis of switch grass derived from ^{13}C-NMR analysis. They estimated that aromatic clusters of 7-8 rings terminated by carbonyl and hydroxyl groups are representative of the composition of thermal char. Valle et al.[39] studied catalytic upgrading of bio-oil with methanol over ZSM-5. They showed two origins of coke, thermal and catalytic, by performing temperature programmed oxidation (TPO). By

deconvoluting the TPO peak, they also observed that catalytic coke is deposited mainly inside the zeolite crystal channels; whereas thermal coke is mostly formed outside of the zeolite crystals. Cheng and Huber[18] studied catalytic pyrolysis of furan over ZSM-5. They concluded that the soluble coke mostly consisted of aromatic rings and carbonyl groups. They identified the molecular weight distribution of soluble coke, using gel permeation chromatography (GPC), and concluded that the maximum molecular weight of soluble coke is beyond the limitation of a GPC column (MW >104). Extraction of the polyaromatic hydrocarbons (PAHs) from the biochar after pyrolysis was also performed by Fabbri et al.,[37] who found that the main PAHs in the biochar were naphthalene, phenanthrene, fluoranthene, and pyrene. Guisnet and Magnoux[40] reviewed the organic chemistry of coke formation. With transmission electron microscopy (TEM) coupled to electron energy loss spectroscopy (EELS), they showed that with HZSM-5 the structure of coke was similar to that of coronene (pregraphitic), while with USHY it was similar to that of pentacene (linear polyaromatic).

In previous work,[65] the physicochemical characteristics of the coke and char after thermal and catalytic pyrolysis of glucose, cellulose and pine sawdust were investigated. Characterization of the solid residue showed that char contains oxygen-rich aromatic compounds with carbonyl group as the side chains, whereas coke does not contain carbonyl groups (observed with TPO and Fourier Transform Infrared Spectroscopy); Char forms on the outer surface of the catalyst and deactivates the catalyst by surface coverage and macropore blocking, whereas the formation of coke occurs inside the catalyst micropores and results in micropore blockage (Observed with nitrogen sorption, Scanning electron microscopy and Focused ion beam-Scanning transmission electron microscopy).

In the analysis of coke and char formation mechanisms, model compounds are widely used for study of the reaction chemistry.[18,41–44] Model compounds for the study of coke formation can be lumped to aromatic hydrocarbons, aromatic oxygenates and small oxygenates. For instance, when

toluene is chosen as the precursor, coke forms under self-alkylation reactions[45] and/or side alkylation with propylene[46] under carbenium ion mechanisms. Similarly, Huang et al.[47] studied coke formation over ZSM-5 zeolite during ethylbenzene disproportionation at 25-450 °C, showing that at relatively high temperature (260-450 °C), coke is formed via oligomerization of the ethyl side chains. The ethyl cations from the dealkylation of ethylbenzene form oligomeric species and alkylcarbenium ions (mainly C3+ and C4+), which subsequently form coke via repeated intermolecular hydride transfer reactions. Besides carbenium ion mechanisms, toluene was proposed to proceed to radical reaction mechanisms leading to coke precursors at high temperature and vacuum.[43,48–50]

Cheng and Huber[18,51] performed catalytic pyrolysis of furan, showing Diels-Alder reaction pathways, followed by oligomerization, cyclization, cracking, isomerization, and hydrogen transfer reactions as the main pathways for coke formation. Oxygenated aromatics were seen to give rise to significantly different mechanisms of coke formation. According to Ramasamy et al.,[52] biomass-derived small oxygenates, such as acetaldehyde, acetic acid and ethyl acetate, when pyrolyzed at 360 °C and 300 psig, participated in aldol condensation reactions, leading to olefins and single-ring aromatic hydrocarbons, which are considered to be coke precursors. Moreover, coke formation from propanal over ZSM-5 was studied by Hoang et al.,[53] who found that coke formation proceeds via aldol condensation followed by cyclization.

In this work, we are mainly interested in the mechanisms of coke formation from compounds that are products of biomass (catalytic) pyrolysis and at conditions relevant to pyrolysis (600 °C and 1 atm). We used the existing literature as a guideline for anticipated reactions and mechanisms. We also used existing knowledge on the coking activity of several chemicals in concert with existing measurements of dominant products from biomass pyrolysis[65] to determine a set of model compounds of relevance to coke formation. The latter allowed to eliminate the primary biomass decomposition reactions, which leads to char and substantially different chemistries.[125] Small

molecules with kinetic diameters smaller than the ZSM-5 largest cavity (7 Å), such as toluene, propylene, tolualdehyde, and furan are used. These four representative model compounds are explored for the identification of reaction pathways for coke formation from aromatics, olefins, aldehydes and oxo-aromatics. The coke formation pathways are discussed in comparison with those from the literature. Moreover, the characteristics of coke from each model compound are analyzed in an effort to reveal the contribution of different functional groups to coke formation. Overall, this study tries to explore the mechanism of coke formation; understand the role of oxygen in coke formation; reveal the coke structure; study the impact of the support on coke formation.

6.2. Experimental section

6.2.1. Catalysts

Commercial ZSM-5 catalyst from W.R. Grace & Co. was used in the analysis of the contribution of the support on coke formation. Comprehensive characterization of this catalyst in terms of morphology, porosity and acidity can be found in Du et al.[61] ZSM-5 zeolite (CBV 8014) from Zeolyst International was used in the analysis of coke formation mechanisms during catalytic pyrolysis of each model compound. Supported ZSM-5 catalyst from W. R. Grace & Co was also used to study the effect of support on coke formation. A detailed characterization of these two catalysts is shown in Table 6-1.

Table 6-1: Characterization of the supported ZSM-5 catalyst and Al_2O_3-SiO_2 matrix[a]

	Physical property		Porosity analysis[b]			Acidity analysis[c]	
	ρ_{bulk} (kg/m^3)	d_p (μm)	S_{total} (m²/g)	S_{micro} (m²/g)	V_{micro} (cm^3/g)	SiO_2/Al_2O_3 molar ratio	B.s./L.s
ZSM-5 catalyst	800	75~175	124.30	98.98	4.61E-2	-	11.15
ZSM-5 zeolite	500	0.5~2	418.84	292.72	13.56E-2	80	0.59

[a]In the table, ρ_{bulk} stands for bulk density; d_p, particle size; S_{total}, BET surface area; S_{micro}, t-plot micropore area; V_{micro}, t-plot micropore volume; B.s., Brønsted acid sites; L.s., Lewis acid sites. [b]Porosity analysis was

performed in Micrometitics ASAP 2020 Accelerated Surface Area and Porosimetry System. Samples were degassed at 250 °C under vacuum for 12 h before analysis. [c]Acidity analysis was performed by Diffuse Reflectance Infrared Fourier Transform Spectroscopy (DRIFTS). ZSM-5 and matrix were calcined in air at 350 °C for 3 hours, and then diluted with KBr to 6 wt%. Enough pyridine (99 wt%) was added to the samples to achieve saturation. Physisorbed pyridine was removed by heating the samples up to 150 °C under vacuum. Extinction coefficients of 1.67 cm/μmol and 2.22 cm/μmol are used for concentration calculation of Brønsted and Lewis acid sites, respectively.[66]

6.2.2.Experimental setup and procedure

A picture of the bench scale reactor used in this work is shown in Figure 2-4. The catalyst bed consisted of ZSM-5 zeolite or catalyst held in place by two plugs of quartz wool in a quartz tube reactor (22 mm ID). The reactor was heated by a vertical tube furnace to 600 °C, and the bed temperature was controlled using a K-type thermocouple placed in the middle of the reactor. A saturator was used to feed the reactants to the reactor via entrainment by Ar. The saturator temperature was maintained at 10 °C above the boiling point of the main reactant, measured by a thermocouple. The space velocity of the system was controlled by using Ar as a carrier gas at constant flow rate of 50 sccm. The gas residence time was calculated in the range 2.4-7.2 sec when ZSM-5 zeolite is used and 1.5-7.5 sec when ZSM-5 catalyst is used.

During the experiments, varying loadings of ZSM-5 zeolite or catalyst (1 gr, 2 gr, 3 gr) were placed in the reactor. The reactor was placed in a furnace with Ar flow until the temperature reached set point. One gram of reactant was then injected through a septum into the preheated saturator. For the experiments with propylene, 10% (0.17 gr) and 60% (1.03gr) propylene in Ar were fed into the reactor for 20 min. In the experiments of propylene with toluene, 1 gr of toluene and 0.17 gr of propylene were co-fed to the reactor. The system was purged with argon (50 sccm) until no other gas could be detected by the MS. The condensable products were collected in an impinger filled with 20 mL methanol in dry ice. After completion of the experiment, the coked zeolite/catalyst was collected and separated from the quartz wool. An additional 15 mL of methanol was used to rinse the impinger and the base of the reactor tube. All liquids were collected and analyzed.

In order to test the repeatability of the experiments, standard experiments at each zeolite to feed ratio were performed at least three times and the standard derivation was calculated for furan. The standard derivation was then applied to all the experiments with different model compounds in order to show the system error and repeatability of the experiments. The accuracy of each experiment was further validated by its overall mass balance. Only the experiments with ≥90 wt% mass balance were kept and shown here. For the special case of catalytic pyrolysis of furan, ≥80 wt% mass balance was accepted due to the presence of water in liquid product, which was not measured.

6.2.3.Product Analysis

Gas products were analyzed online with mass spectrometry (MS, Agilent 5975C, inert with triple axis detector). The MS was calibrated using standard gases (H_2, CH_4, CO (C_2H_4), CO_2, C_3H_6, and Ar). Liquid products were analyzed using an Agilent 6890N Gas Chromatograph equipped with a 5973N mass selective detector (GC-MS) and Agilent DB-5 column. A split ratio of 50:1 and temperature program starting at isothermal setting at 40 °C, followed by a 10 °C/min ramp to 270 °C was applied for furan, benzene and toluene quantification. All other compounds were identified with a splitless injection and temperature program starting at 40 °C, followed by a 1 °C/min ramp to 87 °C and a 20 °C/min ramp to 270 °C. Quantification standards consisting of furan, benzene, toluene, xylene, styrene, indene, naphthalene, tolualdehyde were calibrated. All other compounds were analyzed using the semi-quantification method.

The weight percent of coke on zeolite or catalyst was determined by weight loss during temperature programmed oxidation (TPO) at temperatures up to 900 °C, using a Q-500 thermogravimetric analyzer from TA instruments. For TPO, all samples were held at 120 °C for 30 min in order to remove moisture and then heated to 900 °C at a heating rate of 15 K/min. Raman spectra were obtained for coked zeolites in a Renishaw 2000 Ramanscope, operated with

a 0.024 in focus length, 514.5 nm laser excitation source (2.41 eV), at 20% power and 32 exposure times, to avoid detector saturation. For each sample, laser focus was set to 40% to prevent local damage and 3 different positions were analyzed to verify the spectra. Elemental analysis of the coked zeolites was performed in a Vario MICRO Elemental Analyzer from Elementar Americas Inc. Right before each analysis, samples were dried in an oven at 100 °C for 3 hr. Diffuse Reflectance Infrared Fourier Transform Spectroscopy (DRIFTS) of the coked zeolites was performed in a NICOLET 6700 Fourier Transform Infrared Spectroscopy (FTIR) from Thermo Scientific, equipped with an MCT detector and a Praying Mantis DRIFTS cell from Harrick Scientific. Pure KBr was used as background and samples were diluted in KBr (0.5 wt% concentration) for each analysis. Solid-state magic angle spinning (MAS) Nuclear magnetic resonance (NMR) spectra were acquired with a Bruker Avance III 400 MHz spectrometer operating at field strength of 9.4 T, corresponding to a frequency of 400 MHz for 1H and 100.6 MHz for ^{13}C by using a triple resonance 2.5 mm MAS probe. Samples were packed in a Zirconia rotor with Vespel caps and spun at 35 kHz at room temperature. Quantitative direct polarization ^{13}C MAS NMR spectra were acquired with 90° pulse width of 2.5 s, delay time of 120 s ($> 5T_1$) and 100 kHz of spectral width using spinal 64 high power proton decoupling. Chemical shifts were given with respect to tetramethylsilane (TMS) by using an external reference of glycine (carbonyl at 176.5 ppm) for ^{13}C as the secondary reference. The coked zeolites were characterized in NMR without prior HF and CH_2Cl_2 treatment, in order to measure the complete characteristics of both soluble and insoluble coke.[40]

6.3. Results and discussion

In this study, toluene, propylene, tolualdehyde and furan were used as biomass model compounds. GC-MS was used to analyze the liquid composition. MS was used for on-line gas composition analysis. TPO and elemental analysis were used for analysis of H and C content in

coke. Raman, DRIFTS and solid state ^{13}C NMR were used for the analysis of physicochemical properties and structure of coke. All experiments were performed at 600 °C and 1 atm.

6.3.1. Coke formation from catalytic pyrolysis of toluene

Figure 6-1 (a, b) shows the product yields and overall product selectivity from catalytic pyrolysis of toluene using ZSM-5 zeolite. The conversion of toluene was enhanced by higher zeolite to toluene ratios. Coke formation was promoted by catalytic reactions, with a parallel decrease in the liquid yield. Minor amounts of hydrogen and methane were measured. Table 6-1 lists the selectivity of all the liquid products, obtained from the catalytic pyrolysis of toluene. The selectivity to xylenes, indenes, benzene derivatives, biphenyls, and the sum of the heavy PAHs (≥ 3 rings) decrease as catalyst to toluene ratio increases, which implies their possible role as catalytic coke precursors or intermediates for the formation of other compounds, such as naphthalenes.

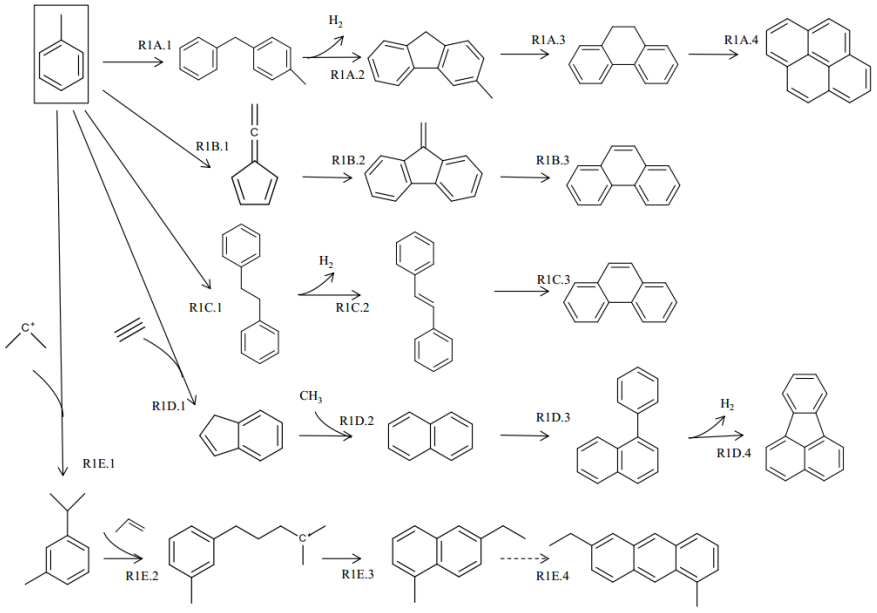

Scheme 6-1: Possible reaction pathways for PAH formation from (catalytic) pyrolysis of toluene and toluene with propylene.

R1A[45] – R1A.1 (toluene self-alkylation), R1A.2 (dehydrogenative coupling), R1A.3 (isomerization) and R1A.4 (hydrogen transfer and repetition of R1A.1–R1A.4); R1B [49] – R1B.1 (isomerization), R1B.2 (fulvenallenyl radical self-alkylation) and R1B.3 (isomerization); R1C[49] – R1C.1 (self-alkylation), R1C.2 (dehydrogenation) and R1C.3 (cyclization); R1D[49,50] – R1D.1 (alkylation and cyclization), R1D.2 (alkylation and ring rearrangement), R1D.3 (alkylation with phenyl radical) and R1D.4 (dehydrogenation); R1E[46] – R1E.1 (alkylation on the nucleus with carbenium ions), R1E.2 (side alkylation and isomerization), R1E.3 (cyclization), and R1E.4 (repetition of R1E.2, R1E.3)

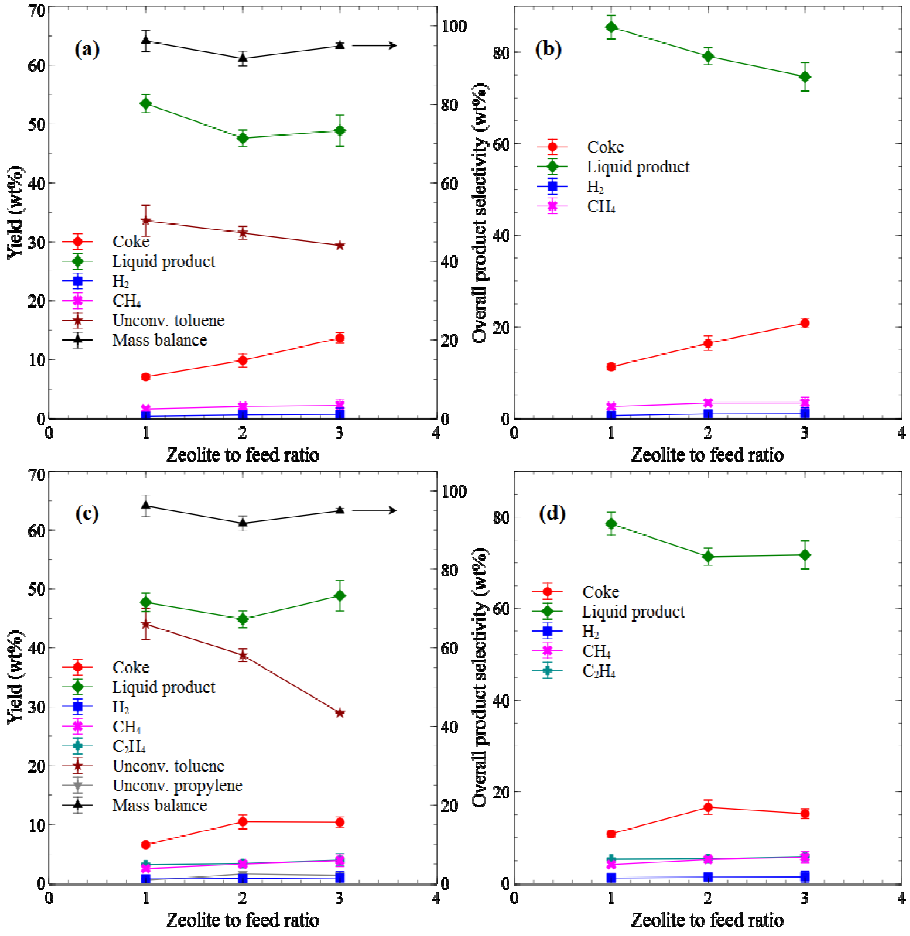

Figure 6-1: Product distributions from catalytic pyrolysis of (a) toluene in yield, (b) toluene in overall product selectivity, (c) toluene with propylene in yield and (d) toluene with propylene in overall product selectivity using ZSM-5 zeolite

Styrene, which was previously observed to be a major liquid product when supported ZSM-5 catalyst was used for the catalytic pyrolysis of miscanthus × giganteus,[61] is not formed in the pyrolysis reactions with ZSM-5 zeolite. However, as shown later in catalytic pyrolysis of toluene

with supported ZSM-5 catalyst, styrene is observed in the liquid product. This means that styrene is extremely reactive, contacting with the strong acid sites in ZSM-5 zeolite, when it is unsupported and pure. Benzo[a]fluorene (kinetic diameter 7.41 Å[56]), triphenylene (kinetic diameter 7.54 Å[56]) and pyrene (kinetic diameter 7.24 Å[56]) were observed as the largest diameter liquid product compounds. The kinetic diameters of these three compounds are very close to the pore constrains of ZSM-5 (largest cavity 7 Å, pore limiting diameter 5 Å[138]).

Table 6-2: Detailed liquid product selectivity from catalytic pyrolysis of toluene using ZSM-5 zeolite*

Zeolite to toluene ratio	1:1	2:1	3:1
Benzene	47.56 ± 6.40	49.89 ± 3.07	48.15 ± 5.75
Xylene	22.85 ± 0.10	18.07 ± 4.49	15.37 ± 2.41
Styrene	-	-	-
Indenes	2.07 ± 0.54	1.52 ± 0.34	1.26 ± 0.41
Naphthalenes	4.38 ± 2.33	4.98 ± 0.68	5.08 ± 0.44
Benzene derivatives	0.96 ± 0.63	0.23 ± 0.33	0.24 ± 0.34
Biphenyls	3.03 ± 0.27	2.09 ± 1.23	2.08 ± 0.71
Bibenzyl & (E)-Stilbene	0.12 ± 0.04	0.11 ± 0.00	0.09 ± 0.03
Fluorenes	1.49 ± 0.45	0.73 ± 0.02	0.84 ± 0.28
Anthracenes & Phenanthrenes	2.41 ± 0.73	1.31 ± 0.03	1.14 ± 0.38
Fluoranthene & Pyrenes	0.28 ± 0.08	0.28 ± 0.01	0.27 ± 0.09
11H-Benzo[a]fluorene	0.32 ± 0.10	0.13 ± 0.00	0.09 ± 0.03
Triphenylene	0.11 ± 0.03	-	-
Total	85.59 ± 2.58	79.34 ± 1.86	74.61 ± 3.09

*Indenes include indene, 1-methylindene; Naphthalenes include 2-methylnaphthalene, 1-methylnaphthalene, 2,6-dimethylnaphthalene; Benzene derivatives include 1,2,3-trimethylbenzene, 1,3,5-trimethylbenzene, 1-ethenyl-3-methylbenzene; Biphenyls include biphenyl, 2-methyl-1,1'-biphenyl, 4-methyl-1,1'-biphenyl, 2,2'-dimethylbiphenyl, 3,3'-dimethylbiphenyl, 4,4'-dimethylbiphenyl, 2,3'-dimethyl-1,1'-biphenyl, diphenylmethane; Fluorenes include fluorene, 2-methyl-9H-fluorene, 3-methyl-9H-fluorene, 2,3-dimethyl-9H-fluorene, 1,1'-methylenebis[4-methyl]benzene, 1-methyl-2-[(3-methylphenyl)methyl]benzene; Anthracenes & Phenanthrenes include anthracene, 2-methylanthracene, phenanthrene, 1-methylphenanthrene, 4-methylphenanthrene, 9,10-dihydro-1-methylphenanthrene, 3,6-dimethylphenanthrene, 1a,9b-dihydro-1H-Cyclopropa[l]phenanthrene, 2-phenylnaphthalene, diphenylethyne, 2-phenyl-1H-Indene; Fluoranthene & Pyrenes include fluoranthene, 1-methylpyrene.

Several studies have focused on modeling the reaction pathways of the formation of PAHs (coke precursors) in toluene pyrolysis, but a comprehensive study at typical biomass pyrolysis conditions (1atm, 400-600 °C) is missing. Zhang et al.[48] studied the reaction pathway through diphenylmethane and fluorene (Scheme 6-1, R1A) for phenanthrene formation in toluene

pyrolysis at 20 Torr and 997-1597 °C. They also proposed a bibenzyl cyclization reaction pathway (Scheme 6-1, R1C). Production of diphenylmethane was also observed by Svelle et al.,[139] in transmethylation of toluene over zeolites. Similarly, Lannuzel et al.[43] proposed a toluene pyrolysis mechanism (specifically focused on diphenylmethane and bibenzyl) under high pressure of 700 bar and temperatures of 300-400 °C. They concluded that formation of bibenzyl was from two benzyl radicals, while formation of diphenylmethane proceeded through benzyl radical addition on an aromatic ring. Matsugi and Miyoshi[49] studied the formation of naphthalene and phenanthrene during the pyrolysis of toluene at low pressure (~10 Torr) and high temperature (1032 °C). They reported that the largest contribution in naphthalene formation was from the methyl addition to indenyl radical, a product from benzyl radical and acetylene, followed by ring-rearrangement of the methyleneindanyl radical. For the formation of phenanthrene, the reaction through 5-ethenylidenecyclopenta-1,3-diene is one pathway (Scheme 6-1, R1B), but the dominant path is through cyclization of bibenzyl (Scheme 6-1, R1C). Matsugi and Miyoshi[49] also proposed the alkylation of toluene with acetylene for the formation of indene, which leads eventually to the formation of naphthalene (Scheme 6-1, R1D 1&2). Furthermore, Colket and Seery[50] proposed a reaction mechanism leading to the formation of fluoranthene, which is also seen in the final products from catalytic pyrolysis of toluene. In their pathway, naphthalene is treated as intermediate participating in radical reactions (Scheme 6-1, R1D 3&4).

Overall, although the free radical pathways (at high temperature) proposed for biomass pyrolysis are still under debate and other reaction mechanisms such as the ionic and concerted mechanisms[125] have been proposed, the radical reaction pathways are primary candidates for understanding coke formation in toluene catalytic pyrolysis. The important reaction intermediates leading to PAH formation mentioned in the literature such as diphenylmethane, bibenzyl and biphenyl are all observed in the current study (Table 6-2). The trends of decrease of biphenyls, bibenzyl and the heavy PAHs in liquid selectivity as catalyst to feed ratio increases, in addition to

higher coke yields, are clear indications of the main coke formation mechanisms R1A and R1C. Coke formation in catalytic pyrolysis of hydrocarbons mainly proceeds via reactions with biphenyls, bibenzyl and heavy PAHs, which is consistent with our previously proposed reaction network.[65]

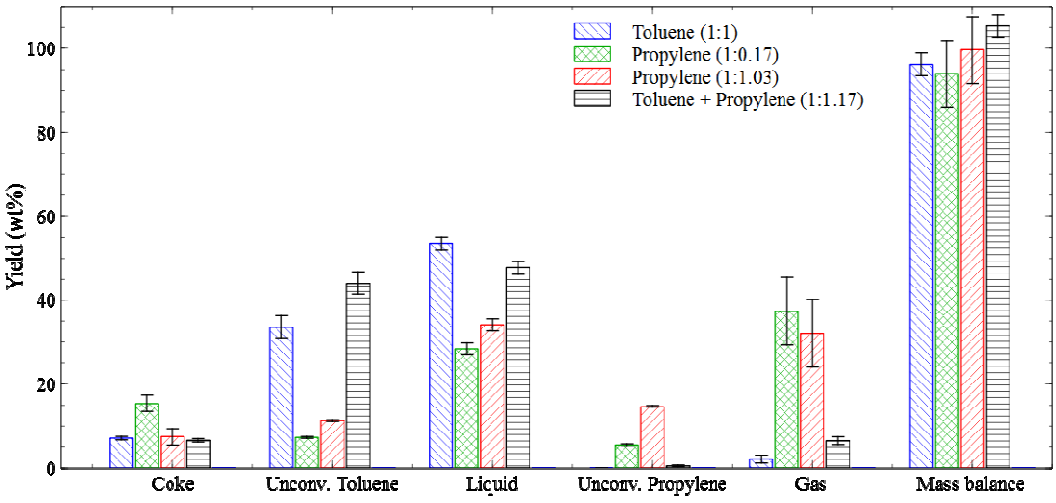

Figure 6-2: Comparison of product yields in catalytic pyrolysis of toluene, propylene, and toluene with propylene cofeeding using ZSM-5 zeolite

6.3.2.Effect of cofeeding an olefin compound on coke formation

Figure 6-1 (c, d) shows the product yields and overall product selectivity from catalytic pyrolysis of toluene co-fed with propylene using ZSM-5 zeolite. By cofeeding with propylene, the conversion of toluene is significantly reduced at relatively low zeolite to feed ratio due to the competitive occupation of the zeolite active sites by propylene. Substantial quantity of ethylene is produced in the cofeeding experiments compared with those with pure toluene, possibly due to the thermal decomposition of propylene or cracking of its oligomerization derivatives. A more detailed comparison of product yields in catalytic pyrolysis of toluene, propylene, and toluene with propylene is shown in Figure 6-2. Regardless of the conversion of the feed, coke and gas yields are maximized in catalytic pyrolysis of propylene (Zeolite/Feed ratio 1:0.17). It is well

known that formation of coke is extensive in catalytic pyrolysis of olefins over ZSM-5 zeolite or fluid catalytic cracking (FCC) catalyst.[51,140,141] In the experiments shown in Figure 6-2, at zeolite to propylene weight ratio of 1:0.17, coke yield is measured at 15.40 wt%. At experiments with about 1:1 zeolite to feed ratio, coke yields after catalytic pyrolysis of toluene, propylene and toluene with propylene cofeeding are very similar. This means that cofeeding of toluene with propylene does not enhance the coke formation. Instead, the liquid product yield is reduced in the cofeeding compared with just toluene, with a parallel increase in the gas products. The decrease in liquid selectivity is mostly attributed to smaller yields to xylene and biphenyls, as shown in Figure 6-3. This means that the presence of propylene in catalytic pyrolysis of toluene restricts the formation of xylene and biphenyls or promotes their conversion to form larger aromatics (e.g. naphthalene).

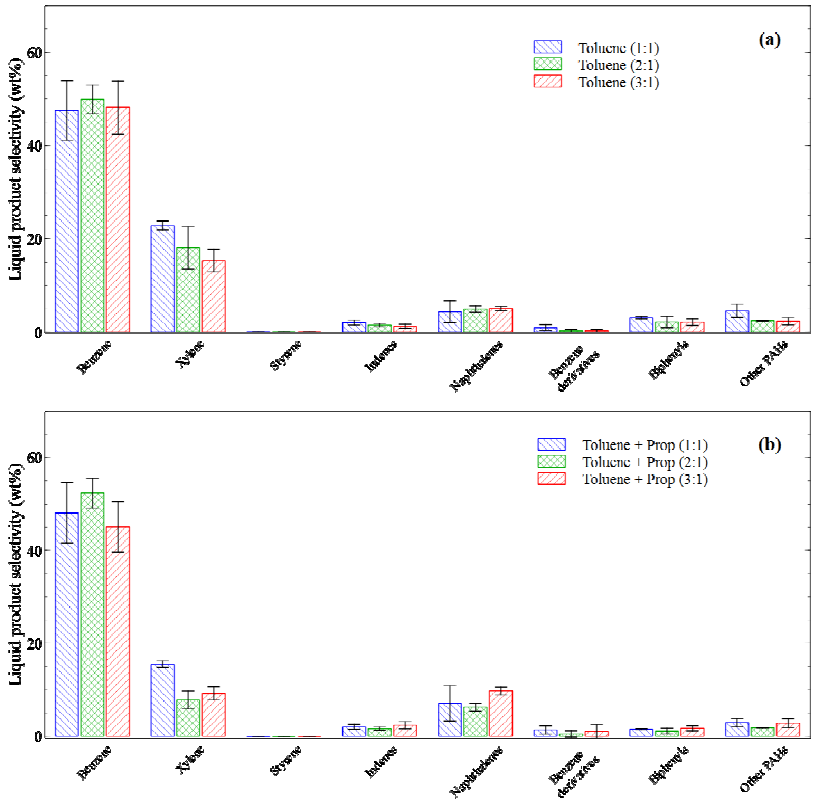

Figure 6-3: Comparison of liquid product selectivity from catalytic pyrolysis of (a) toluene with propylene cofeeding and (b) that of toluene, using ZSM-5 zeolite

Quintana et al.[46] proposed an ionic mechanism (Scheme 6-1, R1E) for the formation pathway of a coke precursor (alkylated phenanthrene) in catalytic cracking of 1-butene over FCC zeolite catalyst at 530 °C. In the mechanism R1E of Scheme 6-1, butene is proposed to act as a preferential alkylant agent for alkylation of toluene.[46] Further alkylation of the resulting alkylated aromatic by propylene leads to coke formation. The reaction proceeds through the formation of o-cymene, intermediate. Although the existence of cymene is not observed in the liquid product after catalytic pyrolysis of toluene with propylene in this work, the reaction pathway for coke formation through alkylation of propylene and toluene is possible if we assume complete conversion of the substituted aromatic intermediates. Actually, the formation of cymene through alkylation of propylene and toluene is usually observed at relatively lower temperatures (200-250 °C).[142,143] The decrease in the yield to xylene and biphenyls and the increased formation of naphthalene in the experiments of toluene co-fed with propylene, compared to those with pure toluene, are strong indications of the reaction pathway R1E in Scheme 6-1.

Overall, the presence of propylene does not influence the conversion of toluene to coke. Although thermal decomposition of propylene or propylene derivatives to methane, ethylene, and hydrogen occurs (Figure 6-1 (c, d)), most of the propylene forms toluene and benzene as the intermediate products and possibly follows the coke formation mechanism proposed by Quintana et al.[46] Nonetheless, the effect of propylene cofeeding on coke formation is model-compound-dependent according to the literature. For example, lower coke formation in the presence of propylene was observed by Cheng and Huber[51] in the catalytic pyrolysis of furan. On the other hand, Prasomsri et al.[144] studied the catalytic conversion of anisole over HY zeolite at 400 °C. With propylene cofeeding, the formation of coke was enhanced, compared to that with pure anisole.

6.3.3.Contribution of aromatic carbonyl groups to coke formation

Figure 6-4 (a, b) shows the product yields and overall product selectivity from catalytic pyrolysis of tolualdehyde. A complete conversion of tolualdehyde was observed for all the zeolite to feed ratios. Consistent with the pyrolysis of toluene, coke formation is enhanced as catalyst to feed ratio increases. Catalytic pyrolysis of tolualdehyde results in significant amounts of CO. It is surmised that decarbonylation reaction occurs at the initial stage of the pyrolysis, leading to the formation of toluene and CO. Ausavasukhi et al.[145] studied the catalytic pyrolysis of benzaldehyde over gallium-impregnated ZSM-5. They found that on strong Brønsted acid sites, benzaldehyde decomposes to benzene and CO (Scheme 6-2, R2A). Thermal reaction of benzaldehyde to benzyl benzoate by a polymerization reaction at 350-370 °C was observed by Hurd and Bennett[146] (Scheme 6-2, R2B), while they also reported the decomposition of benzaldehyde to benzene and CO (Scheme 6-2, R2A) at elevated temperature (680-690 °C). The thermal cracking of benzaldehyde to benzene and CO at high temperature (1327 °C) was reported by Vasiliou et al.[147] Based on the observations from the literature,[145–147] it is likely that the decarbonylation reaction can happen at the initial stage of tolualdehyde catalytic pyrolysis over ZSM-5 zeolite at 600 °C.

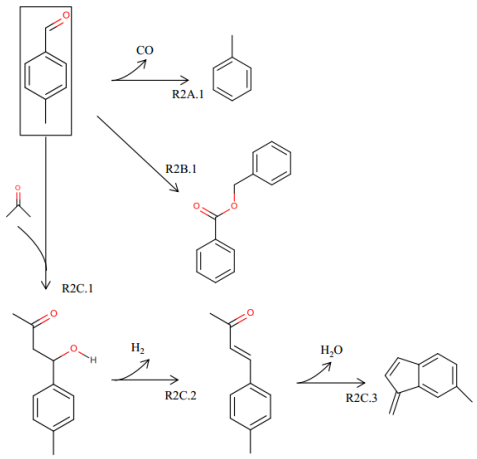

Scheme 6-2: Possible reaction pathways for catalytic pyrolysis of tolualdehyde.

R2A[145] – R2A.1 (decarbonylation); R2B [146] – R2B.1 (polymerization); R2C[148] – R2C.1 (aldol condensation), R2C.2 (dehydrogenation), R2C.3 (dehydration and cyclization)

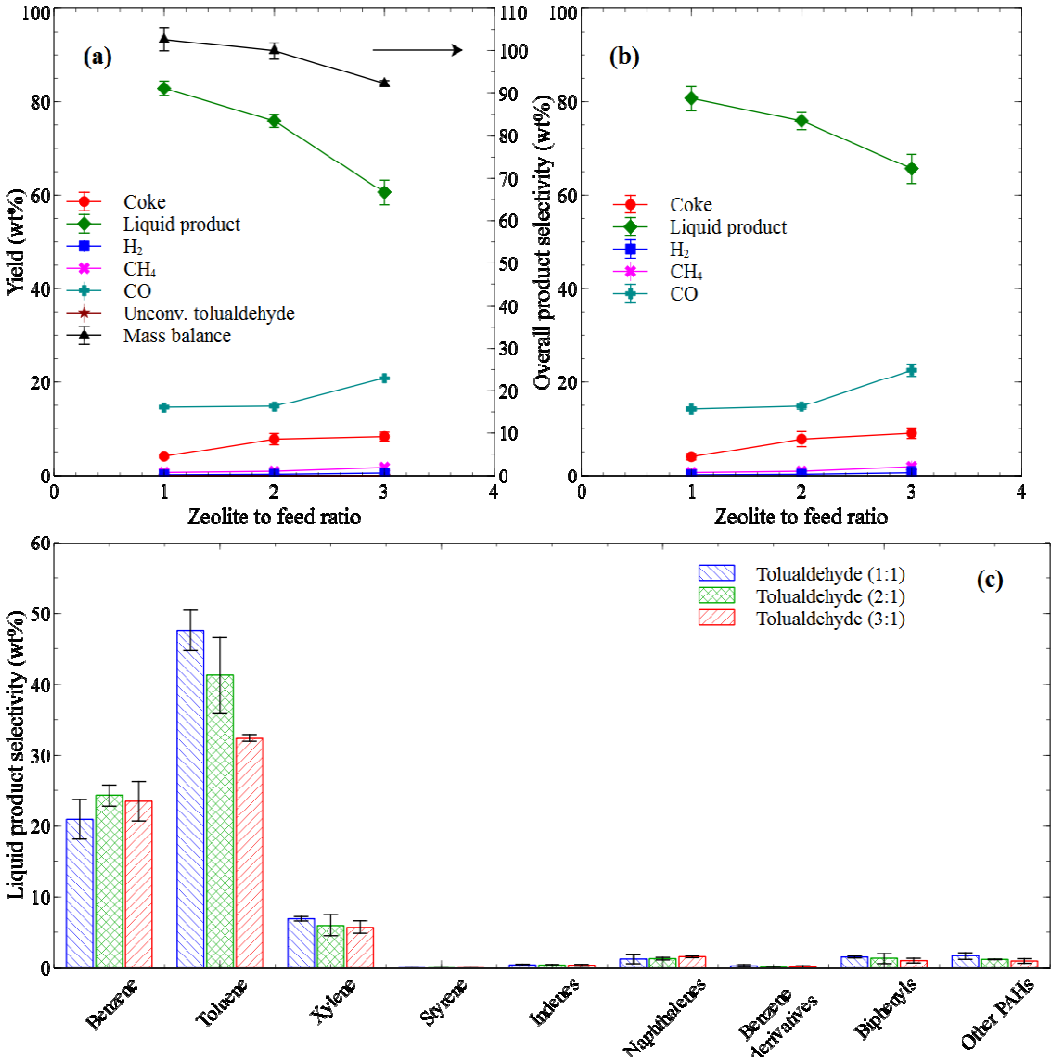

Figure 6-4: Product distributions from catalytic pyrolysis of tolualdehyde using ZSM-5 zeolite: (a) product yields; (b) overall product selectivity; (c) liquid product selectivity

Figure 6-4 (c) shows the liquid selectivity from catalytic pyrolysis of tolualdehyde over ZSM-5 zeolite. The liquid product selectivity in catalytic pyrolysis of tolualdehyde is different from that from catalytic pyrolysis of toluene, mainly because toluene was not taken into account as liquid product in the catalytic pyrolysis of toluene. The selectivity to naphthalenes increases as zeolite to

feed ratio increases, whereas the selectivity to all other compounds decreases at higher zeolite to feed ratios. This trend is consistent with the liquid product selectivity of toluene pyrolysis. Overall, by comparing the liquid selectivity of the two reaction systems (toluene and tolualdehyde), the same qualitatively products were measured. The existence of an aromatic carbonyl end group does not lead to different coke formation pathways. Verification of the explicit dominance of decarbonylation as the initial step in the pyrolysis of tolualdehyde is significant. In Figure 6-5, major products from catalytic pyrolysis of tolualdehyde are compared with those calculated from the results of toluene pyrolysis, based on the assumption that tolualdehyde is stoichiometrically converted to toluene and CO at the initial step of pyrolysis. At all catalyst to feed ratios, coke, benzene and xylene yields from experiments are generally consistent with the corresponding calculated values.

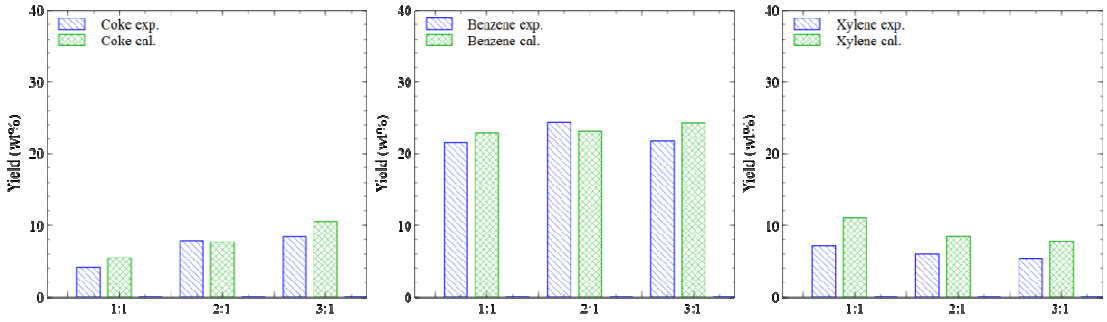

Figure 6-5: Verification of the initial step for catalytic pyrolysis of tolualdehyde over ZSM-5 zeolite.

Experimental results are reported directly from tolualdehyde pyrolysis. Calculated results are based on the assumption that tolualdehyde is completely converted to toluene and CO at the initial step and following exactly the toluene pyrolysis pathway.

In Scheme 6-2, R2C, aldol condensation of tolualdehyde and acetone is proposed as the initial reaction for aromatics production and eventually leads to coke. Mettler et al.[105] discussed the potential role of aldol condensation in the formation of pyrolysis char. They pointed out that there might be a connection between char formation during pyrolysis (400-600 °C) and humin

formation during aqueous phase conversion at low temperature (<200 °C). Since the formation of humin through aldol condensation during aqueous phase conversion of biomass and biomass-derivatives is well studied,[149–151] it will be beneficial to the study of char and coke formation in biomass pyrolysis, if formation of pyrolysis char is proven to follow the same reaction mechanism as humin formation through aldol condensation. However, by comparing the experiment and theoretical calculations of this study (Figure 6-5), the decarbonylation reaction is considered as the dominant reaction in tolualdehyde catalytic pyrolysis at 600 °C. It seems that aldol condensation is not likely to happen at 600 °C during pyrolysis. This observation is consistent with Kamiguchi et al.,[148] who studied the aldol condensation of benzaldehyde and acetone over a supported Ta cluster. They observed that, at temperature lower than 375 °C, the yield of E-4-phenyl-3-buten-2-one (aldol condensation product) increased with temperature, but at higher temperature (>375 °C) the decomposition of benzaldehyde to benzene dominated.

6.3.4. Coke formation from an aromatic oxygenate compound

Oxygenates and in particular furanic compounds are predominant in the liquid product of biomass pyrolysis. In this study, furan, a proven important biomass pyrolysis intermediate[18,59] is used as a model compound for the study of coke formation from aromatic oxygenates. As shown in Figure 6-6 (a, b), coke formation is enhanced by increasing zeolite to feed ratio. The overall selectivity to coke in the products from furan pyrolysis is much higher than that from toluene pyrolysis. The mass balance of catalytic pyrolysis of furan is in the range of 80-85%, due to the production of water. In Figure 6-6 (c), a significant decrease of the yield to indenes and PAHs is observed whereas the selectivity to toluene is increased at higher zeolite to feed ratios. It has been proposed that the production of aromatics in catalytic pyrolysis of furan over ZSM-5 is following the Diels Alder and ring-opening reaction pathways.[18,51,152] However, the coke formation mechanism is not clear. In the proposed reaction pathways by Cheng and Huber,[51] coke formation in catalytic pyrolysis of furan mostly begins from aromatic hydrocarbons and/or olefins in the so-called

"hydrocarbon pool" (Scheme 6-3, R3A). This suggests that although furan is an aromatic oxygenate, the oxygen in furan does not contribute to the structure of coke or to the formation pathways of coke formation. Moreover, this suggests that oxygen is not involved directly in coke formation reactions and coke should not contain oxygen in the form of carbonyl or hydroxyl groups. This will be verified in section 6.3.5 through elemental analysis and DRIFTS.

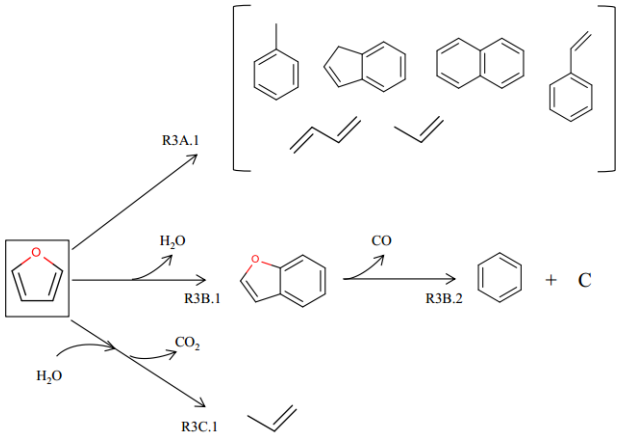

Scheme 6-3: Possible reaction pathways for catalytic pyrolysis of furan. R3A[51] – R3A.1 (Diels Alder to form the "hydrocarbon pool"); R3B[51] – R3B.1 (furan self-condensation), R3B.2 (decarbonylation), R3B.3 (cracking); R3C[153] – R3C.1 (hydrolysis)

The lack of oxygen in coke and its negligible contribution to coke formation pathway deem the necessity of catalytic coke formation study over zeolite to only nonoxygenates (aromatic hydrocarbons and olefins). Another interesting pathway comes from furan self-condensation (Scheme 6-3, R3B). Furan reacts with itself, forming water and benzofuran via ring opening.[152] Benzofuran has the ability to decompose to benzene, coke and CO.[51] According to the reaction stoichiometry, the coke shown in this mechanism contains mostly carbon content. The structure of the carbon produced during catalytic pyrolysis of furan is unknown at this point. Later characterization (Section 6.3.5) indicates that the coke from pyrolysis of furan has a highly condensed form compared with those from pyrolysis of other model compounds used in this

study. The last reaction pathway (Scheme 6-3, R3C) regarding coke formation is from furan hydrolysis from Gilbert et al.[153] Furan reacts with water to produce CO_2 and olefins. It is very likely that coke formation in this reaction follows the same pathways as olefins. Moreover, furan hydrolysis produced less coke than furan Diels-Alder condensation.

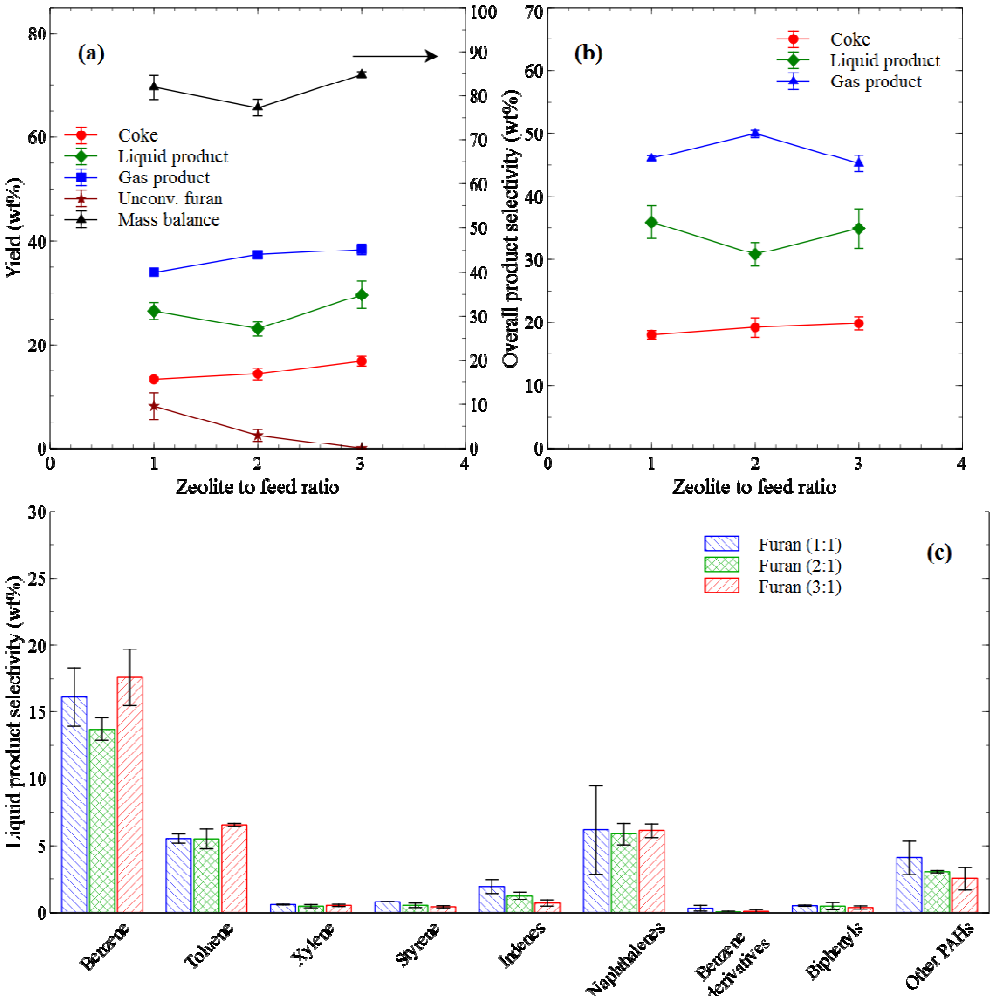

Figure 6-6: Product distributions from catalytic pyrolysis of furan using ZSM-5 zeolite: (a) product yields; (b) overall product selectivity; (c) liquid product selectivity

6.3.5.Characteristics of coke from different model compounds

Figure 6-7 shows Raman spectra of coked zeolites from catalytic pyrolysis of toluene, toluene/propylene, tolualdehyde and furan at 600 °C and 1:1-3:1 zeolite to feed ratios. The initial Raman spectra for coked zeolites from all model compounds show strong signals coming from fluorescence background,[154,155] so a consistent baseline correction has been performed to the Raman spectra. According to Schwan et al.,[156] the existence of D peak proves the existence of condensed benzene rings incorporated in the amorphous (hydrogenated) structure or highly disordered graphitic structure (sp^3 hybridization). G peak stands for E_{2g_2} mode of graphite or the C=C sp^2 stretching of olefinic or conjugated carbon chains. The broadening and position shift of the Raman G peaks are related to the integrated effect from carbon cluster size, distribution, stress, and chemical bonding.[157]

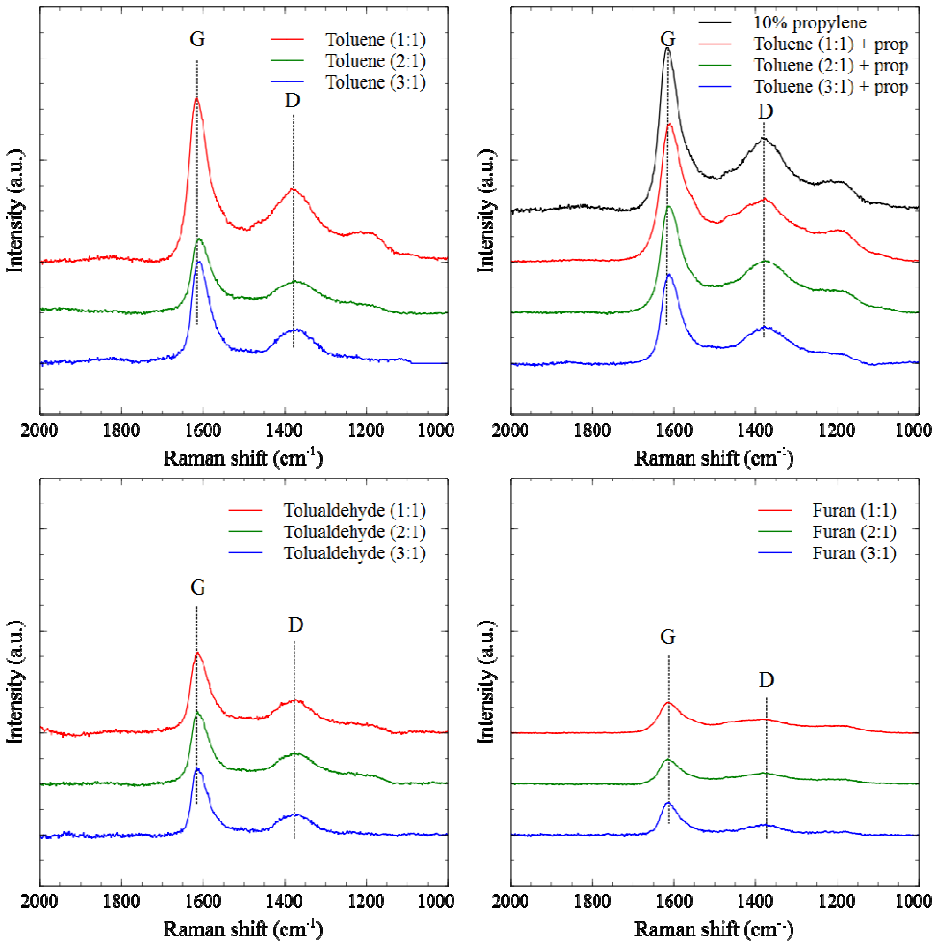

Figure 6-7: Normalized Raman spectra of coked zeolites from catalytic pyrolysis of toluene, toluene/propylene, tolualdehyde and furan using ZSM-5 zeolite at 600 °C, 1:1-3:1 zeolite to feed ratios

Table 6-3: Deconvolution of the Raman spectra of the coked zeolite from catalytic pyrolysis of toluene, toluene/propylene, tolualdehyde and furan using ZSM-5 zeolite at 600 °C, 1:1-3:1 zeolite to feed ratios

	G band		D band	I_D/I_G	L_a*
	Position [cm^{-1}]	Area [%]	Area [%]	ratio	[nm]
Toluene (1:1)	1614.73	53.66	46.34	1.16	3.79
Toluene (2:1)	1610.26	48.62	51.38	0.95	4.63
Toluene (3:1)	1608.77	41.28	58.72	0.70	6.29
10% propylene	1614.73	53.67	46.33	1.16	3.79
Toluene (1:1) + 10% propylene	1610.26	56.71	43.29	1.31	3.36
Toluene (2:1) + 10% propylene	1615.24	55.81	44.19	1.26	3.49
Toluene (3:1) + 10% propylene	1612.26	51.44	48.56	1.06	4.15
Tolualdehyde (1:1)	1613.24	48.70	51.30	0.95	4.63
Tolualdehyde (2:1)	1613.75	45.39	54.61	0.83	5.30
Tolualdehyde (3:1)	1616.73	41.00	59.00	0.69	6.38
Furan (1:1)	1615.24	54.87	45.13	1.22	3.61
Furan (2:1)	1615.24	49.75	50.25	0.99	4.44
Furan (3:1)	1613.75	42.50	57.50	0.74	5.95

*Graphitic in-plane crystallite size, L_a is calculated based on the equation mentioned in Ferrari and Robertson [157], where constant C(514.5nm) ~ 44 Å.

Table 6-2 summarizes the deconvolution peak areas for G band and D band. The ratio of the two bands, I_D/I_G, for all the samples are within the range of 0.5-1.5. Combining the I_D/I_G with the G band line width of 100-150 cm^{-1} for all the samples shown in Figure 6-7, it is shown that the coke from pyrolysis of all the model compounds used in this study contains structure similar to amorphous hydrogenated carbon (see Figure 6-5 in Ref.[156]). The ratio of the two bands, I_D/I_G, decreases for every model compound as the zeolite to feed ratio increases. This indicates more crystalline structures in coke produced from pyrolysis with increasing zeolite to feed ratio

regardless of the feed. The effect of other operating conditions, such as temperature, on coke crystallinity was studied by Ochoa et al.,[158] during thermal treatment of biooil. They reported that catalytic reactions enhance the crystallinity of the coke. Same conclusion can be drawn by studying the in-plane crystallite size, L_a.

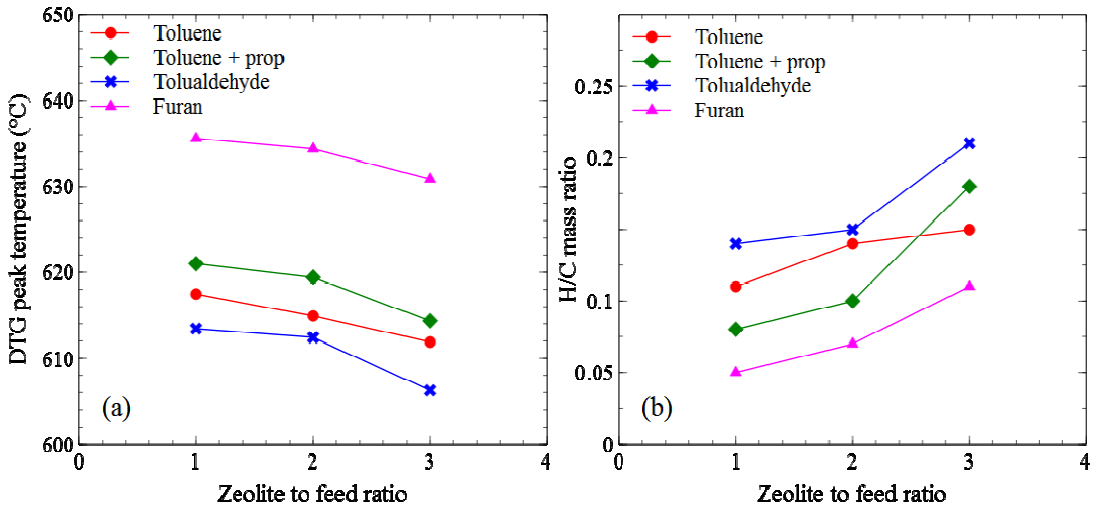

Figure 6-8: DTG peak temperature and H/C mass ratio of coked zeolites from different model compounds as a function of zeolite to feed ratio.

Figure 6-8 (a, b) presents the peak of the first differential thermogram (DTG) of the coked zeolites, and H/C mass ratio from elemental analysis as a function of zeolite to feed ratio. In Figure 6-8 (a), the DTG peak temperature decreases as the zeolite to feed ratio increases, indicating a relatively more condensed structure (more fused aromatic rings) at lower zeolite to feed ratios. Among the model compounds, furan has the most condensed form of coke after catalytic pyrolysis. Tolualdehyde has the least condensed structure of coke. Comparing the liquid analysis shown in Figure 6-3, 6-4 & 6-6, the structure of coke is likely related to the formation of naphthalenes and PAHs during pyrolysis (furan pyrolysis has highest selectivity to naphthalenes and PAHs whereas tolualdehyde has the lowest). Indicated by the DTG peak temperature, the

similar structures of coke from pyrolysis of toluene, toluene plus propylene and tolualdehyde confirm in part the hypothesis that similar mechanisms are responsible for their formation. As shown in R1C, R1E and R2A in reaction scheme 6-1 and 6-2, the coke precursors from pyrolysis of toluene, toluene plus propylene and tolualdehyde are similar three-ring PAHs, like anthracene or phenanthrene. The small differences seen in the DTG peaks of the coke from these compounds can be mainly attributed to the different effective toluene to zeolite ratio. Nonetheless, the consistency in the trends of these results is striking.

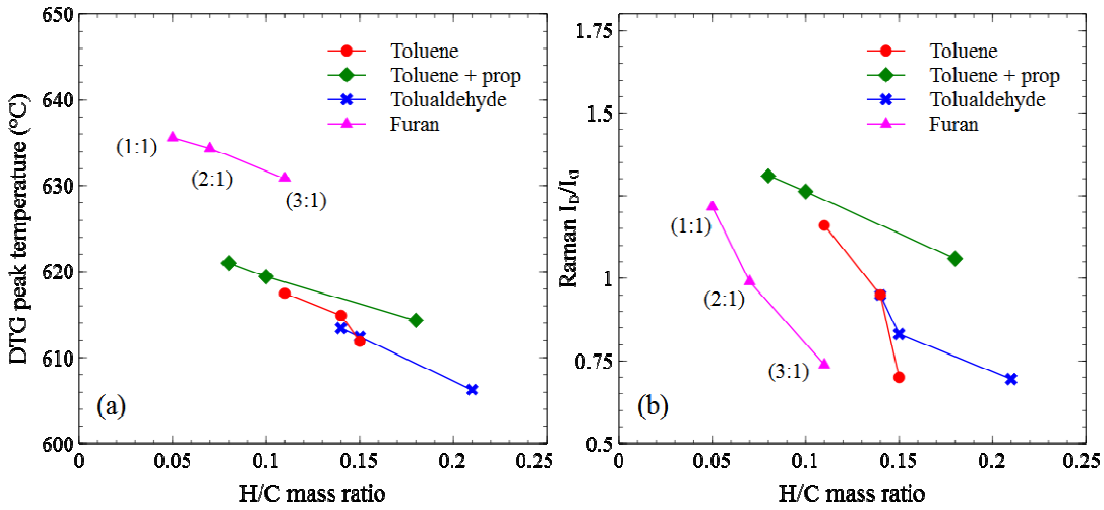

Figure 6-9: DTG peak temperature and Raman I_D/I_G ratio as a function of H/C mass ratio for coked zeolites from different model compounds.

The aromatic structure is further verified by elemental analysis, shown in Figure 6-8 (b). It is shown that H/C mass ratio increases with zeolite to feed ratio. This is consistent with the TPO results. All the coke samples have very low H/C ratio in the range of 0.05-0.2. For comparison, olefins (C_nH_{2n}) have H/C mass ratio of 0.17. The smallest aromatic compound, benzene (C_nH_n), has H/C mass ratio of 0.08. As more aromatic rings appear in the structure system, the H/C mass ratio becomes lower. When the structure of coke becomes more carbonaceous (e.g. $C_{2n}H_n$), the H/C mass ratio reaches 0.04. It is seen that coke from pyrolysis of furan has the lowest H/C mass

ratio (0.05), which indicates the highly hydrogen deficient structure (close to $C_{2n}H_n$) in the coke from furan. However, the coke from tolualdehyde at 3:1 zeolite to feed ratio has the highest H/C mass ratio of about 0.2, which might be attributed to the alkyl side chains on the aromatic rings in coke (see also FTIR and NMR results in the following).

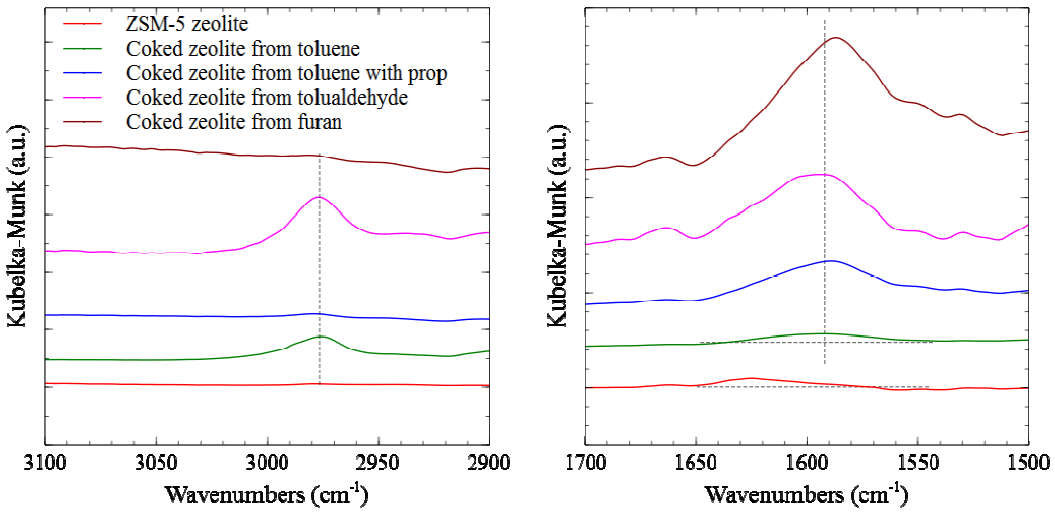

Figure 6-10: FTIR analyses for the coked zeolites from catalytic pyrolysis of different model compounds at 600 °C and 1:1 catalyst to feed ratio. Region 2900-3100 cm^{-1} represents sp^3 C-H stretching; 1500-1700 cm^{-1} C=C stretching aromatic

A correlation between the DTG peak temperature and the H/C ratio is shown in Figure 6-9 (a), where it is clear that coke from pyrolysis of furan has much higher DTG peak temperature and lower H/C mass ratio, compared with the coke from pyrolysis of the other three model compounds, representing a more condensed structure. Coke from toluene and tolualdehyde are very similar to each other. This further verifies that the reaction pathway in Scheme 6-2, R2A is responsible for both. Agreement is also reached by plotting the Raman I_D/I_G versus the H/C mass ratio, shown in Figure 6-9 (b). It is interesting that the crystallinity of coke from each model compound is increasing with the H/C mass ratio. This means that as the structure of coke grows

and becomes more condensed (more aromatic rings, lower H/C ratio), more defects appear in the structure, leading to relatively disordered coke.

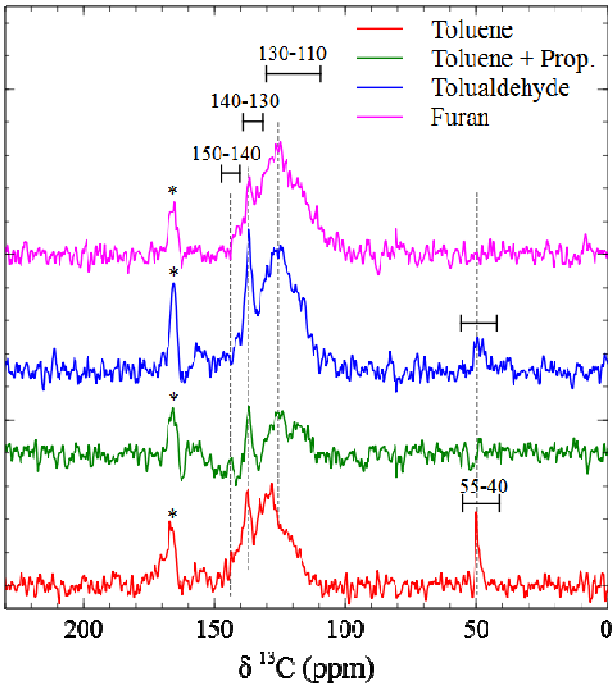

Figure 6-11: NMR analyses of coked zeolites from catalytic pyrolysis of toluene, toluene/propylene, tolualdehyde and furan using ZSM-5 zeolite at 600 °C, 1:1 zeolite to feed ratios.

"*" represents the spinning side bands; 110-130 ppm represents non-substituted aromatic carbon; 130-140 represents carbon bridges between aromatic rings; 140-150 ppm represents substituted aromatic carbon; 55-40 ppm represents aliphatic carbon

In order to explore and understand the most dominant bond types in the coke from the four model compounds, DRIFTS analysis was performed, shown in Figure 6-10. In the region 3100-2900 cm^{-1}, clear peaks are observed in the coke from pyrolysis of toluene and tolualdehyde, meaning that the coke from these two model compounds contains significant amounts of alkyl groups as side chains on the aromatic rings compared with coke from toluene plus propylene and furan. The presence of alkyl side chains in coke from pyrolysis of toluene and tolualdehyde are likely to be reason for the higher H/C ratio and lower temperature TPO peak of the coke. Coke from toluene

with propylene does not contain alkyl groups as aromatic side chains, due to the enhancement of alkylation and cyclization reactions caused by the excessive existence of propylene and ethylene, shown in Figure 6-1. Coke from furan does not contain alkyl groups as side chains. This is consistent with Cheng and Huber,[18] who suggested that there were no terminal methyl or methylene groups at 600 °C in the coke from catalytic pyrolysis of furan, due to the formation of olefins or other products from the methyl group. In the range 1700-1500 cm^{-1}, the coke samples from all the model compounds show peaks, characteristic of aromatic rings, although the peak for toluene coke is weak compared to others. This means that the polyaromatic bone structure of coke is controlled by the ZSM-5 zeolite, whereas the side chains are model-compound-dependent.

Table 6-4: Quantitative NMR analyses of coke from catalytic pyrolysis of different model compounds (1:1 zeolite to feed ratio)*

Location (ppm)	Aliphatic carbon 45-55	Non-substituted aromatic carbon 110-130	Carbon bridges between aromatic rings 130-140	Substituted aromatic carbon 140-150	Aromaticity
Toluene	7.58	45.57	37.35	9.50	92
Toluene/prop	-	85.77	14.23	-	100
Tolualdehyde	6.30	79.58	7.98	6.15	94
Furan	-	71.38	28.62	-	100

*All values reported for aliphatic, non-substituted aromatic and alkyl-substituted aromatic are area percentages of the total spectra. Aromaticity means the total aromatic area percentage of the total spectra area.

Table 6-5: Elemental analysis and ^{13}C NMR analyses of model compounds predicted by Marvin*

	Pyrene	1-Methylpyrene	1-Ethylpyrene	A***	B***
	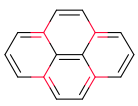	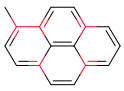	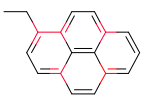	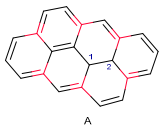	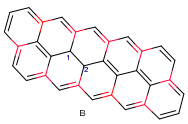
MPD** (nm)	9.22	10.32	9.48	10.04	10.08
H/C mass ratio	0.052	0.059	0.065	0.053	0.051
NMR Aromatic carbon (ppm)	130.90 127.00	132.11 131.45	140.20 130.93	140.23 138.81	148.07 148.07

	125.83	130.97	130.12	138.76	145.56
	124.70	129.73	130.06	135.17	143.98
	124.63	129.15	129.21	132.16	133.27
		127.75	127.79	131.47	131.47
		127.52	127.52	131.06	131.07
		127.02	127.43	130.23	130.78
		126.35	127.03	129.48	129.72
		125.83	125.83	128.95	128.95
		125.05	125.05	128.79	127.41
		124.94	124.94	127.41	127.30
		124.86	124.85	127.12	127.27
		124.82	124.70	127.10	127.12
		124.59	124.25	126.75	127.10
		123.57	123.53	126.48	126.75
				124.91	126.75
				123.22	126.70
				121.61	126.31
				121.19	125.70
					125.03
					124.80
					124.25
					123.62
					123.49
					123.14
					122.74
					122.69
					122.02
					120.36
					120.21
					113.63
Aliphatic carbon (ppm)	-	19.63	25.85	46.60	47.98
			15.00	45.79	47.13

*The carbons in red represent the so-called "bridge carbon".
**MPD represents minimum projection diameter, which is predicted by Marvin.
***A:hexacyclo[11.7.1.1^{4},^{20}.0^{2},^{11}.0^{3},^{8}.0^{17},^{21}]docosa-2,4,6,8,10,12,14,16,18,20(22)-decaene
B:decacyclo[14.14.2.1^{4},^{30}.1^{15},^{19}.0^{2},^{11}.0^{3},^{8}.0^{13},^{31}.0^{17},^{26}.0^{18},^{23}.0^{28},^{32}]tetratriaconta-1(31),2,4(33),5,7,9,11,13,15(34),17,19,21,23,25,27,29-hexadecaene borane

In table 6-4, NMR peak areas for the functional groups of coked zeolites from pyrolysis of all the model compounds are compared quantitatively. Furan and toluene/propylene produce coke with 100% aromaticity (pure PAHs structure), whereas coke from toluene has aliphatic carbons substituted on the aromatic rings. It is interesting and important to understand what kind of aliphatic carbon exists in the toluene coke. In order to further understand the NMR results, the elemental analysis and ^{13}C NMR of various PAHs are predicted using ChemAxon Marvin. In this study, pyrene (MPD 9.22 Å) is used as the starting model compound since its accommodation in ZSM-5 channels has been proven in the literature.[159,160] Table 6-5 shows the elemental analysis,

minimum projection diameter, and NMR peak shift of pyrene and pyrene-derived model compounds. Pyrene does not contain aliphatic carbons. As the alkyl side chain becomes longer (from methyl group to ethyl group), the NMR peak shift goes from 19.63 ppm to 25.85 ppm. The change here is significant. However, the alkyl side chain cannot extend any longer (e.g. propyl group) in order to reach a ~ 50 ppm NMR peak shift, because it would have been easier to form rings (Mechanism R1E) or be cracked to alkanes/alkenes in the presence of zeolite.[161] Thus, further exploration is focused on the alkyl carbon within the ring.

In Table 6-5, compound A (noted here as A for brevity) is the product with alkyl carbon (sp^3 hybridization) in the ring system, shown in red color. The aliphatic peak shift in the NMR of compound A is very close to the real experimental value (45-55 ppm). The accommodation of methylpyrene (MPD 10.32 Å) in ZSM-5 pore system has been proven in the literature.[159,160] Thus, with a smaller MPD (10.04 Å) than methylpyene, compound A can tightly fit inside ZSM-5 cages (7 Å). It should be noted that further growth of compound A in order to reach a more condensed structure (smaller H/C mass ratio) is unlikely due to the shape selectivity theory.[56,97,162–164] Thus, this study proposes a linear growth of compound A to represent coke components with more condensed structures. The linear polyaromatic hydrocarbons have been found to sterically fit inside ZSM-5 pore systems. Palumbo et al.[165] studied the conversion of methanol to hydrocarbons over ZSM-5. They found that, during the reaction, PAHs, such as pentacene (MPD 7.78 Å), can be trapped inside the ZSM-5 channels. Similarly, the tight fit of tetracene (MPD 9.3 Å) in ZSM-5 channels has been proven by Marquis et al.[166] In Table 6-5, compound B shows a more condensed form (smaller H/C mass ratio) than compound A. It is clear that when compound B (MPD 10.08 Å) is used to represent coke, the aliphatic NMR peak shift drops exactly in the range of 45-55 ppm. This implies that the aliphatic carbon in coke observed in NMR and FTIR should have the same feature as that in compound B. The aliphatic carbons exist mainly in the form of cyclic alkane fused within aromatic rings in the final structure of coke produced from pyrolysis of

toluene and tolualdehyde at 600 °C and 1:1 zeolite to feed ratio. However, The H/C mass ratio of the model compounds shown here are between 0.05 and 0.07, lower than that measured from elemental analyses of toluene coke (0.11-0.15). Thus it should be noted that the model compounds A and B can possibly be compounds in the coke mixture (part of coke), but cannot fully represent the whole structure of coke.

6.3.6.Difference in coke formation between ZSM-5 zeolite and ZSM-5 supported catalyst

Figure 6-12 compares product yields, especially coke yields, from the catalytic pyrolysis of toluene, toluene with propylene, tolualdehyde, and furan using ZSM-5 zeolite and ZSM-5 catalyst. For all the model compounds studied, ZSM-5 zeolite promotes the conversion of the feed, leading to higher coke yields. In the case of tolualdehyde, when conversion is 100% in both ZSM-5 zeolite and catalyst, the ZSM-5 zeolite enhances coke formation due to higher active site density. For comparison of the structure of coke produced over ZSM-5 zeolite and catalyst, TPO was performed for each coke. Figure 6-13 shows TPO analyses of coke/char from catalytic pyrolysis of toluene, propylene, toluene with propylene and tolualdehyde using (a) ZSM-5 zeolite and (b) ZSM-5 catalyst. Consistently, when ZSM-5 zeolite is used, the single peak of the first derivative of weight loss is shown at a temperature of about 620 °C, which means that in the catalytic pyrolysis of these model compounds, only coke is formed.[65] Interestingly, when ZSM-5 catalyst is used, a peak shift is observed for all the model compounds studied. To be specific, for the catalytic pyrolysis of toluene, the peak shifts to higher temperature as the catalyst to feed ratio increases. For the catalytic pyrolysis of toluene with propylene cofeeding and catalytic pyrolysis of tolualdehyde, the peak shifts to lower temperature as the catalyst to feed ratio increases. The shift of the peak to lower temperature means lower activation energy in the combustion of coke from higher catalyst to feed ratio.[123] A similar peak shift is also observed when different heating rates are used during combustion.[65] Previously, catalyst support was shown to have uncontrolled activity for coke/char formation during biomass catalytic pyrolysis.[61] Therefore, the peak shift

can be explained by the formation of carbonaceous materials of different structure on the catalyst support. Another reason that can result in the shift of the TPO peak temperature in combustion is the diffusion limitation of the oxygen component caused by the catalyst support. Finnouche et al.[167] studied desorption of xylene isomers with TGA. A relatively lower temperature for desorption of p-xylene was observed compared with o- and m-xylenes. The peak from TPO of coked catalyst from furan does not shift much as the catalyst to feed ratio changes. However, for catalytic pyrolysis of furan, the TPOs of coked catalysts show a secondary peak at relatively high temperature, which indicates that a more condensed coke is formed in pyrolysis of furan compared with that formed in pyrolysis of other model compounds. This claim is very consistent with the coke formation pathway through furan self-condensation (Scheme 6-3, RB).

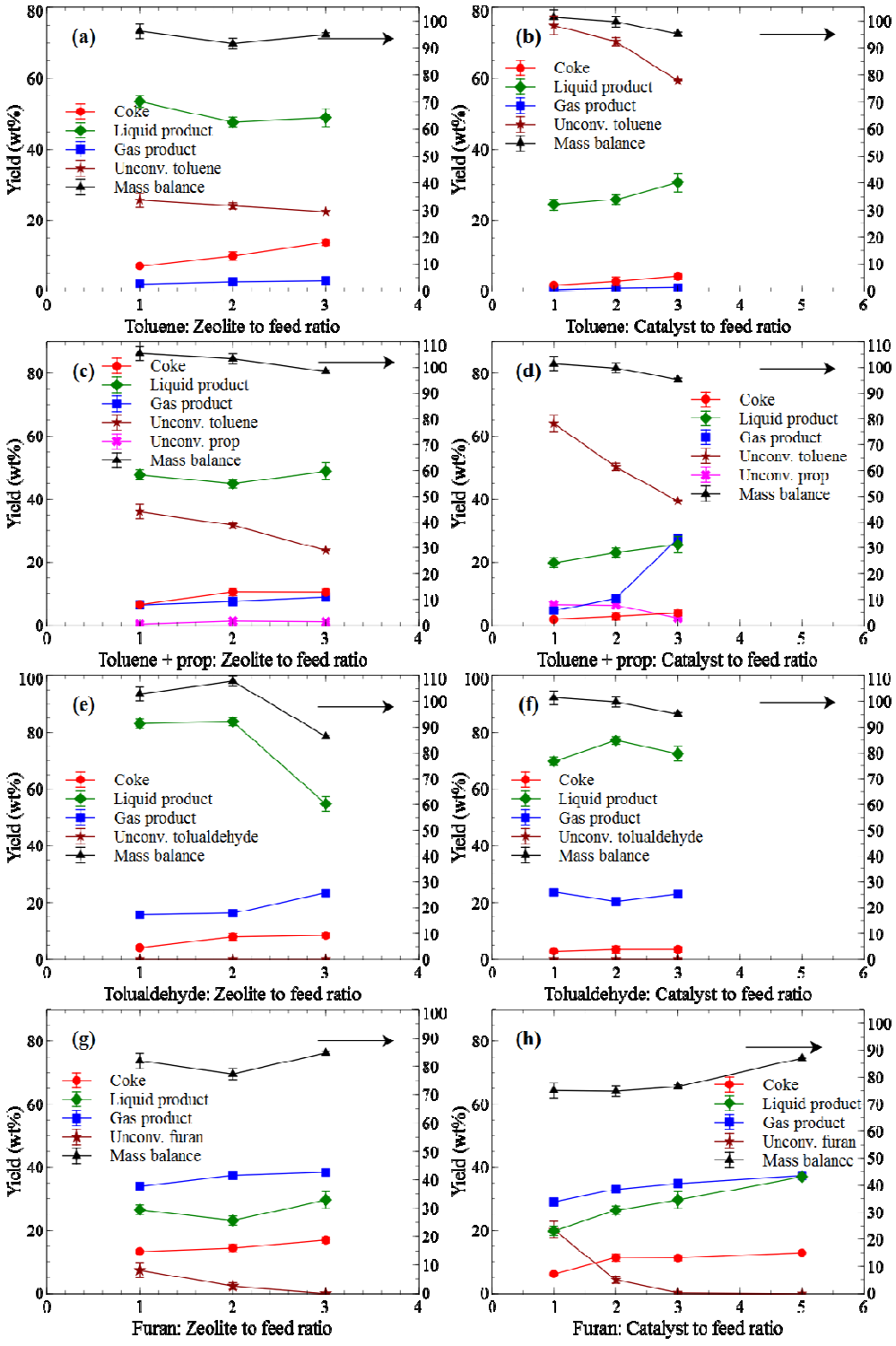

Figure 6-12: Product yields from catalytic pyrolysis of toluene, toluene with propylene, tolualdehyde, and furan using (a, c, e, g) ZSM-5 zeolite and (b, d, f, h) ZSM-5 catalyst

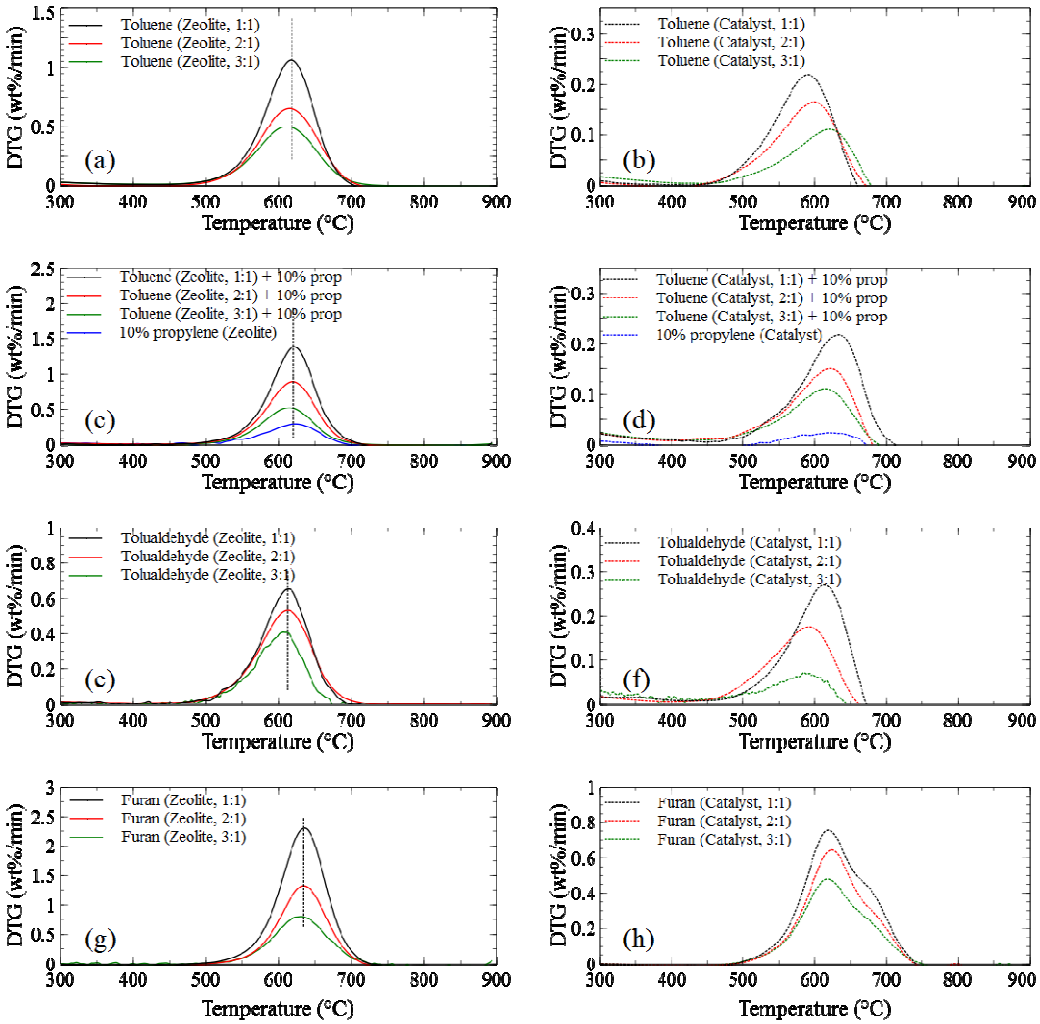

Figure 6-13: TGA analyses of coked zeolites and catalysts from catalytic pyrolysis of toluene, propylene, toluene with propylene and tolualdehyde using (a, c, e, g) ZSM-5 zeolite and (b, d, f, h) ZSM-5 catalyst

6.4. Conclusions

In summary, reaction pathways for coke formation have been studied in catalytic pyrolysis of toluene, toluene/propylene, tolualdehyde and furan over ZSM-5 zeolites and ZSM-5 supported catalyst. The structure of coke from different model compounds has been explored and compared to each other. From the experimental results and corresponding discussion, the following main conclusions were drawn:

- In toluene catalytic pyrolysis, coke formation follows alkylation reaction pathways. Biphenyls, bibenzyl and heavy PAHs are important reaction intermediates leading to coke formation. The cofeeding of propylene with toluene does not enhance coke formation compared with pure toluene during the catalytic pyrolysis. Propylene mostly forms toluene/benzene as the primary step and follows the alkylation reactions of toluene/benzene afterwards.
- In catalytic pyrolysis of tolualdehyde (used as a representative aromatic oxygenate), decarbonylation was shown as the initial step during the pyrolysis. The formation of coke follows exactly the same path as the coke formation in catalytic pyrolysis of toluene. Aldol condensation of the carbonyl group in tolualdehyde with acetone is not seen to occur at pyrolysis conditions. In catalytic pyrolysis of furan, Diels-Alder reactions for production of olefins and aromatic hydrocarbons are the dominant reactions in the catalytic pyrolysis. The aromatic hydrocarbons and olefins in the "hydrocarbon pool" are proposed as coke precursors leading to formation of coke with no oxygen content. From the results of tolualdehyde and furan, it was shown that oxygen is not participating in the coke formation mechanism directly.
- The production of coke is more affected by zeolite/catalyst to feed ratio than by the model compounds, reflecting the catalytic origin of the coke and its limited precursors. Among all the model compounds in this study, furan contributes the most to coke formation compared with the other model compounds.
- The structure of coke is similar between toluene and tolualdehyde, which is consistent with the proposed mechanisms. Among the model compounds, furan has the most condensed form of coke after catalytic pyrolysis. In tolualdehyde and toluene, coke contains significant amount of aliphatic carbons in the aromatic ring system whereas no aliphatic carbon is observed in coke from toluene/propylene cofeeding and furan.

Moreover, catalytic reactions enhance the production of coke with greater crystallinity, less condensed structure and higher H/C mass ratio.

- When using a supported catalyst, coke formation is reduced compared with using zeolite, due to the acid sites being diluted in the support. The lower acidity of the supported ZSM-5 promotes the cracking reaction of benzofuran, resulting in more condensed coke with higher TPO peak temperature.

CHAPTER 7 SUGGESTED FUTURE WORK

7.1. Further study of aldol condensation reactions leading to coke and char formation

Aldol condensation reaction has been considered important in the fundamental studies of char formation in biomass pyrolysis.[105] The studies in Chapter 6 showed that tolualdehyde, an aromatic compound with aldehyde group, performed decarbonylation reaction forming toluene and CO as the initiation reaction during catalytic pyrolysis at 600 °C with ZSM-5. This resulted in very low possibility for tolualdehyde, even at the presence of acetone, to undergo aldol condensation reactions. Another well-known reaction of aldol condensation comes from furfural and acetone. Several studies have been performed regarding furfural and acetone aldol condensation. Kikhtyanin et al.[168,169] studied the aldol condensation of furfural and acetone at 20-100 °C using zeolites. They found that the product distribution was affected by the acidity of zeolites. For example, 4-(2-furyl)-3-butene-2-on was the major product in the aldol condensation when MFI zeolite was used. Coke was also observed. The TPO of the coked zeolite showed a peak at around 380 °C. The results reported by Kikhtyanin et al. are in good agreement with the results from Hora et al.,[41] who studied aldol condensation of furfural and acetone over Mg-Al catalysts. However, at common pyrolysis temperatures (400-600 °C), the reaction of aldol condensation between furfural and acetone might not dominate compared with the pyrolysis of each of them alone. In this case, the effect of synergy between furfural and acetone on coke and char formation at high temperature (400-600 °C) is of significant interest. Fanchiang and Lin[170] studied catalytic pyrolysis of furfural over ZSM-5 at 300-500 °C. They concluded that the initiation of furfural conversion was decarbonylation, which produced furan and CO as the products. Cheng and Huber[51] studied catalytic pyrolysis of furan, furfural and furfuryl alcohol and their cofeeding with propylene over ZSM-5 at 400-600 °C. They concluded that even at the existence of propylene, conversion of furfural into furan and CO inside the catalyst was the first step in catalytic pyrolysis. The production of aromatics in pyrolysis of furfural followed the Diels

Alder reactions similar to that from furan. These two examples imply that in furfural, the aldehyde group on furan ring is very easy to break during the catalytic pyrolysis, just like that in tolualdehyde.

The proof of aldol condensation of furfural and acetone at high temperature (400-600 °C) over ZSM-5 is absent in the literature to the best of our knowledge. Thus it will be very interesting to investigate the synergy between furfural and acetone experimentally. By combining the liquid analysis and char/coke characterization, as performed in Chapter 6, the real effect of aldol condensation on the char/coke formation can be revealed. For future work, it is suggested that experiments of catalytic pyrolysis of furfural, acetone and furfural cofeeding with acetone should be performed under regular pyrolysis temperatures (400-600 °C) over ZSM-5. The comparison of the three parallel experiments should be focused on the liquid product distribution, the char/coke yields, char/coke deposition location, structure, functional groups and composition. Besides furfural, another aldehyde compound, acetaldehyde has already been studied regarding its capability to undergo aldol condensation with itself. However, that study was not performed under common pyrolysis conditions, either.[52] It will be better to also include acetaldehyde in the study of coke/char formation through aldol condensation reactions during catalytic pyrolysis. The preliminary results from tolualdehyde (Chapter 6), furfural and acetaldehyde provide a strong mechanistic insight, as a starting point in understanding coke formation due to aldol condensation.

7.2. Understanding the decoupled effect of pore size and acidity on coke formation

Coke formation during biomass catalytic pyrolysis, at least when the studied model compounds are used (Chapter 6), has been proven to follow the “hydrocarbon pool” mechanism. This means that favorable single-ring aromatic hydrocarbons are formed together with the poly-aromatic hydrocarbons, which are unfavorable coke precursors. In other words, the current widely-used

zeolite catalysis system will always create a compromise between the promotion of formation of single-ring aromatic hydrocarbons and decrease of formation of coke. Recently, studies[17,56,171,172] have been focused on the design and synthesis of novel zeolite catalysts with unique properties, such as pore size and acidity, in order to find an effective way for coke reduction.

Investigations regarding the effect of pore size and zeolite acidity on coke formation and liquid aromatics production have been performed in the literature. Jae et al.[56] found that medium pore zeolites with moderate internal pore space and steric hindrance (ZSM-5 and ZSM-11) have the highest aromatic yield and the least amount of coke. Theoretically, smaller pore size zeolites can effectively prevent coke formation. However, as they observed, for example, SAPO-34, whose pore size is smaller than that of ZSM-5, could not form either coke or liquid aromatics. In contrast, the biggest pore size zeolite, Y zeolite, formed the maximum quantity of coke in carbon yield, due to either the bigger pore size or the higher acidity, which is another reason for enhanced coke formation. Mukarakate et al.[171] studied the role of SiO_2/Al_2O_3 in product distribution during upgrading of biomass pyrolysis vapors over β-zeolite. They observed that higher acidity zeolite (lower SiO_2/Al_2O_3) produced more coke in yield, regardless of the pore size of the zeolite.

Mesoporous zeolites have been widely used for the study of biomass catalytic pyrolysis, due to the potential capability of relaxing the diffusion limitations of microporous zeolites. A very nice and integrated work comes from Li et al.,[172] who studied catalytic pyrolysis of wood, cellulose and lignin. They found that desilicated ZSM-5 zeolite, which has mesoporous structure, would enhance the production of aromatics and reduce coke formation. This is a very interesting observation, because it implies that coke formation can be prevented to some extent by decreasing the residence time inside the zeolite system, further reducing the chance of secondary reactions inside zeolite. Unfortunately, there was no strong proof of the relaxation of coke formation due to mesoporosity in zeolite. As a result, the reason for the reduction of coke

formation was attributed to the creation of mesoporosity without noticing another potential reason of the significantly decreased Brønsted acidity. The uncertainty in the effect of zeolite acidity can generate a misunderstanding of the effect of catalyst porosity on coke formation. As an example, Foster et al.,[17] observed an opposite effect of mesoporosity on the coke formation compared with Li et al.[172] They created the hierarchical mesoporosity in ZSM-5 with an increased bulk SiO_2/Al_2O_3 ratio using the surfactant-mediated method. They found that when furan was used as the feedstock, the mesoporous ZSM-5 produced much more coke in yield compared with the parent ZSM-5. They attributed the reason for the increased coke yield to the contribution of mesopores making more space for coke to accommodate. Combining the results from Li et al.[172] and Foster et al.,[17] it is obvious that the inconsistent conclusions regarding the relationship between coke formation and mesoporosity is caused by their ignoring the effect of the zeolite acidity (SiO_2/Al_2O_3 ratio) on coke formation. From these two studies, it seems that the real reason affecting the coke formation is the acidity of the zeolite rather than pore size.

In the literature, the difficulty of discriminating between the effect of the pore structure (mostly pore size) and that of acidity on the coking rate has been pointed out by Guisnet and Magnoux.[173] Moreover, the decoupled effect of mesoporosity and acidity is, to some degree, distinguished by Kim et al.,[174] who studied the effect of mesoporosity on coke formation during methanol-to-hydrocarbon (MTH) conversion. They concluded that coke formation could be relaxed by combining the introduction of mesoporosity and a low concentration of acid sites in the zeolite. It is suggested that preliminary work should focus on the true effect (without interaction of acidity) of hierarchical mesoporous zeolite on the coke formation during biomass catalytic pyrolysis. An effective method for synthesis of mesoporous materials without significantly changing SiO_2/Al_2O_3 ratio should be investigated, based on which a better understanding of the decoupled effect of pore size and acidity on product distribution, especially coke formation, can be gained.

CHAPTER 8 CONCLUSIONS

The proposed spouted bed design was shown to be a promising reaction system for biomass catalytic pyrolysis, providing excellent mixing, superior biomass feeding and selectivity towards deoxygenated products. In agreement with relevant literature reports, high temperatures and catalyst loadings favored aromatics production, via deoxygenation reactions that formed carbon oxides. The catalyst support produced more coke and less monocyclic aromatic hydrocarbons than the ZSM-5 catalyst, due to its uncontrolled catalytic activity and lack of shape selectivity. The reactor operating conditions were mapped to product selectivity showing high selectivity to aromatics at 600 °C and high catalyst to biomass ratios.

The quantitative product distribution is not the same between the spouted bed reactor and the Py-GC apparatus due to different operating conditions (heating rate and residence time). The higher heating rate and residence time in the spouted bed lead to higher gas yield, lower liquid yield and promoted aromatic hydrocarbons production compared with *in situ* CFP in PyGC. *Ex situ* catalytic upgrading enhanced production of deoxygenated compounds, compared with the *in situ* CFP, due to the prevention of catalyst deactivation caused by char formation. The structure of char from the CFP method is different from that of thermal pyrolysis, resulting in the notion that the catalyst has an effect on the structure of thermal char. The TPO of char/coke from *in situ* CFP and that from spouted bed show peaks at the exact same temperature, indicating that different residence times and heating rates between the two configurations do not affect the char/coke structure.

The properties and the characteristics of the char and coke derived from thermal and catalytic pyrolysis are different. The formation of char and coke strongly depends on the biomass source and also on the pyrolysis conditions (e.g., heating rates). When glucose and pine are used as biomass feed in slow catalytic pyrolysis, catalyst deactivation due to formation of char and the

corresponding loss of accessibility (surface coverage and macropore blocking) becomes dominant. On the other hand, in cellulose slow catalytic pyrolysis and all the Catalytic fast pyrolysis experiments, the formation of coke is attributed to catalyst micropore blocking. In Catalytic fast pyrolysis of glucose and pine, formation of catalytic coke proceeds in parallel to the formation of thermal char. We identified the char to coke ratio to be 3/7 (mass basis) for the case of glucose and it is theoretically feasible to do so for other biomass model compounds.

The formation of coke from olefins, aromatic hydrocarbons and aromatic oxygenates are all directly related to the so-called "hydrocarbon pool" mechanism, following mainly hydrogen transfer and cyclization reactions. The structure of coke is similar between toluene and tolualdehyde, which are consistent with the proposed mechanisms. Among the model compounds studied, furan has the most condensed form of coke after catalytic pyrolysis. In tolualdehyde and toluene, coke contains significant amounts of aliphatic carbons in the aromatic ring system whereas no aliphatic carbon is observed in coke from toluene/propylene cofeeding and furan. Moreover, catalytic reactions enhance the production of coke with greater crystallinity, less condensed structure and higher H/C mass ratio. When using a supported catalyst, the coke formation is reduced compared with using zeolite, due to the diluted acid sites caused by the support. The lower acidity of the supported ZSM-5 promotes the cracking reaction of benzofuran, resulting in more condensed coke with higher TPO peak temperature.

It is suggested that future work should focus on further investigating the effect of aldol condensation during char/coke formation using model compounds, such as furfural and acetaldehyde. Besides understanding of the char/coke formation during biomass catalytic pyrolysis, an exploration of the decoupled effect of pore size and acidity on product distribution, especially coke formation, should also be performed. This will contribute greatly to the final goal of designing and synthesizing novel catalysts that can reduce coke formation and enhance biooil production.

APPENDIX I CONVERSION OF WASTE BIOSOLID FROM WATER TREATMENT PLANT TO FUELS AND CHEMICALS

The results of Appendix I have been published in Applied Energy, 2014.[175]

Brown grease is a mixture of high-value hydrocarbons, such as waste vegetable oil, animal fats and grease that is collected in water treatment plants and requires further treatment before disposal. However, brown grease has a higher level of contamination, compared to yellow grease, and cannot be used as animal feedstock or fertilizer. Additionally, brown grease is responsible for about 40% of all sewer overflows, causing back-ups and damage to pipe lines and for about 20,000,000 illnesses each year in the USA.[176] Therefore, special attention must be dedicated to its disposal and the cost associated. In order to fulfill 100% utilization of the brown grease for fuel and chemicals production, the main goal of this project is to explore the possibility of converting the 10 wt% heavy product (bio-solid in aqueous phase) after phase separation in the process of bio-diesel production to useful fuels and chemicals. The concept of utilizing brown grease bio-solids in pyrolysis and gasification was driven by the comparison of the hydrogen-to-carbon and oxygen-to-carbon ratios, as well as the hydrogen-to-carbon effective ratio (Table I-1), with those of lignocellulosic biomass (pine sawdust) and glucose, a biomass model compound.

Table I-1: Elemental analysis of bio-solid, pine and glucose (mol%, dry basis)

Feedstock	N	C	H	O*	H/C	O/C	H/C_{eff}
Bio-solid	1.19	33.80	54.64	10.37	1.62	0.31	1.00
Pine	0.20	34.52	46.33	18.95	1.34	0.55	0.25
Glucose	0.00	25.00	50.00	25.00	2.00	1.00	0.00

* Oxygen content was calculated by difference.

The elemental analysis (H/C, O/C and H/C_{eff} in Table I-1) shows that the brown grease bio-solids compose a hydrogen rich feedstock, which implies its potential for pyrolysis and gasification. The feasibility of pyrolyzing feedstocks of high H/C_{eff} ratios, such as brown grease bio-solids, was articulated by Zhang et al.,[177] where the aromatic and olefin yield (desired pyrolysis products) as a function of H/C_{eff} was studied. They found that increasing H/C_{eff} ratio (from 0 – glucose to 2 – methanol) results in increasing the aromatic and olefin yields (from 27 C% to 80 C%, respectively). Moreover, there is an inflection point at H/C_{eff} ratio of 1.2, after which the aromatic and olefin yield does not increase rapidly. As shown in Table I-1, all the biomasses analyzed in this study have the H/C_{eff} less than 1.2, which means the aromatic and olefin yield will change significantly among these feedstocks as the hydrogen to carbon effective ratio varies. The brown grease bio-solid has a much greater H/C_{eff} than pine and glucose, which implies its potential to producing higher aromatic and olefin yields via pyrolysis.

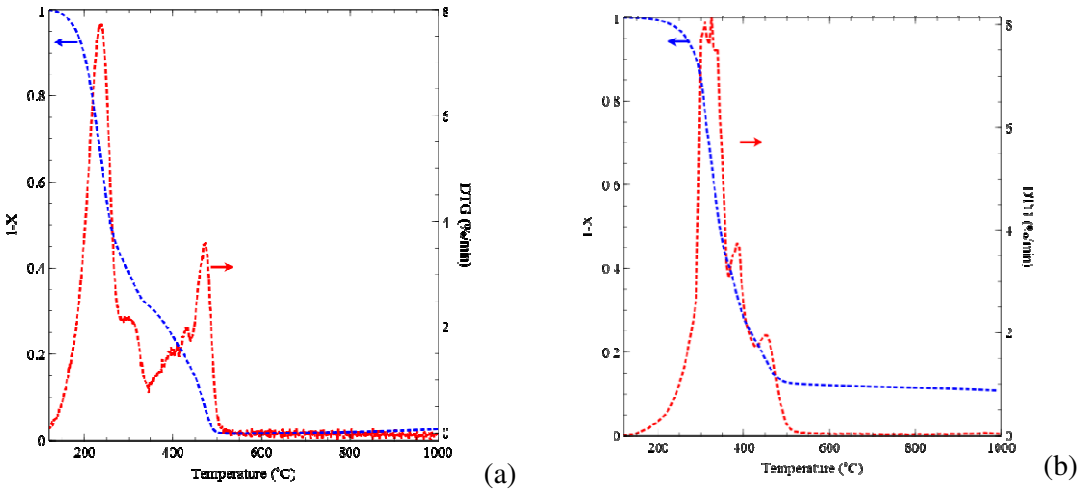

Figure I-1: Thermogravimetric analysis (TGA) of biosolid in (a) air and (b) nitrogen

Bio-solids gasification (combustion) was performed in thermogravimetric analysis (TGA) in air, to explore the extent of gasifiability of the bio-solids, whereas pyrolysis was studied in both TGA and in a fixed bed reactor. The selectivity of pyrolysis liquid products was investigated using Gas

chromatography-mass spectrometer (GC-MS). As shown in Figure I-1, gasification and pyrolysis of the brown grease bio-solids were performed in (a) air and (b) nitrogen, respectively, in TGA at 10 °C/min to 900 °C. Each experiment was held at 120 °C for 30 min to remove moisture in the sample. In Figure I-1(a), multiple peaks appear in the DTG analysis of the combustion of bio-solids, with the first in the 200-400 °C range and the second in the 400-500 °C range. By comparing the combustion (Figure I-1(a)) and pyrolysis (Figure I-1(b)) experiments, the first DTG peak is attributed to thermal decomposition of the bio-solids and the second DTG peak represents the oxidation of bio-solid chars.[178] As shown in the pyrolysis TGA experiment, about 10 wt% char residue left after the pyrolysis. In the combustion experiment less than 1 wt% residue remained in the TGA crucible. This result indicates that about 9 wt% of the total residue after (slow) pyrolysis is char, which cannot be further pyrolyzed in inert gas atmosphere, but it is combustible. The 1 wt% residue after combustion should include mostly inorganic compounds (ash). Further analysis of the residue and its environmental impact will be discussed in the future. The above analysis proves that almost the entirety (99 wt%) of the bio-solids is combustible, which also implies the feasibility of producing synthesis gas from the bio-solid through gasification.

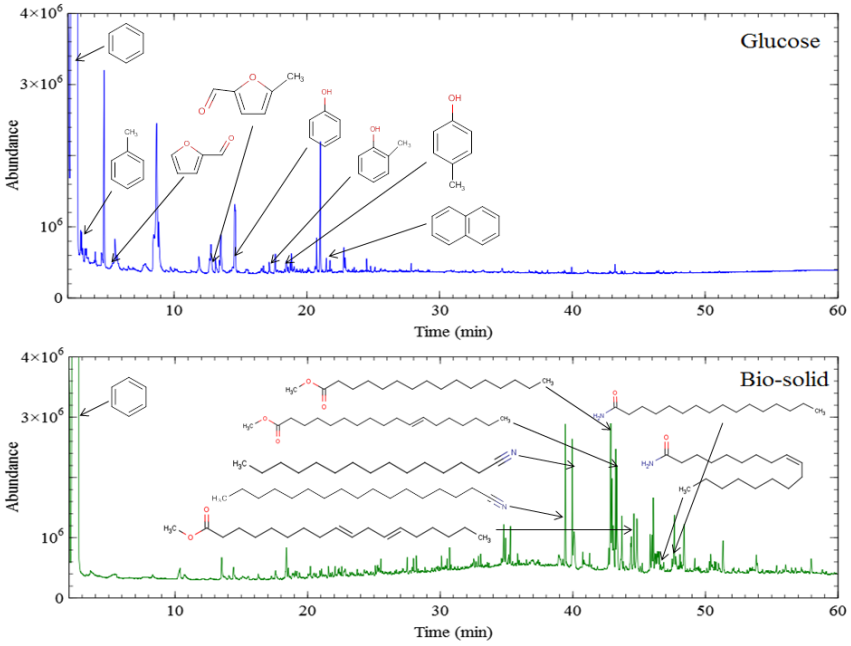

Figure I-2: Identification of the major compounds from GC-MS analysis of bio-oils produced from glucose and bio-solid

Production of bio-oil from the bio-solid was studied through fast pyrolysis in a quartz reactor heated by a drop tube furnace at 600 °C. The fast heating rate was accomplished by sliding the pyrolysis reactor into the hot zone of the furnace. The liquid products were collected using two impingers (1st empty, 2nd with 10 ml methanol) in dry-ice bath. The liquid product selectivity was investigated in Gas Chromatography-Mass Spectrometer (GC-MS). The GC-MS method used for the analysis involves holding the sample at temperature 40 °C for 10 min and then increasing the oven temperature to 280 °C at a rate of 5 °C/min. Before the GC-MS analysis, the sample was washed and diluted with methanol. As shown in Figure I-2, the liquid products of pyrolysis of bio-solids are mostly long-chain hydrocarbons. As a comparison, the liquid products from the fast pyrolysis of glucose (a lignocellulosic biomass model compound) at 600 °C are also listed in Figure I-2, and contain many small oxygenates, such as furan compounds. Production of oxygenates from pyrolysis of lignocellulosic biomass is often reported in the literature.[55,58,119,179,180] In that respect, pyrolysis of bio-solids is advantageous as compared to other commonly studied biomass sources.

APPENDIX II CONVERSION OF WASTE COFFEE GROUNDS TO FUELS AND CHEMICALS

The results of Appendix II have been published in RSC Advances, 2015.[181]

In 2013, 2.8 million metric tons of coffee waste were produced by countries who import coffee.[182] The typical way for treatment of spent coffee grounds (SCG) is to dispose in landfills. However, this can take up large amounts of space. What's worse, the disposed SCG can become a source of methane emissions as a result of anaerobic decomposition,[183] which will intensify global warming. Falling into the general category of waste biomass, SCG is a renewable resource that has the potential to assist with energy generation and chemicals production.[58] In this study, thermal and catalytic pyrolysis of SCG is investigated to explore the potential utilization of SCG for fuels and useful chemicals production. The effect of temperature and ZSM-5 catalyst on product distribution is discussed.

Thermal and catalytic pyrolysis of SCG was performed in a fixed-bed reactor. 1.0 gr of SCG and 1.0 gr of ZSM-5 (in catalytic experiments) were loaded into the reactor between the quartz wool layers. Prior to pyrolysis, the reactor was heated to 490-590 °C in an inert Ar environment with a 100 sccm purge. An impinger was filled with acetone and submerged in a dry ice bath for condensing the liquid products. A 1 L gas collection bag was used for gas collection and off-line gas analysis in gas chromatograph with a thermal conductivity detector (GC-TCD). During the preheating stage, the reactor was elevated outside the furnace to avoid premature pyrolysis. To initiate pyrolysis, the bed was rapidly shifted into the center of the hot furnace. The liquid product was analyzed via gas chromatography mass spectrometry (GC-MS) off-line after pyrolysis.

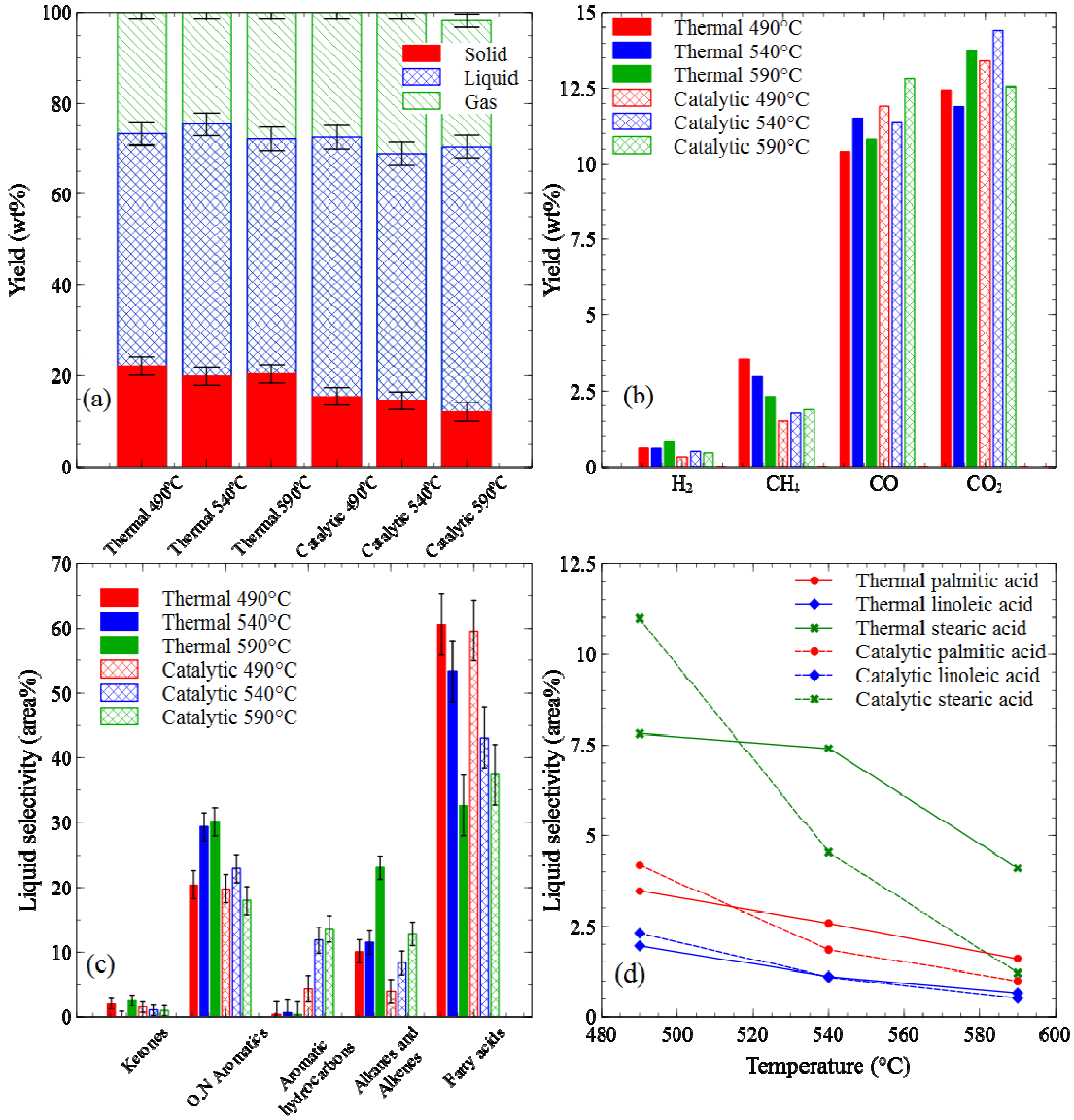

Figure II-1: Catalytic pyrolysis of SCG in fixed-bed reactor. (a) Lumped product distribution; (b) Gas yields; (c) Liquid product selectivity by area percent (d) Acid product selectivity by area percent.

The pyrolysis of SCG in the fixed-bed reactor produces a liquid product consisting of furans, phenols, aromatics, linear hydrocarbons, caffeine, fatty acids, nitriles, amides, among other compounds, with a total liquid yield of 0.51-0.58 wt% (Figure II-1(a)). The gas yields from the pyrolysis of SCG in fixed-bed are shown in Figure II-1(b). The yield of CO from the thermal pyrolysis of SCG is 10.5-12 wt%. The yield of CO from the catalytic pyrolysis of SCG is 11.5-13

wt%, which increases by 1 wt% from thermal pyrolysis. Char yields from the pyrolysis of SCG are measured to be 15-20 wt%.

For illustration purposes, the liquid products are categorized in functional groups as ketones, oxygenated and nitrogenated aromatics, aromatics, alkenes and alkanes, and fatty acids. The relative abundance of aromatics, alkenes, and alkanes increases with temperature in both thermal and catalytic experiments (figure II-1(c)), while the selectivity of fatty acids (figure II-1(d)) is found to decrease with increasing temperature. In SCG pyrolysis, alkanes and 1-alkenes are formed via decarboxylation and decarbonylation of the saturated fatty acids, palmitic and stearic acid. The decarboxylation of linoleic acid (an unsaturated acid) can produce n-alkenes, yet these are mostly absent from SCG pyrolysis experiments. In addition, the selectivity of stearic acid from both thermal and catalytic pyrolysis of SCG is particularly high (Figure II-1(c)), which indicates that the saturation of linoleic acid to stearic acid via hydrogenation occurs as the first step in pyrolysis and that the chemistry of saturated fatty acids is dominant in SCG pyrolysis. The saturation behavior is confirmed by observations from the pyrolysis of unsaturated fatty acids conducted by Asomaning et al.,[184] who found that the pyrolysis of unsaturated fatty acids had a greater selectivity to 1-alkenes and 1-alkanes rather than n-alkenes.

The decarboxylation of fatty acids to form alkanes and the decarbonylation of fatty acids to form 1-alkenes compete during the pyrolysis of SCG. The selectivity of 1-heptadecene and 1-pentadecene is lower than the selectivity of heptadecane and pentadecane (Table II-1), which suggests that decarboxylation is the primary pathway for fatty acid decomposition.

Table II-1: Fixed-bed liquid product distribution by GC-MS peak area percentage.

Compound	763K Thermal	763K Catalytic	813K Thermal	813K Catalytic	863K Thermal	863K Catalytic
2-5-dimethylfuran	0.67	0.41	-	-	0.75	0.30
toluene	0.37	1.12	-	4.81	0.35	6.11
2-cyclopenten-1-one	0.26	-	-	-	0.49	-
2-furanmethanol	3.20	-	5.95	-	4.28	-
p-xylene	-	1.77	-	3.13	-	4.65
2-hydroxy-2-cyclopenten-1-one	1.95	1.49	-	-	-	-
phenol	2.52	2.98	3.91	4.72	4.29	2.98
3-methyl-1,2-cyclopentendione	1.79	-	-	-	2.05	0.96
2-cyclopenten-1-one	-	1.53	-	1.05	-	-
Indene	-	-	-	1.76	-	0.90
2-methylphenol	-	-	-	1.10	0.95	0.96
4-metyhlphenol	2.04	2.89	3.23	3.77	3.19	2.26
1-undecene	-	-	-	-	0.98	2.39
2,4-dimethylphenol	-	0.99	1.14	1.51	1.20	-
naphthalene	-	1.51	-	2.19	-	1.91
1-dodecene	2.86	-	-	-	2.50	1.32
1,2-benzenediol	1.82	3.71	4.02	2.90	5.16	3.53
hydroquinone	1.95	1.08	2.14	1.73	1.32	2.77
1-methylnaphthalene	-	3.55	-	3.07	-	1.24
1-tridecene	-	-	0.96	-	3.22	-
tridecane	-	-	0.59	-	1.04	1.84
(2-4)-methyl-1H-indole	0.48	0.67	0.63	1.78	0.61	1.34
1-tetradecene	1.54	0.53	1.62	0.85	4.07	1.16
tetradecane	0.71	-	1.09	1.57	1.17	1.05
1-pentadecene	0.52	-	-	-	1.63	0.92
pentadecane	3.19	2.42	4.33	4.02	5.13	3.06
1-hexadecene	-	-	0.59	-	0.90	-
hexadecane	-	-	0.46	-	0.48	-
heptadecane	1.25	1.05	1.89	1.91	1.95	1.09
caffeine	7.70	7.05	8.34	5.42	8.37	3.79
hexadecanenitrile	1.80	3.08	3.17	4.75	3.14	2.97
hexadecanoic acid	40.68	39.63	36.91	28.38	23.06	26.67
heptadecanenitrile	-	-	-	1.78	-	-
9,12-octadecadienoic acid	14.19	13.48	9.84	10.38	5.90	8.70
octadecanoic acid	5.71	6.49	6.60	4.34	3.68	2.02
hexadecanamide	1.32	1.11	2.02	2.03	1.62	1.82

The presence of ZSM-5 catalyst decreases the selectivity to alkenes and alkanes (Figure II-1(c)), indicating that these products are oligomerized to aromatics due to the positive effect of ZSM-5 on aromatics selectivity. The selectivity to O,N aromatics (furans, phenols, indoles, etc.) is substantially higher in thermal experiments compared with the catalytic experiments. The selectivity to aromatic hydrocarbons is substantially greater in catalytic experiments when compared with thermal experiments. The selectivity of aromatic hydrocarbon from catalytic pyrolysis of SCG increases 3-fold when the temperature is increased from 763-863K (Figure II-1(c)).

Table II-2: Elemental analysis of SCG feedstock and biochars from fixed-bed pyrolysis (wt%).

	N	C	H	S	O
SCG Feedstock	1.8	55.6	7.0	0.2	35.5
Char (763K)	2.9	72.0	3.7	0.4	21.1
Char (813K)	3.0	74.8	3.0	0.4	18.9
Char (863K)	2.9	76.2	2.5	0.3	18.8

Elemental analysis of the SCG feedstock and thermal biochars of the SCG pyrolysis experiments are reported in Table II-2. Nitrogen, carbon, and sulfur content are significantly greater in the char samples than in SCG. In contrast, hydrogen and oxygen are dramatically decreased, implying that hydrogen and oxygen sources are more readily pyrolyzed than carbon, nitrogen, and sulfur. Increasing pyrolysis temperature is oberved to increase the carbon content, while decrease the hydrogen and oxygen content in the char. From char analysis it is clear that significant nitrogen content is maintained in the solid form, suggesting fertilizer applications. From an environmental point of view, the retention of nitrogen and sulfur in the solid residue is a clear advantage of SCG pyrolysis as compared to combustion and gasification.

APPENDIX III LIST OF PUBLICATIONS AND CONFERENCE PRESENTATIONS

Publications

- Shoucheng Du, Julia A. Valla, George M. Bollas. Characteristics and origin of char and coke from fast and slow, catalytic and thermal pyrolysis of biomass and relevant model compounds. *Green Chemistry.* 2013, 15, 3214-3229.
- Shoucheng Du, Yijia Sun, David P. Gamliel, Julia A. Valla, George M. Bollas. Catalytic pyrolysis of miscanthus giganteus in a spouted bed reactor using ZSM-5 catalyst. *Bioresource Technology*. 2014, 169, 188–197.
- Iman Noshadi, Baishali Kanjilal, Shoucheng Du, George M. Bollas, Steven L. Suib, Anthony Provatas, Fujian Liu, Richard S. Parnas. Catalyzed production of biodiesel and bio-chemicals from brown grease using Ionic Liquid functionalized ordered mesoporous polymer. *Applied Energy*. 2014, 129, 112-122.
- Shoucheng Du, David P. Gamliel, Julia A. Valla, George M. Bollas. Coke formation of model compounds relevant to pyrolysis bio-oil over ZSM-5. *Green Chemistry.* 2015, submitted.
- Ari Fischer, Shoucheng Du, George M. Bollas. The effect of temperature, heating rate, and ZSM-5 catalyst on the product selectivity of the fast pyrolysis of Spent Coffee Grounds. *RSC Advances*. 2015, 5, 29252-29261.
- David P. Gamliel, Shoucheng Du, Julia A. Valla, George M. Bollas. Biomass catalytic pyrolysis in multiple reactor configurations: a comparison of spouted bed reactor and pyroprobe-GC-MS. *Bioresource Technology*. 2015, submitted.
- Ting Jiang, Shoucheng Du, Tahereh Jafari, Wei Zhong, Yu Sun, Wenqiao Song, Zhu Luo, William A. Hines, Steven L. Suib. Synthesis of highly selective multifunctional Pd/meso-γ-Fe2O3 nanoparticles and their application as magnetically recyclable catalysts in

nitrobenzene hydrogenation under mild reaction conditions. *Applied Catalysis A: General.* 2015, sumbitted.

Conference oral presentations

- Shoucheng Du, David P. Gamliel, Julia Valla and George M. Bollas. Catalytic Pyrolysis of Char and Coke Precursors: An Investigation of the Formation Mechanisms of Char and Coke. AICHE Annual Meeting, November 2014, Atlanta, GA, USA.
- Ari Fischer, Shoucheng Du and George M. Bollas. Conversion of Caffeine and Lipids in Catalytic Fast-Pyrolysis of Spent Coffee Grounds. AICHE Annual Meeting, November 2014, Atlanta, GA, USA.
- David P. Gamliel, Shoucheng Du, George M. Bollas and Julia Valla. A Fundamental Study of the Reaction and Diffusion of Poly-Aromatic Hydrocarbons in Hierarchical Pore Structure Zeolites. AICHE Annual Meeting, November 2014, Atlanta, GA, USA.
- D.Gamliel, M. Dahl, S. Du, G. M Bollas, J. Valla, "Catalytic reaction of aromatic hydrocarbons using hierarchical pore structure zeolites", 247th ACS National Meeting & Exposition, April 2014, Dallas, TX, USA.
- Shoucheng Du, Nicholas Fleming, Julia Valla and George M. Bollas. Fast Catalytic Pyrolysis of Biomass and Relevant Model Compounds Studied in a Spouted Bed Reactor: Effect of Catalyst Type and Loading. AICHE Annual Meeting, November 2013, San Francisco, CA, USA.
- Ameya Akkalkotkar, Shoucheng Du, George M. Bollas and Julia Valla. Hierarchical Pore Structure Zeolites for the Catalytic Upgrading of Tars. AICHE Annual Meeting, November 2013, San Francisco, CA, USA.

- Shoucheng Du, Julia Valla, George M. Bollas. The fate of catalyst during catalytic pyrolysis of biomass and relevant model compounds. 245rd ACS National Meeting & Exposition, April 2013, New Orleans, LA, USA. (PRESENTATIONS ON DEMAND)
- Shoucheng Du, Fabio Poretti, Iman Noshadi, Richard Parnas and George M. Bollas. 100% conversion of waste brown grease to biodiesel and syngas as valuable products for heat and power cogeneration. AIChE Annual Meeting, October 2012, Pittsburgh, PA, USA.
- Shoucheng Du, George M. Bollas. Char and Coke Characterization From Fast and Slow, Catalytic and Non-Catalytic Pyrolysis of Biomass and Relevant Model Compounds. AIChE Annual Meeting, October 2012, Pittsburgh, PA, USA.
- Julia Valla, Shoucheng Du, George M. Bollas. Coal and biomass and power generation via fischer-tropsch synthesis and fuel cells. AIChE Annual Meeting, October 2012, Pittsburgh, PA, USA.
- J. Valla, S. Du, G. M. Bollas, "Gasification of biomass for clean energy production" American Chemical Society Meeting, Division of Energy and Fuels, August 19-23, 2012, Philadelphia, PA, USA.
- Ioulia Valla, Shoucheng Du, G.M. Bollas. Clean fuels from biomass: Comparison of biofuels produced via catalytic pyrolysis and gasification/Fischer-Tropsch synthesis. 243rd ACS National Meeting & Exposition, March 2012, San Diego, CA, USA.
- Shoucheng Du, Julia Valla, G.M. Bollas. A Model-Assisted Tool for the Characterization of Char in Biomass Pyrolysis and Biomass Catalytic Pyrolysis. AIChE Annual Meeting, October 2011, Minneapolis, MN, USA. (PRESENTATIONS ON DEMAND)

Conference posters

- M. Dahl, D. Gamliel, S. Du, G. Bollas, J. Valla, "Introduction of mesoporoisty in ZSM-5 and Zeolite Y to reduce coke production from hydrocarbons", 8th International Conference of Environmental Catalysis, 24-27 August 2014, Ashville, NC, USA.
- Shoucheng Du, Ari Fischer and George M. Bollas. Effect of CH4 Co-Feeding On Biomass Catalytic Pyrolysis. AICHE Annual Meeting, November 2013, San Francisco, CA, USA.
- Shoucheng Du and George M. Bollas. Challenges in the Operation of a Fluidized Bed Reactor for Biomass Pyrolysis. AICHE Annual Meeting, November 2013, San Francisco, CA, USA.
- Zhiquan Zhou, Shoucheng Du, Ari Fischer, Lu Han and George M. Bollas. Chemical-Looping With Oxygen Uncoupling of Coal in a Spouted Bed. AICHE Annual Meeting, November 2013, San Francisco, CA, USA.
- Zhiquan Zhou, Lu Han, Shoucheng Du, Ari Fischer and George M. Bollas. An Overview of Chemical-Looping Reduction in Fixed-Bed and Fluidized Bed Reactors Focused On Oxygen Carrier Utilization and Reactor Efficiency. AICHE Annual Meeting, November 2013, San Francisco, CA, USA.
- Shoucheng Du, Julia Valla and George M. Bollas. Design and Initial Testing of a Spouted-Bed Reactor for Biomass Catalytic Pyrolysis. AIChE Annual Meeting, October 2011, Minneapolis, MN, USA.

APPENDIX IV Copyright

Chapter 3: Reprinted with permission from Catalytic pyrolysis of miscanthus × giganteus in a spouted bed reactor, Bioresource Technology, 2014, 169, 188-197. Copyright (2014) Elsevier.

Chapter 5: Reprinted with permission from Characteristics and origin of char and coke fromfast and slow, catalytic and thermal pyrolysis of biomass and relevant model compounds, Green Chemistry, 2013, 15, 3214-3229. Copyright (2013) The Royal Society of Chemistry.

Appendix I: Reprinted with permission from Catalyzed production of biodiesel and bio-chemicals from brown grease using Ionic Liquid functionalized ordered mesoporous polymer, Applied Energy, 2014, 129, 112-122. Copyright (2014) Elsevier.

Appendix II: Reprinted with permission from The effect of temperature, heating rate, and ZSM-5 catalyst on the product selectivity of the fast pyrolysis of Spent Coffee Grounds. RSC Advances. 2015, 5, 29252-29261. Copyright (2015) The Royal Society of Chemistry.

REFERENCES

1 D. M. Alonso, J. Q. Bond and J. A. Dumesic, *Green Chem.*, 2010, **12**, 1493.

2 H. Cui and J. R. Grace, *Bioresour. Technol.*, 2008, **99**, 4008–20.

3 A. V. Bridgwater and G. V. C. Peacocke, *Renew. Sustain. Energy Rev.*, 2000, **4**, 1–73.

4 A. C. Kokossis and A. Yang, *Comput. Chem. Eng.*, 2010, **34**, 1397–1405.

5 J. Adam, E. Antonakou, A. Lappas, M. Stöcker, M. H. Nilsen, A. Bouzga, J. E. Hustad and G. Øye, *Microporous Mesoporous Mater.*, 2006, **96**, 93–101.

6 G. W. Huber, S. Iborra and A. Corma, *Chem. Rev.*, 2006, **106**, 4044–98.

7 G. W. Huber, *Natl. Sci. Found. - Div. Chem. Bioeng. Environ. Transp. Syst.*, 2008.

8 A. V. Bridgwater, *Catal. Today*, 1996, **29**, 285–295.

9 J. C. Serrano-Ruiz, R. M. West and J. a Dumesic, *Annu. Rev. Chem. Biomol. Eng.*, 2010, **1**, 79–100.

10 H. J. Park, H. S. Heo, J.-K. Jeon, J. Kim, R. Ryoo, K.-E. Jeong and Y.-K. Park, *Appl. Catal. B Environ.*, 2010, **95**, 365–373.

11 *Energy Res. Cent. Netherlands (ECN), ECN-Biomass Phyllis, Http//www.ecn.nl/phyllis*, 2010.

12 S. N. Naik, V. V. Goud, P. K. Rout and A. K. Dalai, *Renew. Sustain. Energy Rev.*, 2010, **14**, 578–597.

13 D. Mohan, C. U. Pittman, and P. H. Steele, *Energy & Fuels*, 2006, **20**, 848–889.

14 F. A. Agblevor, O. Mante, N. Abdoulmoumine and R. McClung, *Energy & Fuels*, 2010, **24**, 4087–4089.

15 A. V. Bridgwater, D. Meier and D. Radlein, *Org. Geochem.*, 1999, **30**, 1479–1493.

16 E. Taarning, C. M. Osmundsen, X. Yang, B. Voss, S. I. Andersen and C. H. Christensen, *Energy Environ. Sci.*, 2011, **4**, 793.

17 A. J. Foster, J. Jae, Y.-T. Cheng, G. W. Huber and R. F. Lobo, *Appl. Catal. A Gen.*, 2012, **423-424**, 154–161.

18 Y. Cheng and G. W. Huber, *ACS Catal.*, 2011, **1**, 611–628.

19 J. Jae, G. A. Tompsett, Y.-C. Lin, T. R. Carlson, J. Shen, T. Zhang, B. Yang, C. E. Wyman, W. C. Curtis and G. W. Huber, *Energy Environ. Sci.*, 2010, **3**, 358–365.

20 T. R. Carlson, Y. Cheng, J. Jae and G. W. Huber, *Energy Environ. Sci.*, 2011, **4**, 145.

21 P. R. Patwardhan, D. L. Dalluge, B. H. Shanks and R. C. Brown, *Bioresour. Technol.*, 2011, **102**, 5265–5269.

22 K. Wang and R. C. Brown, *Green Chem.*, 2013, **15**, 675.

23 S. Thangalazhy-Gopakumar, S. Adhikari, R. B. Gupta and S. D. Fernando, *Energy & Fuels*, 2011, **25**, 1191–1199.

24 Z. Du, B. Hu, X. Ma, Y. Cheng, Y. Liu, X. Lin, Y. Wan, H. Lei, P. Chen and R. Ruan, *Bioresour. Technol.*, 2013, **130**, 777–82.

25 V. Srinivasan, S. Adhikari, S. A. Chattanathan and S. Park, 2012.

26 M. Guerrero, M. P. Ruiz, M. U. Alzueta, A. R. Bilbao and A. Millera, *J. Anal. Appl. Pyrolysis*, 2005, **74**, 307–314.

27 J. Cho, J. M. Davis and G. W. Huber, *ChemSusChem*, 2010, **3**, 1162–5.

28 A. Aho, N. Kumar, K. Eränen, T. Salmi, M. Hupa, D. Y. Murzin and K. Eranen, *Fuel*, 2008, **87**, 2493–2501.

29 G. Elordi, M. Olazar, G. Lopez, P. Castaño and J. Bilbao, *Appl. Catal. B Environ.*, 2011, **102**, 224–231.

30 G. W. Huber and A. Corma, *Angew. Chemie*, 2007, **46**, 7184–201.

31 K. S. Triantafyllidis, E. F. Iliopoulou, E. V. Antonakou, A. A. Lappas, H. Wang and T. J. Pinnavaia, *Microporous Mesoporous Mater.*, 2007, **99**, 132–139.

32 D. J. Nowakowski, A. V. Bridgwater, D. C. Elliott, D. Meier and P. De Wild, *J. Anal. Appl. Pyrolysis*, 2010, **88**, 53–72.

33 M. Al-Haddad, E. Rendek, J.-P. Corriou and G. Mauviel, *Energy & Fuels*, 2010, **24**, 4689–4692.

34 M. J. Antal and M. Grønli, *Ind. Eng. Chem. Res.*, 2003, **42**, 1619–1640.

35 C. Di Blasi, *Prog. Energy Combust. Sci.*, 2008, **34**, 47–90.

36 H. Zhang, T. R. Carlson, R. Xiao and G. W. Huber, *Green Chem.*, 2012, **14**, 98.

37 D. Fabbri, A. G. Rombolà, C. Torri and K. A. Spokas, *J. Anal. Appl. Pyrolysis*, 2013, **103**, 60–67.

38 C. E. Brewer, K. Schmidt-Rohr, J. A. Satrio and R. C. Brown, *Environ. Prog. Sustain. Energy*, 2009, **28**, 386–396.

39 B. Valle, P. Castaño, M. Olazar, J. Bilbao and A. G. Gayubo, *J. Catal.*, 2012, **285**, 304–314.

40 M. Guisnet and P. Magnoux, *Appl. Catal. A Gen.*, 2001, **212**, 83–96.

41 L. Hora, V. Kelbichová, O. Kikhtyanin, O. Bortnovskiy and D. Kubička, *Catal. Today*, 2014, **223**, 138–147.

42 S. Mani, J. R. Kastner and A. Juneja, *Fuel Process. Technol.*, 2013, **114**, 118–125.

43 F. Lannuzel, R. Bounaceur, R. Michels, G. Scacchi and P.-M. Marquaire, *J. Anal. Appl. Pyrolysis*, 2010, **87**, 236–247.

44 T. Odedairo, R. J. Balasamy and S. Al-Khattaf, *J. Mol. Catal. A Chem.*, 2011, **345**, 21–36.

45 H. S. S. Cerqueira, G. Caeiro, L. Costa and F. Ramôa Ribeiro, *J. Mol. Catal. A Chem.*, 2008, **292**, 1–13.

46 R. Quintana-Solórzano, J. W. Thybaut, G. B. Marin, R. Lødeng and A. Holmen, *Catal. Today*, 2005, **107-108**, 619–629.

47 J. Huang, Y. Jiang, V. R. R. Marthala, A. Bressel, J. Frey and M. Hunger, *J. Catal.*, 2009, **263**, 277–283.

48 L. Zhang, J. Cai, T. Zhang and F. Qi, *Combust. Flame*, 2010, **157**, 1686–1697.

49 A. Matsugi and A. Miyoshi, *Proc. Combust. Inst.*, 2013, **34**, 269–277.

50 M. B. Colket and D. J. Seery, *Twenty-fifth Symp. Combust.*, 1994, 883–891.

51 Y.-T. Cheng and G. W. Huber, *Green Chem.*, 2012, **14**, 3114.

52 K. K. Ramasamy, M. A. Gerber, M. Flake, H. Zhang and Y. Wang, *Green Chem.*, 2014, **16**, 748.

53 T. Q. Hoang, X. Zhu, L. L. Lobban, D. E. Resasco and R. G. Mallinson, *Catal. Commun.*, 2010, **11**, 977–981.

54 A. Aho, N. Kumar, A. V. Lashkul, K. Eränen, M. Ziolek, P. Decyk, T. Salmi, B. Holmbom, M. Hupa and D. Y. Murzin, *Fuel*, 2010, **89**, 1992–2000.

55 M. Olazar, R. Aguado, J. Bilbao and A. Barona, *AIChE J.*, 2000, **46**, 1025–1033.

56 J. Jae, G. A. Tompsett, A. J. Foster, K. D. Hammond, S. M. Auerbach, R. F. Lobo and G. W. Huber, *J. Catal.*, 2011, **279**, 257–268.

57 E. M. Sulman, V. V. Alferov, Y. Y. Kosivtsov, A. I. Sidorov, O. S. Misnikov, A. E. Afanasiev, N. Kumar, D. Kubicka, J. Agullo, T. Salmi and D. Y. Murzin, *Chem. Eng. J.*, 2007, **134**, 162–167.

58 T. R. Carlson, G. A. Tompsett, W. C. Conner and G. W. Huber, *Top. Catal.*, 2009, **52**, 241–252.

59 T. R. Carlson, J. Jae, Y.-C. Lin, G. A. Tompsett and G. W. Huber, *J. Catal.*, 2010, **270**, 110–124.

60 L. CDS Analytical, .

61 S. Du, Y. Sun, D. P. Gamliel, J. A. Valla and G. M. Bollas, *Bioresour. Technol.*, 2014, **169**, 188–197.

62 S. Thangalazhy-Gopakumar, S. Adhikari, S. A. Chattanathan and R. B. Gupta, *Bioresour. Technol.*, 2012, **118**, 150–7.

63 H. J. Park, K.-H. Park, J.-K. Jeon, J. Kim, R. Ryoo, K.-E. Jeong, S. H. Park and Y.-K. Park, *Fuel*, 2012, **97**, 379–384.

64 B. Cassel, K. Menard and C. Earnest, *Proximate Analysis of Coal and Coke using the STA 8000 Simultaneous Thermal Analyzer. PerkinElmer, Inc. 1-4*, 2012.

65 S. Du, J. A. Valla and G. M. Bollas, *Green Chem.*, 2013, **15**, 3214.

66 E. F. Iliopoulou, S. D. Stefanidis, K. G. Kalogiannis, A. Delimitis, A. A. Lappas and K. S. Triantafyllidis, *Appl. Catal. B Environ.*, 2012, **127**, 281–290.

67 J. Dai, H. Cui and J. R. Grace, *Prog. Energy Combust. Sci.*, 2012, **38**, 716–736.

68 M. Olazar, M. J. San Jose, F. J. Penas, A. T. Aguayo and J. Bilbao, *Ind. Eng. Chem. Res.*, 1993, **32**, 2826–2834.

69 M. Olazar, G. López, H. Altzibar, R. Aguado and J. Bilbao, *Can. J. Chem. Eng.*, 2009, **87**, 541–546.

70 M. J. San José, S. Alvarez, A. Morales, L. B. López and A. Ortiz de Salazar, *Catal. Today*, 2009, **147**, S162–S169.

71 A. E. Gorshtein and I. P. Mukhlenov, *Zh. Prikl. Khim.*, 1964, **37**, 1887–1893.

72 I. P. Mukhlenov and A. E. Gorshtein, *Khim. Prom.*, 1965, **41**, 443–446.

73 M. Olazar, M. J. San José, A. T. Aguayo, J. M. Arandes and J. Bilbao, *Chem. Eng. J.*, 1993, **51**, 53–60.

74 H. T. Bi, A. Macchi, J. Chaouki and R. Lecros, *Can. J. Chem. Eng.*, 1997, **75**, 0–5.

75 I. D. Lima Rojas, *Sep. Sci. Technol.*, 2010, **45**, 1928–1934.

76 M. Olazar, M. J. San Jose, A. T. Aguayo, J. M. Arandes and J. Bilbao, *Ind. Eng. Chem. Res.*, 1993, **32**, 1245–1250.

77 N. Epstein, *Can. J. Chem. Eng.*, 2013, **91**, 1744–1745.

78 H. T. T. H. Bi, J. R. J. J. R. Grace, H. T. Bi and J. R. Grace and grace, *Int. J. Multiph. Flow*, 1995, **21**, 1229–1236.

79 J. R. Grace, *Can. J. Chem. Eng.*, 1986, **64**, 353–363.

80 A. Haider and O. Levenspiel, *Powder Technol.*, 1989, **58**, 63–70.

81 P. T. Williams and N. Nugranad, *Energy*, 2000, **25**, 493–513.

82 E. Pütün, B. B. Uzun and A. E. Pütün, *Bioresour. Technol.*, 2006, **97**, 701–10.

83 K. Wang, K. H. Kim and R. C. Brown, *Green Chem.*, 2014, **16**, 727–735.

84 A. Aho, N. Kumar, K. Eränen, T. Salmi, M. Hupa and D. Y. Murzin, *Process Saf. Environ. Prot.*, 2007, **85**, 473–480.

85 A. Atutxa, R. Aguado, A. G. Gayubo, M. Olazar and J. Bilbao, *Energy & Fuels*, 2005, **19**, 765–774.

86 S. R. Naqvi, Y. Uemura, S. B. Yusupa and S. B. Yusup, *J. Anal. Appl. Pyrolysis*, 2014, **106**, 57–62.

87 L. Wang, H. Lei, S. Ren, Q. Bu, J. Liang, Y. Wei, Y. Liu, G.-S. J. Lee, S. Chen, J. Tang, Q. Zhang and R. Ruan, *J. Anal. Appl. Pyrolysis*, 2012, **98**, 194–200.

88 A. A. Lappas, M. C. Samolada, D. K. Iatridis, S. S. Voutetakis and I. A. Vasalos, *Fuel*, 2002, **81**, 2087–2095.

89 J. Jae, R. Coolman, T. J. Mountziaris and G. W. Huber, *Chem. Eng. Sci.*, 2014, **108**, 33–46.

90 S. R. Naqvi, Y. Uemura and S. B. Yusup, *J. Anal. Appl. Pyrolysis*, 2014, **106**, 57–62.

91 V. Srinivasan, S. Adhikari, S. A. Chattanathan and S. Park, *Energy & Fuels*, 2012, **26**, 7347–7353.

92 Y.-T. Cheng, J. Jae, J. Shi, W. Fan and G. W. Huber, *Angew. Chemie*, 2012, **124**, 1416–1419.

93 A. Zheng, Z. Zhao, S. Chang, Z. Huang, H. Wu, X. Wang, F. He and H. Li, *J. Mol. Catal. A Chem.*, 2014, **383-384**, 23–30.

94 H. Zhang, R. Xiao, H. Huang and G. Xiao, *Bioresour. Technol.*, 2009, **100**, 1428–34.

95 O. D. Mante, F. A. Agblevor, S. T. Oyama and R. McClung, *Fuel*, 2014, **117**, 649–659.

96 S. D. Stefanidis, K. G. Kalogiannis, E. F. Iliopoulou, A. A. Lappas and P. A. Pilavachi, *Bioresour. Technol.*, 2011, **102**, 8261–7.

97 Y. Yu, X. Li, L. Su, Y. Zhang, Y. Wang and H. Zhang, *Appl. Catal. A Gen.*, 2012, **447-448**, 115–123.

98 S. Wan and Y. Wang, *Front. Chem. Sci. Eng.*, 2014, **8**, 280–294.

99 T. S. S. Nguyen, M. Zabeti, L. Lefferts, G. Brem and K. Seshan, *Biomass and Bioenergy*, 2013, **48**, 100–110.

100 K. Wang, P. A. Johnston and R. C. Brown, *Bioresour. Technol.*, 2014, **173**, 124–131.

101 H. Zhang, R. Xiao, D. Wang, Z. Zhong, M. Song, Q. Pan and G. He, *Energy & Fuels*, 2009, **23**, 6199–6206.

102 G. M. Bollas, S. Papadokonstadakis, J. Michalopoulos, G. Arampatzis, A. A. Lappas, I. A. Vasalos and A. Lygeros, *Chem. Eng. Process.*, 2003, **42**, 697–713.

103 S. Du, Y. Sun, D. P. Gamliel, J. A. Valla and G. M. Bollas, *Bioresour. Technol.*, 2014, **169**, 188–97.

104 D. L. Compton, M. a. Jackson, D. J. Mihalcik, C. a. Mullen and A. a. Boateng, *J. Anal. Appl. Pyrolysis*, 2011, **90**, 174–181.

105 M. S. Mettler, D. G. Vlachos and P. J. Dauenhauer, *Energy Environ. Sci.*, 2012, **5**, 7797.

106 K. Wang, K. H. Kim and R. C. Brown, *Green Chem.*, 2014, **16**, 727.

107 B. Valle, A. G. Gayubo, A. Atutxa and A. Alonso, 2007, **5**.

108 M. S. Mettler, A. D. Paulsen, D. G. Vlacos and P. J. Dauenhauer, *Catal. Sci. Technol.*, 2014, **4**, 3822.

109 M. Asadullah, S. Zhang, Z. Min, P. Yimsiri and C.-Z. Li, *Bioresour. Technol.*, 2010, **101**, 7935–43.

110 M. S. Hasan Khan Tushar, N. Mahinpey, A. Khan, H. Ibrahim, P. Kumar and R. Idem, *Biomass and Bioenergy*, 2012, **37**, 97–105.

111 C. Di Blasi, *Prog. Energy Combust. Sci.*, 2009, **35**, 121–140.

112 D. Ferdous, A. K. Dalai, S. K. Bej and R. W. Thring, *Energy & Fuels*, 2002, **16**, 1405–1412.

113 R. K. Sharma, J. B. Wooten, V. L. Baliga, X. Lin, W. Geoffrey Chan and M. R. Hajaligol, *Fuel*, 2004, **83**, 1469–1482.

114 Y. Y.-C. Lin, J. Cho, G. A. Tompsett, P. R. Westmoreland and G. W. Huber, *J. Phys. Chem. C*, 2009, **113**, 20097–20107.

115 P. R. Patwardhan, J. A. Satrio, R. C. Brown and B. H. Shanks, *Bioresour. Technol.*, 2010, **101**, 4646–55.

116 M. S. Mettler, A. D. Paulsen, D. G. Vlachos and P. J. Dauenhauer, *Green Chem.*, 2012, **14**, 1284.

117 K. Miura and P. L. Silveston, *Energy & Fuels*, 1989, **3**, 243–249.

118 J. Shen, X.-S. Wang, M. Garcia-Perez, D. Mourant, M. J. Rhodes and C.-Z. Li, *Fuel*, 2009, **88**, 1810–1817.

119 P. R. Patwardhan, J. A. Satrio, R. C. Brown and B. H. Shanks, *J. Anal. Appl. Pyrolysis*, 2009, **86**, 323–330.

120 M. S. Mettler, S. H. Mushrif, A. D. Paulsen, A. D. Javadekar, D. G. Vlachos and P. J. Dauenhauer, *Energy Environ. Sci.*, 2012, **5**, 5414.

121 J. Fermoso, M. V. Gil, C. Pevida, J. J. Pis and F. Rubiera, *Chem. Eng. J.*, 2010, **161**, 276–284.

122 K. Slopiecka, P. Bartocci and F. Fantozzi, *Appl. Energy*, 2012, **97**, 491–497.

123 A. K. Burnham and R. L. Braun, *Energy & Fuels*, 1999, **13**, 1–22.

124 Y. Zhang, S. Kajitani, M. Ashizawa and Y. Oki, *Fuel*, 2010, **89**, 302–309.

125 R. Vinu and L. J. Broadbelt, *Energy Environ. Sci.*, 2012, **5**, 9808.

126 B. Guichard, M. Roy-Auberger, E. Devers, B. Rebours, A. A. Quoineaud and M. Digne, *Appl. Catal. A Gen.*, 2009, **367**, 1–8.

127 C. Sheng, *Fuel*, 2007, **86**, 2316–2324.

128 K. Control, 1980, **26**, 379–386.

129 V. B. Di Marco and G. G. Bombi, *J. Chromatogr. A*, 2001, **931**, 1–30.

130 D. Vamvuka, E. Kakaras, E. Kastanaki and P. Grammelis, *Fuel*, 2003, **82**, 1949–1960.

131 S. Xin, H. Yang, Y. Chen, X. Wang and H. Chen, *Fuel*, 2013, **113**, 266–273.

132 C. H. Bartholomew, *Appl. Catal. A Gen.*, 2001, **212**, 17–60.

133 M. Guisnet, L. Costa and F. Ramôa, *J. Mol. Catal.*, 2009, **305**, 69–83.

134 *ChemAxon, Marvin Sketch, Https://www.chemaxon.com/products/marvin/.*, 2010.

135 E. L. First, C. E. Gounaris and C. A. Floudas, *Langmuir*, 2013, **29**, 5599–608.

136 *http://helios.princeton.edu/zeomics/.*

137 C.-H. Zhou, X. Xia, C.-X. Lin, D.-S. Tong and J. Beltramini, *Chem. Soc. Rev.*, 2011, **40**, 5588–617.

138 E. L. First, C. E. Gounaris, J. Wei and C. A. Floudas, *Phys. Chem. Chem. Phys.*, 2011, **13**, 17339–58.

139 S. Svelle, U. Olsbye, K.-P. Lillerud, S. Kolboe and M. Bjørgen, *J. Am. Chem. Soc.*, 2006, **128**, 5618–9.

140 J. L. Figueiredo, M. L. G. O. M. Pinto and J. J. M. Orfao, *Appied Catal. A Gen.*, 1993, **104**, 1–9.

141 Y.-M. Chung, D. Mores and B. M. Weckhuysen, *Appl. Catal. A Gen.*, 2011, **404**, 12–20.

142 P. Prokešová, N. Žilková, S. Mintova, T. Bein and J. Čejka, *Appl. Catal. A Gen.*, 2005, **281**, 85–91.

143 J. Rigoreau, S. Laforge, N. Gnep and M. Guisnet, *J. Catal.*, 2005, **236**, 45–54.

144 T. Prasomsri, A. T. To, S. Crossley, W. E. Alvarez and D. E. Resasco, *Appl. Catal. B Environ.*, 2011, **106**, 204–211.

145 A. Ausavasukhi, T. Sooknoi and D. E. Resasco, *J. Catal.*, 2009, **268**, 68–78.

146 C. D. Hurd and C. W. Bennett, *J. Am. Chem. Soc.*, 1929, **51**, 1197–1201.

147 A. K. Vasiliou, J. H. Kim, T. K. Ormond, K. M. Piech, K. N. Urness, A. M. Scheer, D. J. Robichaud, C. Mukarakate, M. R. Nimlos, J. W. Daily, Q. Guan, H.-H. Carstensen and G. B. Ellison, *J. Chem. Phys.*, 2013, **139**, 104310.

148 S. Kamiguchi, S. Nishida and I. Takahashi, *J. Mol. Catal. A Chem.*, 2006, **255**, 117–122.

149 I. van Zandvoort, Y. Wang, C. B. Rasrendra, E. R. H. van Eck, P. C. A. Bruijnincx, H. J. Heeres and B. M. Weckhuysen, *ChemSusChem*, 2013, **6**, 1745–58.

150 S. K. R. Patil and C. R. F. Lund, *Energy & Fuels*, 2011, **25**, 4745–4755.

151 N. Li, G. A. Tompsett, T. Zhang, J. Shi, C. E. Wyman and G. W. Huber, *Green Chem.*, 2011, **13**, 91.

152 S. Vaitheeswaran, S. K. Green, P. Dauenhauer and S. M. Auerbach, *ACS Catal.*, 2013, **3**, 2012–2019.

153 C. J. Gilbert, J. S. Espindola, W. C. Conner, J. O. Trierweiler and G. W. Huber, *ChemCatChem*, 2014.

154 P. K. Chu and L. Li, *Mater. Chem. Phys.*, 2006, **96**, 253–277.

155 P. Matousek, M. Towrie and A. W. Parker, *J. Raman Spectrosc.*, 2002, **33**, 238–242.

156 J. Schwan, S. Ulrich, V. Batori, H. Ehrhardt and S. R. P. Silva, *J. Appl. Phys.*, 1996, **80**, 440.

157 A. C. Ferrari and J. Robertson, *Phys. Rev. B*, 2000, **61**, 14095–14107.

158 A. Ochoa, B. Aramburu, M. Ibáñez, B. Valle, J. Bilbao, A. G. Gayubo and P. Castaño, *ChemSusChem*, 2014, **7**, 2597–608.

159 D. Mores, J. Kornatowski, U. Olsbye and B. M. Weckhuysen, *Chem. - A Eur. J.*, 2011, **17**, 2874–2884.

160 M. Guisnet and P. Magnoux, *Appl. Catal. A, Gen.*, 1989, **54**, 1–27.

161 X. Dupain, E. D. Gamas, R. Madon, C. P. Kelkar, M. Makkee and J. A. Moulijn, *Fuel*, 2003, **82**, 1559–1569.

162 C. Fernandez, I. Stan, J.-P. Gilson, K. Thomas, A. Vicente, A. Bonilla and J. Pérez-Ramírez, *Chemistry*, 2010, **16**, 6224–33.

163 B. P. C. Hereijgers, F. Bleken, M. H. Nilsen, S. Svelle, K.-P. Lillerud, M. Bjørgen, B. M. Weckhuysen and U. Olsbye, *J. Catal.*, 2009, **264**, 77–87.

164 B. Smit and T. L. M. Maesen, *Nature*, 2008, **451**, 671–678.

165 L. Palumbo, F. Bonino, P. Beato, M. Bjørgen, A. Zecchina and S. Bordiga, *J. Phys. Chem. C*, 2008, **112**, 9710–9716.

166 S. Marquis, A. Moissette, M. Hureau, H. Vezin and C. Brémard, *J. Phys. Chem. C*, 2007, **111**, 17346–17356.

167 F. Finnouche, Y. Boucheffa, R. Boumaza, A. Labed and P. Magnoux, *Ind. Eng. Chem. Res.*, 2004, **43**, 6708–6713.

168 O. Kikhtyanin, V. Kelbichová, D. Vitvarová, M. Kubů and D. Kubička, *Catal. Today*, 2014, **227**, 154–162.

169 O. Kikhtyanin, P. Chlubná, T. Jindrová and D. Kubička, *Dalton Trans.*, 2014, **43**, 10628–41.

170 W.-L. Fanchiang and Y.-C. Lin, *Appl. Catal. A Gen.*, 2012, **419-420**, 102–110.

171 C. Mukarakate, M. J. Watson, J. ten Dam, X. Baucherel, S. Budhi, M. M. Yung, H. Ben, K. Iisa, R. M. Baldwin and M. R. Nimlos, *Green Chem.*, 2014.

172 J. Li, X. Li, G. Zhou, W. Wang, C. Wang, S. Komarneni and Y. Wang, *Appl. Catal. A Gen.*, 2014, **470**, 115–122.

173 M. Guisnet and P. Magnoux, *Appl. Catal.*, 1989, **54**, 1–27.

174 J. Kim, M. Choi and R. Ryoo, *J. Catal.*, 2010, **269**, 219–228.

175 I. Noshadi, B. Kanjilal, S. S. Du, G. M. Bollas, S. L. Suib, A. Provatas, F. Liu and R. S. Parnas, *Appl. Energy*, 2014, **129**, 112–122.

176 K. S. Tyson, in *NREL*, 2002.

177 H. Zhang, Y.-T. Cheng, T. P. Vispute, R. Xiao and G. W. Huber, *Energy Environ. Sci.*, 2011, **4**, 2297.

178 G. Cheng, P. He, B. Xiao, Z. Hu, S. Liu, L. Zhang and L. Cai, *Energy*, 2012, **43**, 329–333.

179 C. A. Mullen, A. A. Boateng, E. M. Lane and V. Pennsyl, *Energy & Fuels*, 2008, **22**, 2104–2109.

180 C. Branca, P. Giudicianni and C. Di Blasi, *Ind. Eng. Chem. Res.*, 2003, **42**, 3190–3202.

181 A. Fischer, S. Du, J. Valla and G. M. Bollas, *RSC Adv.*, 2015, **5**, 29252–29261.

182 *Historical Data*, London, England.

183 D. J. Wuebbles and K. Hayhoe, *Earth-Science Rev.*, 2002, **57**, 177–210.

184 J. Asomaning, P. Mussone and D. C. Bressler, *Fuel Process. Technol.*, 2014, **120**, 89–95.